Assessing Fuel Efficiency: Hydrodynamic Design Investigation and Operational Considerations in Wind-Assisted Cruise Ships

Graduation Thesis M.Sc. Marine Technology

C.L. Lange

TUDelft

MARIN

Assessing Fuel Efficiency: Hydrodynamic Design Investigation and Operational Considerations in Wind-Assisted Cruise Ships

Graduation Thesis M.Sc. Marine Technology

by

C.L. Lange

to obtain the degree of Master of Science

at the Delft University of Technology.

to be defended publicly on Monday June 10th, 2024 at 02:00 PM.

MT.23/24.028.M

Student number:	5620503	
Thesis committee:	prof.dr.ir. T.J.C. van Terwisga	TU Delft
	dr. A.A. Kana	TU Delft
	dr. A. Laskari	TU Delft
	dr. G. Jacobi	TU Delft
	ir. A. Kisjes	MARIN
	ir. G. Marelli	MARIN

Faculty:	Faculty of Mechanical, Maritime and Materials Engineering
Performed at:	Maritime Research Institute Netherlands (MARIN)
Cover:	Orient Express Silenseas © Martin Darzacq (Modified)

TUDelft   **MARIN**

Summary

In the face of escalating global emissions and rising awareness of the dangers of climate change, there is a need for sustainability initiatives across all industry sectors. Within the shipping industry, this is leading to a resurgence of interest in wind-assisted propulsion systems. This research investigates the hydrodynamic design of a wind-assisted cruise ship, aiming to redefine the image of the historically very polluting cruise industry by designing a vessel aimed at achieving 50% propulsive fuel savings through wind-assisted propulsion.

The literature review provides the broad theoretical and computational background necessary for the design evaluation. The description of the historical evolution of wind propulsion, as well as state-of-the-art wind-assisted vessels and emerging concepts, provides the inspiration for the design investigation.

A detailed hydrodynamic analysis was conducted, focusing on variations in hull design (B/T ratio, deadrise angle) and appendage design (skegs, passive and active anti-drift fins). The efficacy of the modifications was evaluated on an operational level using power prediction programs, allowing for performance assessments in varying conditions.

A semi-empirical approach for the prediction of hydrodynamic forces and moments under drift using the maneuvering tool SURSIM is hypothesized as a computationally light alternative to numerical methods. However, SURSIM was found not to have the required fidelity to accurately predict the lift coefficient of the hull at small drift angles. Therefore, a computational fluid dynamics (CFD) approach was adopted for the determination of the hydrodynamic loads.

The optimal unappended cruise ship design resulted in fuel savings of 34.5%. Optimal hydrodynamic efficiency favors a hull optimized for minimal resistance, and a retractable, active angle-of-attack fin for improved side force and yaw moment balance. The introduction of the fin led to an increase in fuel savings to 37.3%. Notable improvements in ship maneuverability can also be expected based on significantly reduced rudder actuation in sailing conditions.

Operational variations have a large impact on fuel savings. Using the wind statistics of the N. Atlantic Holland America Line increased fuel savings to 48%, compared to the MEPC.1/Circ.896 standard. Considerable further gains can be achieved through the efficient handling of surplus wind power. Allowing a variable operational speed between 10.6kn and 20kn instead of a fixed speed of 12kn increased the fuel savings on the N. Atlantic route to 56.7%.

Wind-assisted propulsion can be a viable strategy for significant fuel savings beyond 50%, and efficient appendage design can meaningfully improve the ship's performance. Accurate prediction of fuel savings requires clear knowledge of the operational conditions and control strategies. Further investigation of the detailed appendage design, and comparison of variable speed operation to the employment of a regenerative propeller mode is recommended.

This thesis contributes to the evolving discourse on sustainable maritime transport, specifically within the cruise ship sector, by providing a comprehensive analysis of wind-assisted propulsion's potential benefits.

Contents

List of Figures

List of Tables

Nomenclature

α	Angle of attack	$[deg]$
β	Weibull shape parameter	$[-]$
β	Leeway angle	$[deg]$
δ	Rudder angle	$[deg]$
Δ	Displacement	$[t]$
η	Weibull scale parameter	$[m/s]$
η	Efficiency	$[-]$
Γ	Circulation	$[m^2/s]$
μ	Dynamic viscosity	$[Pa \cdot s]$
ω	Downwash	$[m/s]$
φ	Heel angle	$[deg]$
ρ	Density	$[kg/m^3]$
τ	Shear stress	$[Pa]$
ζ	Propeller-rudder area ratio	$[-]$
ζ	Distance from forward perpendicular	$[m]$
$\dot{CO_2}$	CO_2 emission rate	$[kg/s]$
A	Area	$[m^2]$
A_w	Wetted area	$[m^2]$
A_{wp}	Waterplane area	$[m^2]$
AR	Aspect ratio	$[-]$
AWA	Apparent wind angle	$[deg]$
AWS	Apparent wind speed	$[m/s]$
B	Beam Length	$[m]$
c	Chord length	$[m]$
C_D	Drag coefficient	$[-]$
C_L	Lift coefficient	$[-]$
C_m	Midship coefficient	$[-]$
C_N	Moment coefficient	$[-]$
C_P	Pressure coefficient	$[-]$
C_p	Prismatic coefficient	$[-]$
CE	Center of effort	$[m]$
CF	Carbon factor	$[-]$
CLR	Center of lateral resistance	$[m]$
$CO_{2,\text{perf}}$	CO_2 performance	$[g/(t \cdot nm)]$
CRZ	Propeller swirl coefficient	$[-]$
d	Distance	$[m]$
DWT	Deadweight	$[t]$

e	Oswald efficiency	$[-]$
F_D	Drag force	$[N]$
F_L	Lift force	$[N]$
F_N	Normal force	$[N]$
Fr	Froude number	$[-]$
g	Gravitational constant	$[m/s^2]$
GM	Metacentric height	$[m]$
GZ	Righting arm	$[m]$
I	Turbulence intensity factor	$[-]$
ICS	Initial cell size	$[m]$
K	Lift slope	$[-]$
L	Length	$[m]$
L_2	Root mean square residuals	$[-]$
L_∞	Maximum residual	$[-]$
LHV	Lower heating value	$[J/kg]$
LPP	Length between perpendiculars	$[m]$
m	Momentum	$[kg \cdot m/s]$
N	Moment in z-direction	$[Nm]$
N_b	Cells per beam length	$[-]$
P	Power	$[W]$
P	Probability	$[-]$
p	Pressure	$[Pa]$
R	Straight-sailing resistance	$[N]$
R_0	Base grid refinement	$[-]$
Re	Reynolds number	$[-]$
RM	Righting moment	$[Nm]$
s	Span	$[m]$
T	Draft	$[m]$
TWA	True wind angle	$[deg]$
TWS	True wind speed	$[m/s]$
u	Flow in x-direction	$[m/s]$
U	Flow velocity	$[m/s]$
v	Flow in y-direction	$[m/s]$
v_s	Ship speed	$[m/s]$
w	Flow in z-direction	$[m/s]$
$y+$	Dimensionless wall distance	$[-]$
$\dot{m}$	Mass flow	$[kg/s]$
$\vec{v}$	Wind field	$[m/s]$
X	Force in x-direction	$[N]$
Y	Force in y-direction	$[N]$

<div align="right">

1

</div>

Introduction

1.1. Context

1.1.1. History of Wind Propulsion

But the sail sport will endure forever, being one of the most vigorous and beautiful sports in existence. Perhaps its mission will be to preserve and further the knowledge of mastering the wind and finally, after long, long years when oil and coal shall have become too costly, to revive to new splendour the grand art of sailing, in modified form perhaps, and based upon further progress in aviation and meteorology, as well as upon other advances in the engineering art. (Walter Laas, 1912) [1]

In the past, limits in propulsive power restrained the potential of seagoing vessels. In the earliest days of shipping, this power had to come from human effort. Manual propulsion required a large crew with inherently low energy density, leading to minimal voyage range and cargo-carrying capacity. This changed around 5000 years through the discovery of wind propulsion through the invention of the soft sail. By harnessing a freely available and abundant resource, crew requirements decreased, ships grew in size, and trading routes developed that would span across all oceans. In this way, the global shipping and sea trading industry can be attributed to the invention of the soft sail [2].

The 19th and 20th centuries' industrialization marks the takeover of mechanical propulsion systems. Because of its high energy density, but most importantly because of its reliability, shipping came to depend on steam and diesel propulsion systems. With oil in cheap and plentiful supply, the research focus for shipping also shifted towards developing efficient propellers, large engines, and hull forms optimized for maximum cargo-carrying capacity. Research on wind-propulsion was then mainly focused on recreational and competitive sailing, leading to hydrodynamic design investigations like the Delft Systematic Yacht Series [3].

In the 1970s, the shipping industry's perception of fuel oil dramatically changed due to disruptions in the Middle Eastern oil supply, highlighting its vulnerability to geopolitical instability. With fuel prices rising, the interest in researching alternative fuel supplies grew. Wind propulsion was a strong candidate, being the only technology proven for sea trade in the past. The research and development of better wind propulsors, which has been dismissed in the past, suddenly became relevant [4]. Most notably, this includes the invention of the Flettner rotor and Cousteau's Turbosail [5]. These inventions were investigated for their higher lift coefficients and much smaller footprints. Other notable designs that gained traction in the 70s and 80s are the kite sail [6], the Dynarig [7], and rigid sails [8]. The sudden spike in interest also sparked an extensive array of experimental research [7], [9]. Economic feasibility studies on hybrid motor-sail configurations were also conducted, concluding that ships carrying low-cost cargo can already be transported more efficiently using wind power on specific routes [10].

This period provides essential foundations for modern literature on the topic. Nonetheless, the wind-supported shipping industry never took off from this push, with only a handful of ships being built, most of

which did not stay competitive for long. With oil prices recovering, there was just not enough economic incentive to reduce fuel consumption. But times have changed. With the realization of the impact that greenhouse gas emissions have on the planet, the current century is the most critical for restructuring our energy sources.
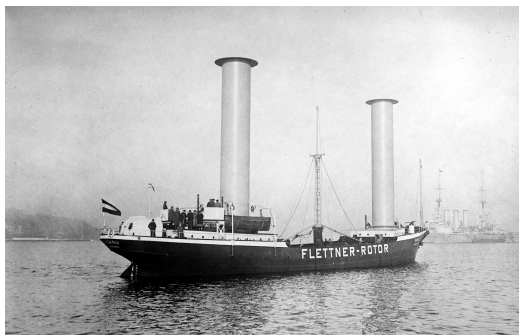
(a) 'Buckau' Flettner rotor ship, 1925 [11].
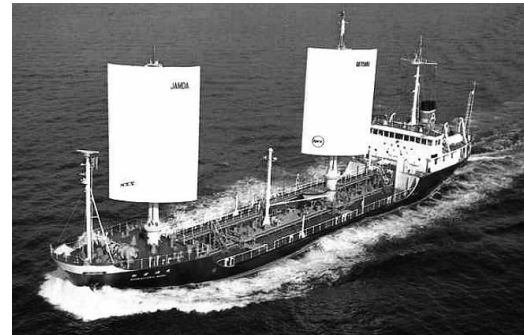
(b) 'Jamda Shin Aitoku Maru' rigid-sail tanker, 1980 [12].

Figure 1.1: Notable historic vessels in the field of wind-assisted propulsion.

1.1.2. A Case for Change

We are already living with climate change. While political decision-making is only slowly starting to grip, people worldwide are already facing its real and increasing effects, with record-breaking temperatures, droughts, floods, and hurricanes increasing year after year. This rise in weather events, along with the spread of diseases, challenges to food production, and rising sea levels, leave no doubt that climate change is a global issue that has to be dealt with urgently [13]. The Intergovernmental Panel on Climate Change (IPCC) studies the scientific evidence for anthropogenic climate change, representing the broad scientific consensus on the matter. To avoid the worst impacts, the global temperature rise must be kept below 1.5°C, as stated in the 2015 Paris Agreement. This is only possible by drastically cutting greenhouse gas emissions, implying net-zero emissions by 2050.

There are fundamental reasons why dealing with climate change is so difficult. First, climate change is a global phenomenon with dispersed causes and effects. There is no single agent, but many individuals contribute to or are affected by the problem. Vulnerability is skewed towards developing countries, while the biggest contributors are developed countries. Cause and effect are also severely offset temporally. The cumulative impact of climate change will only be felt far in the future when the reversal of effects is already out of the question. Action, however, has to be taken now. This temporal fragmentation of agency is a major challenge. It should be clear that it is vital to develop new, emission-reducing technologies now [14].

This calls for a complete transformation of global production, transportation, and consumption. The shipping industry is currently steering in the wrong direction, with an expected 20% increase in well-to-wake emissions predicted by 2050, while already accounting for more than 2% of global emissions [15]. In the tourism transport sector, cruise ships are the most polluting, emitting nearly four times as much carbon dioxide per passenger-mile than airplanes and cars [16]. The fuel consumption of vessels significantly contributes to global warming and has to be reduced further to stay a sustainable means of transport.

Regulators such as the International Maritime Organization (IMO) share this sentiment. The first mandatory measures for the energy efficiency of ships came into effect in 2013 through the Energy Efficiency Design Index (EEDI) [17], setting a minimum energy efficiency in CO_2 emission per tonne-mile for various ship types. The EEDI continues to be an essential benchmark for the fuel efficiency of large ships. However, the emission reductions through the EEDI fall short of the 2050 net-zero goal. This is why the IMO is implementing the Carbon Intensity Index (CII) [18], coming into force in 2023. This index determines the carbon efficiency of the ship, which will have to keep improving to comply with more stringent regulations. For example, to retain the same CII, total carbon emissions for a ship in 2026 will already have to be 6% lower compared to 2023. A poor CII rating will have severe implications for

the vessel's operability. Incentives for ships with superior ratings will be given by administrations, port authorities, and other stakeholders. Contrary to the EEDI, the CII also covers a wider variety of ships, including cruise ships and ferries. The goal of the IMO is to achieve at least a 50% reduction in carbon emissions by 2050.

Historical and recent trends leave little doubt that ship emissions will have to reduce drastically in the next 30 years. As such, it has never been more relevant to investigate how this can be implemented without sacrificing the competitiveness of seaborne transport. Research paths for this are creative and diverse, including the research into energy-saving devices [19], alternative fuels [20], and carbon capture methods [21], to mention a few. Looking at the history of shipping, wind energy has been the main driver of innovation for centuries. Yet, now it is as timely as ever to explore the potential of wind power for the maritime world. Considering the ambitious goals set by the IMO for the shipping sector, vessels will soon have to aim for much more drastic fuel reductions. If this is to be achieved through wind-assisted propulsion, the research into optimizing ships for wind-assisted propulsion is crucial.

1.2. Problem Definition and Objective

The aim of this thesis is to investigate design variations for a novel cruise ship aiming at achieving 50% fuel savings through wind-assisted propulsion. The Orient Express: *Silenseas* project by Chantiers de l'Atlantique [22] provides the reference case. It deals with the design of a 220m long cruise ship, promoting an environmentally conscious luxury cruising experience for up to 120 passengers in 54 spacious suites. Fuel-saving percentages refer to the reduction in average fuel consumption of the propulsion system during operation, compared to an identical operation without wind assist.
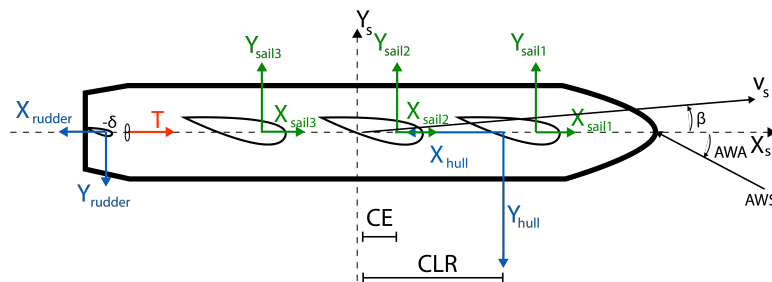
Figure 1.2: Free-body diagram of a wind-assisted ship.

The design of such a vessel is a complex, multidisciplinary endeavor. For this research, the focus lies on hydrodynamic design considerations. All current wind-assist systems generate considerable side forces on the vessel for most apparent wind angles. This is because the aerodynamic lifting surfaces produce lift that is almost perpendicular to the ship's course, leading to a large transverse force on the ship.

This side force is concentrated in the center of effort (CE) and has to be balanced to maintain sailing equilibrium. Conventionally, the hull provides the opposing lift force by sailing at a drift angle β. This force is concentrated in the center of lateral resistance (CLR) of the hull. For typical hull designs, the CLR of the ship lies close to the bow, while the CE is at midship for evenly distributed sails. The offset between the two points creates a moment often balanced by an additional force generated by the rudder [23]. The deflection of the rudder not only limits the ship's maneuverability but also causes additional resistance. This resistance adds to the already increased resistance of the hull sailing at a drift angle. The CE will also be vertically offset, leading to a heeling moment that must be compensated by the righting moment of the hull.

The efficient balance of forces and moments on a sailing ship through the optimized use of various hydro-lifting surfaces forms a fundamental goal in the design and operation of wind-assisted ships.

Finding and evaluating design strategies to achieve a balanced wind-assisted ship is the goal of this research. The following research question was defined based on this:

> What modifications in the hydrodynamic design of a cruise ship are most effective for wind-assisted propulsion to potentially achieve 50% fuel savings, and how can the performance of these modifications be accurately evaluated?

The question can be interpreted in two parts. One is through the actual design study of the cruise ship, and evaluation of different key design parameters. The other is through the method with which the performance of the designs can be quantified, evaluated, and compared. Both aspects are key goals for this research.

To investigate the specific aspects of the hydrodynamic design, which are expected to have the greatest influence on the overall performance, the following sub-question was defined:

1. Which hydrodynamic design variations, including hull shape, appendages, and active control systems, enhance the fuel savings of wind-assisted cruise ships by optimizing side force and moment balance?

Active control refers to appendages that are either retractable or can alter their orientation with respect to the flow. The focus lies on identifying and investigating the most promising hydrodynamic aspects to optimize the fuel savings of wind-assisted ships while considering relevant operational constraints. A holistic approach is adapted to ensure that potential benefits are not just theoretical but also reflected in actual fuel savings during operation.

Given the many parameters involved in the hydrodynamic design, evaluating an optimum could require investigating an extensive design space. This can quickly become a very computationally expensive endeavor. Therefore, the other, secondary sub-question deals with the method of getting to the evaluation of different designs:

2. How accurately can a lower-fidelity, semi-empirical tool predict the hydrodynamic performance of wind-assisted ship designs compared to a computational fluid dynamics approach?

In combination, this allows for both an analysis of the design space and estimated performance for a wind-assisted cruise ship, as well as an investigation on the methodology for the design of future wind-assisted ships in general.

2

Literature Review

2.1. Theoretical Background

2.1.1. Forces on a Foil in 2D

The force equilibrium of a sailing ship relies entirely on the lift and drag generated by surfaces exposed to the flow of air and water. Characterizing each of these contributions using the principle of foils is helpful to understand their effects [24].

Flow diversion around any object causes a drag force due to surface stresses (friction drag) and pressure distributions (form drag). The drag force is defined in the direction of the incoming flow. If the pressure distribution is asymmetrical, another force component orthogonal to the incoming flow exists, the lift force. The goal of foils is to minimize friction and form drag while maximizing lift. Non-dimensionalizing the lift and drag forces gives the key indicators for foil performance:

$$C_L = \frac{F_L}{\frac{1}{2}\rho U^2 A} \tag{2.1}$$

$$C_D = \frac{F_D}{\frac{1}{2}\rho U^2 A} \tag{2.2}$$

The higher the lift-to-drag ratio C_L/C_D, the more efficient the foil. The anatomy of foil geometry can be generalized into a couple of main parameters, illustrated in Figure 2.1a. The chord length is the distance between the leading edge (the stagnation point at which the flow encounters the foil) and the trailing edge (the stagnation point at which the flow from the upper and lower surface meet). Normal to this line, the thickness of the foil is defined. If lift is generally generated in only one direction (e.g. for an airplane), an asymmetrical foil can lead to better performance. In that case, a camber is introduced, which is the offset between the geometrical center of the foil to the chord line.

(a) Airfoil geometry.   (b) Force decomposition.
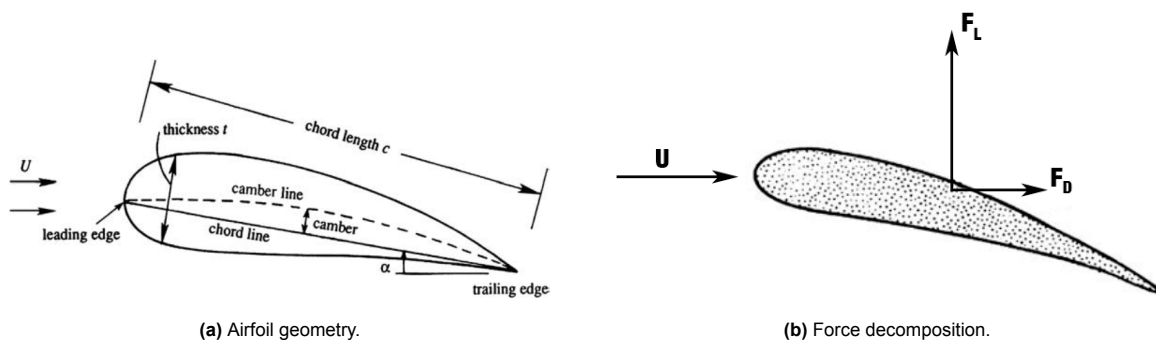
Figure 2.1: Definitions for geometry and forces on a foil [24]. (modified)

Figure 2.2a shows that the biggest contribution to the lift force is the low (suction) pressure of the upper surface of the foil. Integrating the pressure over the surface of the foil gives the normal force on it, which then can be decomposed to obtain the lift and drag forces.

Foils are often used at varying angles-of-attack α. This may be to adapt to the highest lift-to-drag ratio at different flow speeds (e.g. with controllable-pitch propellers) or when used for steering (e.g. with rudders). This makes it relevant to look at the performance of foils over a range of angles of attack. A typical lift and drag curve for a foil is shown in Figure 2.2b.

(a) Pressure distribution.
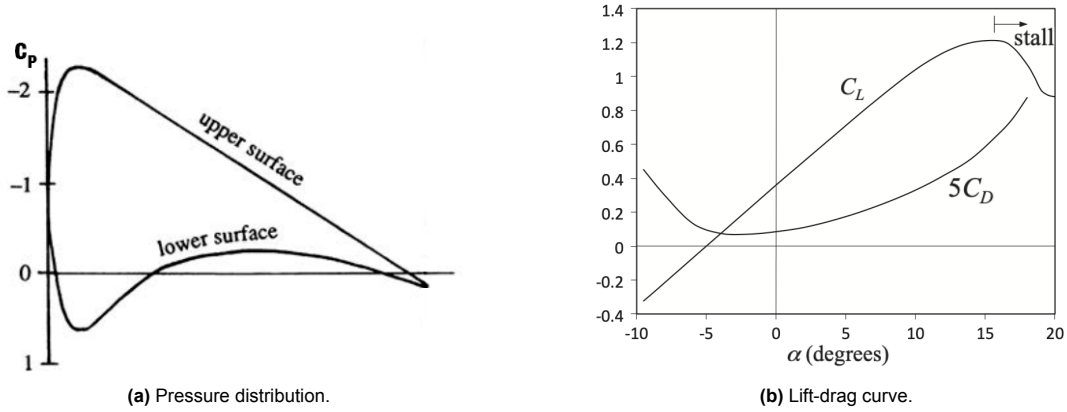
(b) Lift-drag curve.

Figure 2.2: Typical pressure distribution and lift-drag curve for a foil [24]. (modified)

The lift increases for higher angles of attack as the suction pressure decreases due to the stronger flow deflection. The lift follows an approximately linear behavior.

In an ideal case, the vorticity in the boundary layer around the foil defines the lift. Based on potential flow theory, this lift can be determined analytically in a simplified manner using the Kutta-Joukowski Theorem [24]. Since the flow in potential theory is invisicid, lift has to be introduced artificially. This is done using the Kutta condition, which assumes a bound vortex of sufficient strength Γ to move the rear stagnation point to the trailing edge. The strength of this vortex is directly related to the lift force by:

$$F_L = \rho U \Gamma_{\text{kutta}} \tag{2.3}$$

Using the Kutta–Joukowski Theorem it can be shown that for a symmetrical Joukowski foil, the lift is then related to the angle of attack with:

$$C_{L,2D} = 2\pi \sin \alpha \tag{2.4}$$

which is approximately linear for small angles of α. Deviations from this ideal foil are reflected in the lift-curve slope, leading to the general form:

$$C_{L,2D} = K \sin \alpha \tag{2.5}$$

(a)

(b)
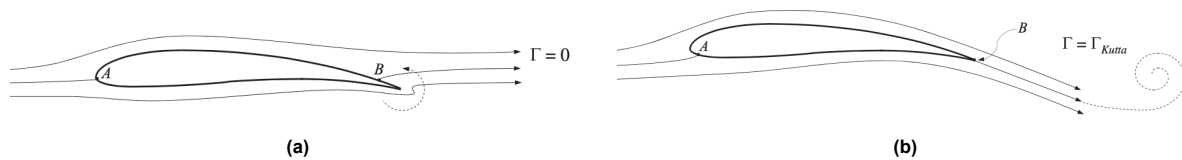
Figure 2.3: Satisfying the Kutta condition by imposing circulation Γ_{kutta}. The dashed vortex in (b) is the original (opposing) starting vortex created the foil was first exposed to the flow, ensuring momentum conservation [24]. (modified)

A steep drop in lift can be noted as the foil stalls at a higher angle of attack. This phenomenon is due to the change in pressure along the suction side of the foil. The pressure decreases rapidly from the leading edge to the minimum pressure point with $\frac{\partial p}{\partial x} < 0$, after which it increases again with $\frac{\partial p}{\partial x} > 0$. The more extreme the low-pressure peak, the steeper this adverse gradient is. If the pressure increases

rapidly, the flow velocity decreases quickly. At some point, this can lead to a flow reversal close to the surface of the foil, where the velocity is already lower due to the viscous boundary layer. This reversal causes the flow to separate from the foil, leaving behind a trailing low-pressure turbulent wake. At the stall angle, this detachment happens so close to the leading edge that much less lift is generated.

<div align="center">(a) Flow reversal in the boundary layer.   (b) Visualization of a stalled foil.</div>
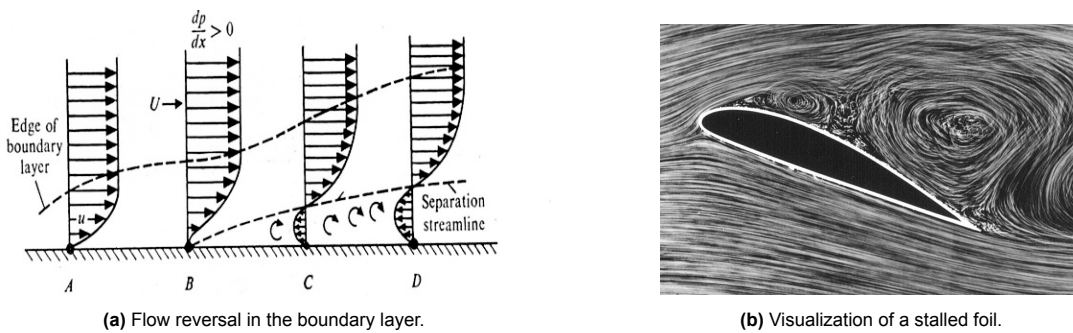
<div align="center">**Figure 2.4:** Effect of separation in boundary layer and associated stall [24]. (modified)</div>

In most cases, foils are operated at angles of attack lower than the stall angle. Running close to the stall angle is dangerous, as a sudden drop in performance can occur. As the drag also increases with increased angles of attack, an optimum angle can be found for which the lift-to-drag ratio is highest. Because these coefficients depend on the Reynolds number, different flow velocities lead to different ideal angles of attack.

2.1.2. Forces on a Foil in 3D

Up until now, the foil was treated in two dimensions, fully defined by its cross-section. Additional considerations apply when looking at the three-dimensional case. The fundamental difference when looking at a 3D case is the tip-vortex effect. As with the 2D working principle, the pressure on the suction side

<div align="center">(a) Schematical tip-vortex generation [24].   (b) Visible trailing vortices [25].</div>
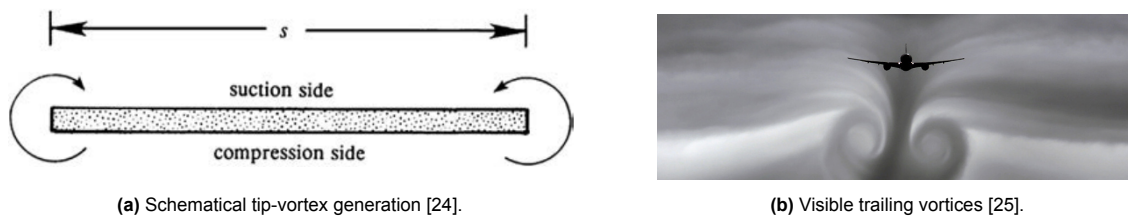
<div align="center">**Figure 2.5:** Tip-vortex effect caused by finite span foil.</div>

will be much lower than on the compression side; this is what causes the lift force. For a finite-span foil, this also means that a flow around the tip of the foil is created. As shown in Figure 2.5, the resulting vorticity is oriented in the stream-wise direction. Exposed to the flow, these vortices trail the foil and dissipate additional energy, reflected in the induced drag. A distinction can be made between low and high aspect-ratio surfaces [26]. The aspect ratio is the ratio of the span over the chord length. Approaching an infinite aspect ratio approaches the 2-dimensional case.

$$AR = \frac{s}{c} \qquad\qquad (2.6)$$

Generally, aspect ratios above five are considered high, aspect ratios below three are low, and aspect ratios below one are seen as very low. It will be shown in 2.1.5 that a wind-assisted ship deals with both high and very low aspect ratio lifting surfaces.

High Aspect Ratio Surfaces
The effects of a finite span wing on lift and drag can be predicted using lifting line theory [24], which simplifies the wing to a set of vortices. It was shown for the 2D case that a bound vortex placed into the foil can describe the lift, and that the effect of the finite wing results in an additional tip vortex. The

(a) Modeling lift through the bound vortex.

(b) Modeling tip effects through the tip vortices, resulting in a horseshoe vortex.
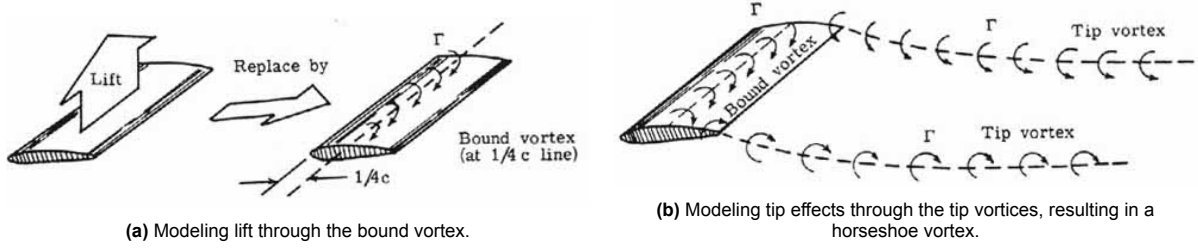
Figure 2.6: Vortices used to model a foil in lifting line theory [27].

combination of these two elements in discrete sections is the basis for lifting line theory, shown in Figure 2.6.

This vortex system is called a horseshoe vortex. The effect of the trailing tip vortices is reflected in a downwash under the wing, distributed in the spanwise direction. This change in flow changes the effective angle of attack and, as such, is the cause for the additional drag and reduced lift of a finite wing. Integrating along the span gives the downwash for any point y_i:

$$w(y_i) = \frac{1}{4\pi} \int_{-s/2}^{s/2} \frac{d\Gamma}{dy} \frac{dy}{y_i - y} \tag{2.7}$$

The effective angle of attack then becomes:

$$\alpha_{e,i} = \alpha - \tan\left(\frac{w(y_i)}{U}\right) \tag{2.8}$$

With the lift vector rotating back because of the shift in α, the lift and drag are corrected for each element along y:

$$dF_L = dF_{L,2D} \cos\left(\tan\left(\frac{w(y_i)}{U}\right)\right) \tag{2.9}$$

$$dF_{D,\text{induced}} = dF_{L,2D} \sin\left(\tan\left(\frac{w(y_i)}{U}\right)\right) \tag{2.10}$$

Filling in $dF_{L,2D} = \rho U \Gamma dy$ gives:

$$dF_L = \rho U \Gamma dy \tan\left(\cos\left(\frac{w(y_i)}{U}\right)\right) \approx \rho U \Gamma dy \tag{2.11}$$

$$dF_{D,\text{induced}} = \rho U \Gamma dy \tan\left(\sin\left(\frac{w(y_i)}{U}\right)\right) \approx \rho w \Gamma dy \tag{2.12}$$

where the approximations result from assuming that the downwash is much smaller in magnitude than the incoming flow, i.e. the small angle approximation.

It can be seen from Equations 2.11 and 2.12 that the lift has a linear, and drag a quadratic relation to circulation, considering the downwash is also a function of circulation. Due to this quadratic dependency, local variations in downwash will always lead to increased drag, lowering the lift-to-drag ratio. Therefore, the most efficient foil is one with a constant downwash $\frac{dw}{dy} = 0$. Mathematically, this is achieved using an elliptical lift distribution. In that case, the downwash is a constant, which leads to simple equations for lift and drag coefficients:

$$C_L = \frac{K \sin \alpha}{1 + \frac{K}{\pi \overline{AR}}} \tag{2.13}$$

$$C_{D,\text{induced}} = \frac{C_L^2}{\pi \overline{AR}} \tag{2.14}$$

where $\overline{AR}$ is the average aspect ratio of the elliptical surface. In the limit of $\overline{AR} \to \infty$, the lift approaches the 2D case of Equation 2.5, and the induced drag approaches zero. These equations also clearly show that the induced drag is a significant component, since it scales with the square of the lift.

In practice, it is often not feasible to design lifting surfaces with an elliptical lift distribution. However, it would be beneficial to still use these simplified equations. For this, the Oswald efficiency factor e is defined [28], so that:

$$C_{D,\text{induced}} = \frac{C_L^2}{e\pi \overline{AR}} \tag{2.15}$$

The Oswald efficiency is 1 for an elliptical distribution, and values down to 0.6 are commonly encountered.

There are multiple limitations to this approach. First, interactions between the trailing vortices are neglected, assuming a perfect 'sheet' behind the foil. It ignores the physical structure of the wing and whichever object it may be connected to. For each segment, the flow is assumed to be 2D, so lift remains linear. This may not be so in practice when looking at large angles-of-attack, or when the aspect ratio of the wing is low.

Low Aspect Ratio Surfaces
The generation of lift through circulation is the basis for deriving the classical lifting line theory. However, this mechanism of linear lift is no longer dominant for low aspect ratio surfaces. Instead, a non-linear component takes over as the aspect ratio decreases. In general, lift and drag can therefore be decomposed into a linear and non-linear component, with their relative significance depending on the aspect ratio:

$$C_L = C_{L,\text{linear}} + C_{L,\text{non-linear}} \tag{2.16}$$

$$C_D = C_{D0} + C_{D,\text{induced}} + C_{D,\text{non-linear}} \tag{2.17}$$

The value for the zero-lift drag coefficient C_{D0} depends on the shape of the object, the linear lift component was defined in Equation 2.13, and the induced drag in Equation 2.15. The non-linear contributions still have to be determined.

The flow around low aspect ratio surfaces was investigated in detail by Hörner [26]. Considering the extreme case, i.e. a plate with an infinitely long chord ($AR \rightarrow 0$), no lift is generated through circulation as the leading and trailing edges are infinitely far away. In that case, the lift comes from the deflection of the flow when encountering the angled plate, with a (tip) vortex sheet coiling up the lateral edges of the surface. The component of the flow that is normal to the plate causes the lift. This can be seen as a form of drag, with a component in the direction of the lift vector, which is why it is often referred to as cross-flow drag. The normal force component can be described using the formula for drag, with the velocity component normal to the surface:

$$F_N = \frac{1}{2}C_{D90}\rho(U\sin\alpha)^2 \tag{2.18}$$

The component of this force in the direction of the lift, in non-dimensional form, is:

$$C_{L,\text{non-linear}} = C_{D90}\sin(\alpha)^2\cos(\alpha) \tag{2.19}$$

Similarly, the component in the direction of the drag:

$$C_{D,\text{non-linear}} = C_{D90}\sin(\alpha)^3 \tag{2.20}$$

Here, C_{D90} refers to the cross-flow drag coefficient, which is the drag coefficient of the object, oriented at 90° to the flow. In practice, values are found to deviate from the theoretical drag coefficient. Especially for small angles, the flow is not fully separated, leading to lower drag than the cross-flow coefficient would predict. Edge effects are important, with sharp-edged plates leading to higher coefficients than rounded ones. Generally, the cross-flow drag coefficient will have to be corrected to match specific cases.

2.1.3. Sail Interaction Effects

A distinct mechanism comes into play when looking specifically at the sails. In many wind-assisted ship designs, including *Silenseas*, multiple sails are mounted in series to form an array of high-aspect-ratio wings. This causes interactions, as the trailing vortices from the upstream wings will disturb the inflow of

the downstream wings. While these effects are generally solved numerically, a semi-empirical method was developed by Bordogna [29], based on the work of Roncin and Kobus [30] on the interaction between racing sailboats.

In this model, the interaction is modeled as a change in the flow field due to the lift and drag of the upstream sails. It computes the impact of lift and drag separately. Lift is based on the horseshoe vortex theory, and drag is represented by viscous component. In that way, the sails are simplified to mere generators of lift and drag, resulting in a change of flow speed and angle for the posterior sails. The flow field due to the interaction of N sails can then be written as:

$$\vec{v} = \vec{v_{\infty}} + \sum_{i=1}^{N} \vec{v}_{\text{HSV},i} + \sum_{i=1}^{N} \vec{v}_{\text{visc},i} \tag{2.21}$$

The anatomy of the horseshoe vortex was previously discussed in the context of forces on finite wings in 2.1.2. The vortex strength can also be found from the lift directly:

$$\Gamma = \frac{F_L}{\rho s v_{\infty}} \tag{2.22}$$

The velocity field due to a horseshoe vortex with strength Γ can be described analytically through mathematical formulations. The viscous component due to drag only influences the magnitude of the velocity field, according to a semi-empirical model:

$$\vec{v}_{\text{visc}} = \vec{v_{\infty}} \left(1 - 0.98 \left[\frac{x}{C_D c} \right]^{-0.5} \left[1 - \left(\frac{2y}{1.14 \left(C_D c x \right)^{0.5}} \right)^{1.5} \right]^2 \right) \tag{2.23}$$

Validation of this simple model by Bordogna showed that an accurate flow prediction due to interactions is only possible for some apparent wind angles. Reasonable agreement between two sails is only found for 0°<AWA<45° and 165°<AWA<180°. A more accurate account of interaction effects still relies on more complex numerical models.

2.1.4. Ship Resistance

Larsson et al. [31] give a detailed overview of the hydrodynamic resistance of straight-sailing ships. The ship's thrust must balance this resistance to move forward at the desired speed. Expressed as non-dimensional coefficients, it can be decomposed into the following components:

$$C_{D,\text{ship}} = \overbrace{\underbrace{C_{D,\text{flat plate}} + C_{D,\text{roughness}} + C_{D,\text{form fric.}}}_{C_{D,\text{friction}}} + C_{D,\text{form press.}}}^{C_{D,\text{friction}}}_{C_{D0}} + C_{D,\text{wave-making}} + C_{D,\text{wave-added}} \tag{2.24}$$

The friction drag is further subdivided into a flat plate, roughness, and form friction component. *Flat plate* resistance is a measure of the frictional resistance purely due to the tangential forces between water flow and the hull's wetted surface. This resistance would be measured on a thin plate traveling through the water at ship speed, with an area equal to that of the submerged hull. The *roughness* of the surface will increase the resistance further. For a flat plate, the velocity outside the boundary layer equals the undisturbed velocity everywhere. This is not the case for a ship hull, where the deflection of flow will cause velocity gradients. The *form friction* component accounts for this. The *form pressure* drag is caused by the pressure gradient along the hull. Analogous to the form drag on a foil, the pressure at the bow will be increased, while the pressure at the aft will be lower, causing a pressure drag.

Next to these expected friction and pressure components, previously referred to as C_{D0}, additional components must be considered because of the water's free surface. These are the wave-making and wave-added resistance components. The pressure variation at the mean water level is considerable for ships since the hull pierces the free surface, causing waves. This can be explained by the dynamic boundary condition, stating that pressure must be continuous across a fluid interface. The condition can only be satisfied if the water level is higher in high-pressure regions and lower in low-pressure

regions. In calm water conditions, the resulting wave pattern is steady with respect to the moving hull, with the energy contained in maintaining this pattern reflected in the *wave-making* resistance. The wave-making resistance gains relevance at higher Froude numbers. If the water is not calm, the *Wave-added* resistance is the environmental force in reaction to the ship responding to free-surface waves. Even though it can significantly contribute to overall resistance, it is usually considered separate from the self-induced resistance components [32].

2.1.5. Sailing Balance

Forces and Moments

For a sailing ship, the force balance turns from a 1 DOF problem into a 4 DOF problem. Instead of just considering the equilibrium in X, the side force Y, the yawing moment N, and rolling moment L also have to be balanced.
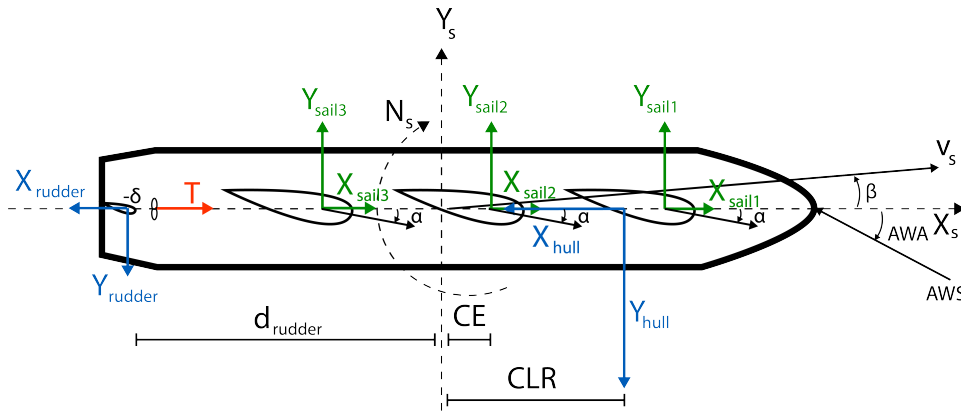
Figure 2.7: Free-body diagram of the balance for a wind-assisted ship. (Extension of Figure 1.2)

Starting with the balance in the xy-plane, it can be seen in Figure 2.7 that all force components besides the thrust are a result of lift and drag forces, decomposed into a ship-fixed reference frame:

$$
\begin{align}
X_{\text{sails}} &= F_{L,\text{sails}} \sin(AWA - \alpha) - F_{D,\text{sails}} \cos(AWA - \alpha) \tag{2.25a} \\
X_{\text{hull}} &= F_{L,\text{hull}} \sin(\beta) - F_{D,\text{hull}} \cos(\beta) \tag{2.25b} \\
X_{\text{rudder}} &= F_{L,\text{rudder}} \sin(-\delta - \beta) - F_{D,\text{rudder}} \cos(-\delta - \beta) \tag{2.25c}
\end{align}
$$

$$
\begin{align}
Y_{\text{sails}} &= F_{L,\text{sails}} \cos(AWA - \alpha) + F_{D,\text{sails}} \sin(AWA - \alpha) \tag{2.26a} \\
Y_{\text{hull}} &= F_{L,\text{hull}} \cos(\beta) + F_{D,\text{hull}} \sin(\beta) \tag{2.26b} \\
Y_{\text{rudder}} &= F_{L,\text{rudder}} \cos(-\delta - \beta) + F_{D,\text{rudder}} \sin(-\delta - \beta) \tag{2.26c}
\end{align}
$$

These lift and drag forces follow from the analysis of foils in 2.1.2. Sails can be seen as high aspect ratio wings exposed to the apparent wind, for which the incoming flow angle can be controlled actively through α. For a better overview, the forces of individual sails are combined into a single force acting at the center of effort.

The hull can be analyzed as a low aspect ratio appendage since its draft (span) is much lower than its length (chord). The lift through cross-flow drag creates a side force based on the drift angle β. The rudder is a high aspect ratio device that can actively be controlled by altering the rudder angle δ.

The described forces do not apply at the same position but are longitudinally offset. This leads to the creation of yaw moments, denoted by N. Defined with respect to the ship-fixed reference frame, the relevant moment arms are the CE, the CLR, and the rudder position:

$$
\begin{align}
N_{\text{sails}} &= -CE \cdot Y_{\text{sails}} \tag{2.27a} \\
N_{\text{hull}} &= CLR \cdot Y_{\text{hull}} \tag{2.27b} \\
N_{\text{rudder}} &= -d_{\text{rudder}} \cdot Y_{\text{rudder}} \tag{2.27c}
\end{align}
$$

The final balance to consider is in heel. Contrary to the other forces and moments, this is the only inherently stable equilibrium due to the restoring qualities of the righting moment of the hull. Still, the moment will cause the ship to heel with an angle φ. For small heel angles, the moment balance can be defined as:

$$CE_z \cdot Y_{\text{sails}} = RM \tag{2.28}$$

with C_z denoting the vertical offset of the center of effort, with respect to the waterline, and RM the righting moment of the hull, defined as:

$$RM = \rho g \nabla \overline{GZ} \tag{2.29}$$

For quasi-static moments, the righting arm $\overline{GZ}$ is related to the heel angle according to a curve of intact static stability [32], defined as:

$$\overline{GZ} = \overline{GM} \sin \varphi \tag{2.30}$$

This means the sail forces are directly related to a resulting heel angle. The metacentric height can be assumed constant for small heel angles since geometric variations of the submerged hull are minimal.

A secondary effect of the heel angle is yet to be acknowledged. When discussing sailing ships, resistance and lateral forces are seen as a function of the drift angle since that represents the angle of attack in the analogy of a foil. However, the heeling angle also increases resistance due to the change in the submerged hull geometry. It can be assumed that for small heel angles, the resistance is insensitive to changes in heel [33].

Here, the sailing forces only refer to the forces due to the sails. However, all geometry above the water surface will cause additional forces on the ship. This is referred to as the windage of the ship. Especially considering the large superstructures on cruise ships, this will be relevant to include.

Sailing Efficiency

If the goal is to generate a forward thrust using wind-propulsion, this inherently implies the generation of a side force due to the lift and drag of the sail, as shown in Equation 2.26a. The hull will have to balance these side forces, according to Equation 2.26b, ideally without causing too large of a moment, to limit the rudder deflection. The hull can also be optimized to generate side force more efficiently, but this usually comes with a penalty in straight-sailing resistance. Investigating ship hulls in oblique flows regarding efficient side force production is prevalent in the analysis of sailing yachts.

The effective draft metric by Gerritsma and Keuning [34] was introduced for this. It describes how effectively a hull can generate side force when sailing with a drift angle. Non-dimensionalized by the ship's draft:

$$T_e/T = \sqrt{\frac{A_w AR_{\text{eff}}}{2}} \tag{2.31}$$

While in theory, the aspect ratio should be equivalent to the one used in the derivation of lifting line theory, as defined in Equation 2.6, the behavior of a ship hull differs from the theoretical expectation. A simple approach is to multiply the aspect ratio by two, thereby assuming a symmetry condition at the water surface. In general, the effective aspect ratio AR_{eff} is therefore determined artificially so that:

$$C_x = C_{x0} + \frac{C_y^2}{\pi AR_{\text{eff}}} \tag{2.32}$$

In this equation, AR_{eff} also contains the Oswald efficiency. Sometimes, the Oswald efficiency is also included separately in the formula. A limitation of this approach is that the additional non-linear drag contribution due to the low aspect ratio of the hull is not taken into account; see Equation 2.17 and Equation 2.20. Also, Keuning and Gerritsma use C_x and C_y analogous to C_D and C_L. This neglects the difference between the frames of reference for a foil and a ship. Lift and drag are defined with respect to the incoming flow, while resistance and side force are defined with respect to the object, i.e. the hull. For small leeway angles, this difference can be assumed negligible.

2.1.6. Ship Maneuvering Theory

Apart from sailing yachts, the performance of ships in oblique flows is also analyzed in the context of maneuvering. The goals in maneuvering analyses are slightly different. In maneuvering, transient behavior is important (stopping, changing course), so emphasis is put on the study of e.g. added mass coefficients and the response at different yaw rates. For a sailing equilibrium, this is not very relevant. The range of conditions also differs. While in maneuvering, all drift angles have to be regarded, considering the ship might also reverse, in sailing one is only interested in the response at small drift angles, albeit with a larger expectation of accuracy. These things considered, there is still significant value in looking at maneuvering models and tools.

Fundamentally, the approach is similar to the definition of $C_{L,D,N}$ based on the low aspect ratio wing theory. A large variety of maneuvering models exist, using different coefficients and non-dimensionalizations. The model described here is the one that is used by the later described SURSIM tool.

The side force and yaw moment can be modeled as having a linear and a non-linear component, analogous to linear and non-linear lift components, defined by maneuvering coefficients [35]:

$$X = X_{uu}u^2 + X_{vv}v^2 \cos^2\beta \tag{2.33a}$$

$$Y = Y_{uv}uv \cos\beta + Y_{\text{non-lin}} \tag{2.33b}$$

$$N = N_{u|v|}u|v| \cos\beta + N_{\text{non-lin}} \tag{2.33c}$$

with terms including the yaw rate r omitted since it is zero for a steady straight sailing condition. For the linear part, the slender-body strip theory is the most common approach. The fundamental assumption in strip theory is that the force on a hull segment is based on the rate of change of fluid momentum m. The linear coefficients can then be described in the following way:

$$Y_{uv} = \int_{\text{APP}}^{\text{FPP}} \frac{dm_{yy}}{d\zeta} d\zeta \tag{2.34a}$$

$$N_{u|v|} = \int_{\text{APP}}^{\text{FPP}} \frac{dm_{yy}}{d\zeta} x d\zeta \tag{2.34b}$$

with ζ being the distance from the forward perpendicular of the ship. The non-linear components require an extension of strip theory to include cross-flow drag effects. The associated terms are described by Hooft and Quadvlieg [36], [37], forming equations with C_{D90} integrated over the ship sections:

$$Y_{\text{non-lin}} = -\frac{1}{2}\rho \int_{\text{APP}}^{\text{FPP}} C_{D90}(x)T(x)v(x)|v(x)|dx \tag{2.35a}$$

$$N_{\text{non-lin}} = -\frac{1}{2}\rho \int_{\text{APP}}^{\text{FPP}} C_{D90}(x)T(x)v(x)|v(x)|xdx \tag{2.35b}$$

The analytical description ends here. Empirical models are used to estimate the remaining unknown parameters X_{uu}, X_{vv}, m_{yy}, and $C_{D90}(x)$, e.g. based on captive model test results.

2.1.7. Linking Maneuvering and Airfoil Theory

While not used in the later calculations, it was confirmed that by applying a linearization, the described maneuvering model corresponds to the low aspect ratio wing theory. For small angles, one can assume $\alpha \approx \beta$, implying the lift is approximately equivalent to the side force, and the drag is approximately equivalent to the resistance. Then, the following relations apply:

$$C_{D0} \approx \widetilde{X}_{uu} \tag{2.36a}$$

$$C_{D,\text{induced}} \approx \widetilde{X}_{vv} \tag{2.36b}$$

$$C_{L,\text{linear}} \approx \widetilde{Y}_{uv} \tag{2.36c}$$

with the tilde denoting the non-dimensional form of the parameter. In airfoil theory, the non-linear component is also defined relative to the body and not relative to the incoming flow, see Equation 2.18. Therefore, non-dimensionalizing Equation 2.35a and inserting $U = v_s \sin(\beta)$ gives identical equations for both theories. The only caveat is that Hörner defines his equation using $\sin^2(\alpha)$, which is not valid for negative angles, as it should then be '$\sin(\alpha)|\sin(\alpha)|$' instead.

2.2. Computational Tools

2.2.1. XFOIL

XFOIL [38] is a well-established tool for analyzing foils in 2D, allowing for a rapid determination of lift and drag curves. It uses a panel method to solve the potential flow equations numerically for complex geometries. If a field is inviscid, rotation cannot be generated, leading to a conservative flow. In this case, one can define a potential, a scalar function whose gradient represents the flow velocity. The flow field around an airfoil can then be described by the superposition of a free-stream flow, a source sheet to deflect the flow, and a vortex sheet to simulate the lift. Correction factors for the source sheet account for viscous effects. The panel method is a boundary element method, as the individual panels only need to be defined at the boundaries and not in the whole domain. This leads to quick computation times. The cells are defined around the surface of the foil and in a single line in the wake starting from the trailing edge.
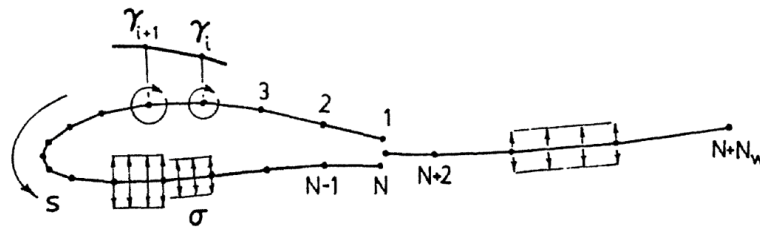
Figure 2.8: XFOIL panel method, s being the coordinate along the foil surface and into the wake, σ the source strength, and γ the circulation strength defined for each panel [38].

While some convergence issues for very low Reynolds numbers and for situations with strong separation (e.g. close to or beyond stall) are known to pose problems, accuracy is generally very good. However, as described in Section 2.1, the behavior of foils in 3D can vary significantly from the 2D estimate.

2.2.2. DESP

Estimating the ship resistance is crucial in the design of any seagoing vessel. Holtrop and Mennen [39] developed an elaborate regression model for resistance estimation based on the database of the Netherlands Ship Model Basin. Around a dozen parameters define the geometry of the hull, along with appendages. Empirical relations determine the resistance components, described in more detail in 2.1.4. At MARIN, DESP [40] is a tool used for resistance estimation using the Holtrop and Mennen method. It has been in use since 1987, resulting in extensive knowledge about the applicability and limitations of the method. Generally, differences within 10% are observed in the comparison to model tests. It is important to note that the Holtrop and Mennen method will typically give the resistance assuming an optimized hull form for the chosen speed/Froude number. If the hull geometry is not optimal for the given speed, i.e. for off-design conditions, errors can be larger.

An example resistance curve, in this case the one calculated for a scaled version of the MARIN Ferry, is shown in Figure 2.9. A difference to the analytical ship resistance model is the correlation allowance resistance, defined in the Figure as 'correlation'. This component is a correction factor of the full scale resistance extrapolated from model tests. The primary effects accounted for are hull roughness, non-modeled details (e.g. anodes, welds), and air resistance.
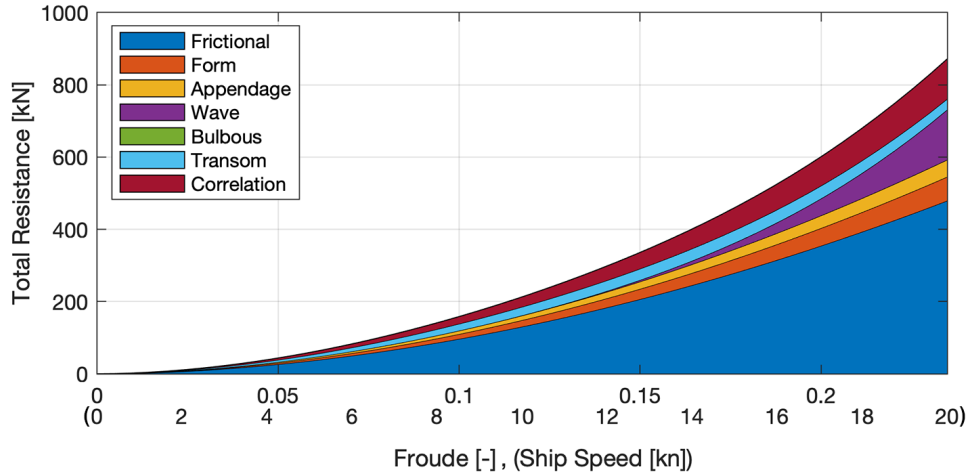
Figure 2.9: Resistance components as a function of Froude number and ship speed for a scaled version of the MARIN Ferry. L: 190m, B: 25m, T: 9m

2.2.3. SURSIM

SURSIM is a MARIN proprietary tool to calculate the hydrodynamic reaction forces of a ship, intended for the simulation of maneuvering without added waves, for example, for application in ports and inland waterways. It is based on the slender-body strip theory, taking into account the non-linear cross-flow components, based on the maneuvering theory described in Section 2.1.6 'Ship Maneuvering Theory'. The empirical foundation is based on data from twin-screw ferries, cruise ships, and motor yachts, so the highest accuracy is expected when applied to vessels that fit this category.

Validation
Validation of the tool has been conducted at MARIN by Toxopeus. A first study [35] included the MARIN Ferry model, which is also the base model for this study. It found good agreement with CFD results, but some over-prediction of the forces at the bow was noted for ships with high block coefficients. However, only the linear components Y_{uv} and N_{uv} were investigated, not the cross-flow drag components. In a later study [41], Toxopeus included non-linear components, yielding mixed results. However, this comparison did not include the MARIN Ferry, and no variation of deadrise or skegs.

2.2.4. ReFRESCO

ReFRESCO [42] is a computational fluid dynamics (CFD) software package for maritime applications developed at MARIN together with several universities and partners. It can solve unsteady, compressible viscous flows based on the Navier-Stokes (NS) equations. The general issue with solving the NS equations is that in most problems, the encountered flow is turbulent. Turbulent flows are highly unsteady on a wide range of lengths and time scales, making direct numerical simulation challenging and time-consuming. ReFRESCO is a Reynolds-averaged Navier-Stokes solver (RANS). This means that small-scale perturbations in the flow are time-averaged. An additional turbulence model then accounts for modeling discrepancies. The appeal of this approach comes from the fact that, in most cases, one is not interested in fully resolving the detailed flow throughout the whole domain but rather in specific properties, such as the distribution of forces on a body. RANS is often also the only viable solution in terms of complexity and computational power.

Governing Equations
The equations described here form the basis for the RANS method [43]. For an incompressible flow, the averaged continuity and momentum equations are:

$$\frac{\partial (\rho \bar{u}_i)}{\partial x_i} = 0 \tag{2.37a}$$

$$\frac{\partial (\rho \bar{u}_i)}{\partial t} + \frac{\partial}{\partial x_j}(\rho \bar{u}_i \bar{u}_j + \underbrace{\rho \overline{u_i' u_j'}}_{cov}) = -\frac{\partial \bar{p}}{\partial x_i} + \frac{\partial \bar{\tau}_{ij}}{\partial x_j} \tag{2.37b}$$

with $\bar{\tau}_{ij}$ being the (mean) viscous stress tensor:

$$\bar{\tau}_{ij} = \mu \left(\frac{\partial \bar{u}_i}{\partial x_j} + \frac{\partial \bar{u}_j}{\partial x_i} \right) \tag{2.38}$$

A caveat is apparent. While averaging a linear term gives an equivalent, averaged term, averaging a product of two terms gives an additional covariance term. Neglecting this term is only possible if the two quantities are uncorrelated since then the covariance is zero. That is not the case, as velocity components will hardly be uncorrelated. This covariance term can be seen in Equation 2.37b, denoted by cov. This term can not be resolved by averaged quantities and is referred to as the Reynolds stress. Turbulence models 'close' the equations by modeling this term; multiple such models are available in ReFRESCO.

The k-ω SST model used in this study is a two-equation eddy-viscosity model. The hybrid model combines the Wilcox k-ω and the k-ϵ models through a blending function. The Wilcox model is active in near-wall and the k-ϵ model in the free stream. Since the former model is more suitable for simulation the flow in the viscous layer, and the latter is ideal for regions far away, blending the two functions gives the best of both [44].

Near-wall Corrections

The previous paragraph underlined the difference between predicting the flow in a near-wall and a free stream. The boundary layer, the transitional region between a boundary (in this case, the hull of the ship) and the free stream flow, features large velocity gradients and can be difficult to predict. The characteristic of the flow depends on the distance to the wall, which is defined through $y+$, the dimensionless distance from the boundary wall [45]:

$$y+ = \frac{u_\tau}{\mu} y \tag{2.39}$$

Figure 2.10 shows how $y+$ denotes different regimes, each showing a distinct relation between $y+$ and the normalized velocity profile $U+$.
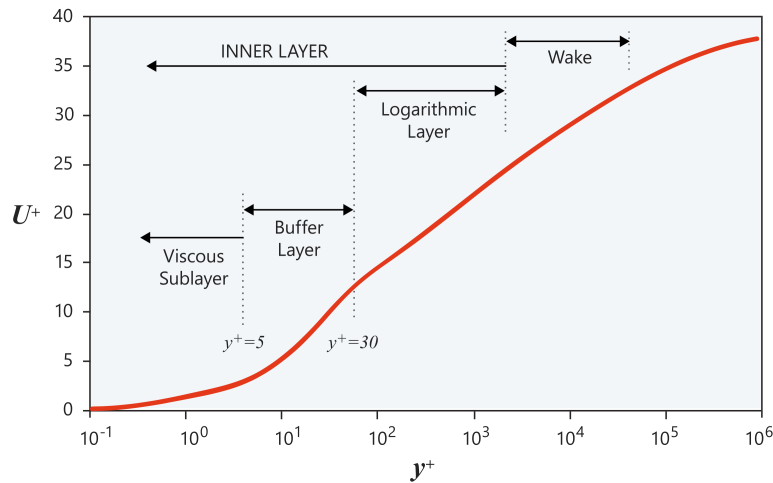
Figure 2.10: Boundary layer regimes as a function of y+ [46].

There are various approaches to resolve the flow in the boundary layer. One way is to integrate the turbulence all the way to the wall. In hybrid models such as the k-ω SST model, the Wilcox k-ω would be active in near-wall regions and resolve the flow down to the wall. For this to work, the mesh has to be fine enough to capture the various layers, which means that the first cell center should fall into the viscous sublayer, ideally around $y+ = 1$. This approach leads to a large number of cells and, therefore, substantial computational time.

Alternatively, so-called wall functions can be used. Wall functions are empirical equations that model the near-wall region, bridging the inner layer with the fully developed region of the flow. In that case,

the first cell center must only be placed in the log-law region, decreasing the refinement necessary in the viscous layer. Overall, the wall function approach is reasonable in many flow conditions, mainly flows with high Reynolds numbers. Accuracy may decrease for low Reynolds number flows, strong body forces, or separated flows [46].

Free Surface

Two common ways to deal with the water's surface in CFD computations are the double-body and the free-surface approach. The free-surface approach is more accurate as it uses a dynamic boundary condition, for which pressure fluctuations lead to a deflection of the free surface, creating waves. This free surface effect corresponds to the additional resistance described in Section 2.1.4 'Ship Resistance'. It was shown that the influence of this resistance component becomes more significant with higher Froude numbers; see Figure 2.9. Therefore, if Froude numbers are relatively low, free-surface effects are negligible, and the simulation time can be greatly reduced by neglecting the free surface. This is referred to as the double-hull approach. Instead of modeling a free surface, a symmetry plane is imposed at the waterline.

Propeller Coupling

The propeller is a complex, unsteady component of the ship. To characterize its flow effectively, various strategies may be employed. The most common approaches, in ascending complexity, are RANS-actuator, RANS-BEM, and RANS-RANS coupling.

In the RANS-actuator method, the propeller is modeled as an actuator disk. The actuator disk describes steady body forces representing the suction action of the propeller, the acceleration of the flow through the propeller, and the swirl behind it. To implement this model, the distribution of forces due to the propeller needs to be defined a priori; they are not adapted based on the CFD environment.

RANS-BEM coupling is more accurate in that regard. The propeller is modeled using a boundary element method (BEM). Iteratively, the wakefield calculated using RANS is used as an input in BEM, where the loading of the propeller is calculated for a complete revolution, leading to an unsteady problem. The time-averaged force field is then used in RANS to adapt the flow, so the RANS computation remains steady. This back-and-forth is repeated until a tolerance criterion is fulfilled. In ReFRESCO, PROCAL is the BEM code used for this coupling. Contrary to the actuator approach, this method can account for the oblique propulsor inflow due to the leeway effect.

For a full unsteady simulation of the ship-propeller interactions, RANS-RANS coupling can be used. Here, the propeller mesh is physically rotated, and the resulting flow is resolved using RANS. This is different from a single RANS simulation using the entire model, as different time scales and simulation settings for the ship and propeller are possible. Still, this approach is by far the most computationally intensive.

Validation

Several validation studies have investigated the use of ReFRESCO to predict side forces. For wind-assisted propulsion, Struijk [47] initially found the resistance and yaw moment to be well resolved using RANS, while the side force deviated by more than 20% from the expected values. Similar errors are reported by Settels [48] in a later study.

Van der Kolk compared RANS simulations of various hull forms and appendage variations with experimental data [49] and defined best practices and a method to determine the numerical uncertainty [50]. Especially for the side force, much better agreement with experimental data was found. Average comparison errors were around 1-2%. It was found that modeling separation behavior and the evolution of vortices while maintaining a computationally affordable simulation is the principal challenge. Grids with a larger refinement diffusion (i.e where the domain refinement is prioritized over the ship surface refinement) showed superior performance. The influence of cell size at the ship hull boundary was most apparent for the side force uncertainty. The EASM turbulence model leads to the best results, but the slightly less expensive k-ω SST model is also a common choice. While it is acknowledged that the side force prediction is the most challenging, good agreement was found for all force components and all hull forms.

Most recently, Giovannetti et al. [51] compared the results from towing tank, full-scale CFD, and model-scale CFD computations for an appended hull at varying leeway angles. The k-ω SST model was used, and the free surface was approximated using a panel method, leading to computational times between 7 and 15 hours. All hydrodynamic coefficients are within uncertainty limits when comparing model-scale CFD and towing test results. Full-scale CFD results for side force and yawing moment deviate from experimental results by around 25%.

At MARIN, ReFRESCO is the preferred tool for estimating forces on wind-assisted ships, and it has been successfully used in various previous studies. In [52], [53], the double-body approach was compared to free surface modeling. Trends appear consistent for all parameters and geometric variations at low Froude numbers. This makes it possible to adapt the resistance allowance of the double-body results based on a smaller subset of free-surface computations.

A study at MARIN investigated forces and moments due to drift for the MARIN Ferry design, with different skegs [54] in a maneuvering context. Experimental results were compared to double-body calculations in ReFRESCO. The resulting forces match the experimental data well, but the accurate prediction of the center of later resistance (CLR) still proves challenging, and deviations between the experimental and numerical data are apparent. In Appendix A, the data from this study is shown.

2.2.5. Sailfish

Sailfish is being developed at MARIN to estimate the performance of ships equipped with wind-assisted propulsion. Various properties of the ship systems are defined and summarized in Table 2.1. As such, implementation of a new design in Sailfish generally requires a preceding analysis of the individual components. The accuracy of Sailfish as a computational tool largely depends on the provided inputs' accuracy. Power prediction programs (PPP) can be created using this data. A PPP estimates a wind-assisted ship's fuel consumption/emissions for varying wind speeds and directions [55]. The expected emissions on a specific route and for a specific operational profile can be determined by multiplying the PPP matrix with a wind statistics matrix.

Table 2.1: Overview of various properties to be defined in Sailfish for the power prediction of wind-assisted ships.

System	Component	Properties
Ship Hull	Properties	Principal dimensions, design coefficients, stability
	Forces	Resistance, maneuvering forces
Rudder	Location/Dimensions	Number of rudders, position, and sizing
	Forces	Unified Rudder Model [56]
Powertrain	Engine, Gearbox, Shaft	Model parameters to find emissions at different loading conditions
	Propeller	Fixed and variable pitch propeller models
Auxiliary Power	Engine	Various models to find emissions for a set auxiliary power consumption
Wind Propulsion	Type	Flettner, suctionsail, wingsail, or soft sail configurations
	Location/Dimensions	Number of sails, position, and sizing
	Forces	For wingsail: table of lift and drag coefficients for varying angles of attack

Working out the equilibrium state of the ship for all wind conditions is based on the Equilibrium and Speed (E&S) solver. Such a state is achieved when the desired ship speed, drift angle, rudder angle, wind propulsor settings, and propeller RPM lead to zero acceleration. This equilibrium can be found in up to 4 DOF (surge, sway, yaw, roll). Some essential parameters, such as the hydrodynamic coefficients of the hull, are passed to E&S as discrete arrays. A cubic spline interpolation is used to interpolate between values. As this leads to a smooth and accurate interpolation, no artifacts in the results are expected by using this approach.

2.3. State of the Research

2.3.1. Hull Shapes

The hull shape greatly affects the performance of a wind-assisted ship, as it is used as a lifting device to counter the side forces generated by the wind propulsion. While for a conventionally propelled vessel, the objective is to minimize resistance for the intended speed, two other objectives come into play for a wind-assisted ship. First, the lift-to-drag ratio for the range of encountered leeway angles should be as high as possible. Secondly, the center of lateral resistance (CLR) of the hull should fall close enough to the center of effort (CE) to avoid generating a large moment on the ship.

Systematic Variations in the DSWA Series
A systematic approach to this design problem was taken by the Delft Systematic Wind-Assist Series (DSWAS) developed by Struijk [47]. This set of hull forms comprises variations of prismatic and midship coefficient, draft-to-length ratio, and deadrise angle, with the Dykstra Ecoliner concept design by Nikkels [57] as the parent hull form.

Item	Value
L	138m
B	18.2m
T	6.5m
Δ	11850t
Fr	0.17

Table 2.2: Main particulars of the Ecoliner hull.
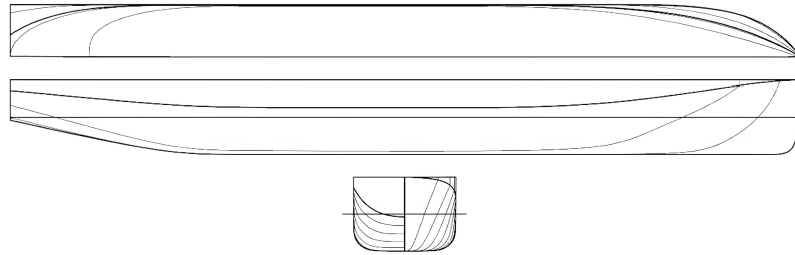
Figure 2.11: Ecoliner parent hull lines [49].

If the prismatic coefficient C_P is raised by increasing the bilge radius, a weaker bilge vortex and lower side force generation are expected. However, if C_P is raised by lengthening the parallel mid-body, the vortex strength would increase due to longer bilges, leading to higher side force generation. It is therefore argued that including C_P is mainly to make the series applicable to a range of vessel types. The midship coefficient C_M was included since sharp-bilged vessels are seen to generate more side force.

Based on the series, Struijk constructed the following empirical formulations for the hydrodynamic coefficients:

$$Y(\beta) = \beta 1.144\frac{T}{L} + \beta^2 \left[-0.252C_p + 1.358C_m + -1.081\frac{A_{wp}}{A_w} \right] \tag{2.40a}$$

$$N(\beta) = \beta \left[1.732\frac{T}{L} + -0.005C_p + 0.051C_m \right] \tag{2.40b}$$

While not in the initial set, the series was later extended by Van der Kolk to also include a deadrise angle parameter [49], as it was found that adding a deadrise leads to a potentially higher side force and lower drag. Also, while the initial study included draft as a parameter, this was later replaced by the non-dimensional draft-to-length ratio. Consensus exists that a higher draft will increase side force production as the aspect ratio of the hull increases, as also detailed in the theory of low-aspect-ratio foils, in Section 2.1.2 'Forces on a Foil in 3D'.

Table 2.3: Design space for hull variations in the Delft Systematic Wind-Assist Series.

Hull	C_p	C_m	L/T	Deadrise
Parent	0.764	0.942	21.23	0°
Series Min	0.686	0.787	16.67	0°
Series Max	0.84	0.984	23.81	14°

Table 2.4: Design space for hull variations in the MARIN systematic investigation.

Hull	B/T	L/T	Deadrise
Parent	2.8	21.23	0°
Series Min	1.992	12.52	0°
Series Max	4.032	33.49	14°

Research at MARIN

At MARIN, a similar variation of hull forms, also based on the Ecoliner hull, was studied using CFD simulations [52]. This included 80 variations of beam-to-draft, length-to-draft, and deadrise angle, shown in Table 2.4. The main trade-off was found to be the beam-to-draft ratio. A deeper hull will generate lift more efficiently and have a lower base resistance. A wider hull is more stable, supporting larger sail forces at the same heel limit.

The length-to-draft ratio was found to have little effect on the lift generation, while drag increased. In this study, deadrise did not have an apparent impact on lift or drag as long as the draft was kept constant. The yaw moment is most related to the lift. Hulls with high lift force generations also create the strongest moments.

As a follow-up, specific investigations on bow and aft shapes were conducted at MARIN for a wind-assisted bulk carrier design [53]. A first general observation is that at higher leeway angles, the pressure differences between starboard and portside increase most significantly at the bow and aft of the ship, as can be seen in Figure 2.12. The pressure on the portside increases considerably at the bow, leading to a much higher side force generation in that area. This also moves the CLR forward. The distribution is opposite at the aft, where the pressure at the portside decreases. This generates lift in the opposing direction, moving the CLR further forward.
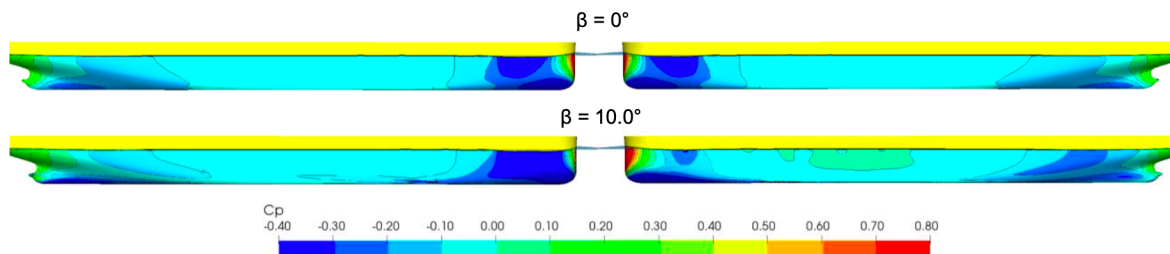
Figure 2.12: Pressure distribution on starboard and portside for zero and 10° (flow from portside) leeway angle [53]. (modified)

The following variations were investigated:

Aftship:
- Reduced waterline width
- Lowered aft contour
- More U-shaped aft section
- More V-shaped aft section

Gondola:
- Skeg-shaped gondola
- Gondola with smoothed bottom

Bow:
- Sharp entrance angle and increased length
- Sharp entrance angle at equal length

The lift-to-drag ratio shows only slight variations for the designs. Slight improvements between 1 and 2.4 percentage points were only found for lowering the aft contour and for the skeg-shaped gondola. The effects on the propeller inflow are neglected. It is argued that these effects would be minimal, in the order of less than a percent. In terms of fuel consumption, none of the designs lead to significant improvements. The lowered aft contour performs best, reducing the fuel consumption by 0.3%.

2.3.2. Rudders

Appendages can play a significant role in the design of wind-assist vessels. The rudder can be seen as a high aspect-ratio foil mounted in the propeller wake for increased force generation. It is an active device, as the generated lift and the generated side force are controlled through the rudder angle. Control of this angle provides maneuverability to the ship by altering the yaw balance.

The knowledge base for design considerations of rudders is extensive for propeller-driven ships [58], [59]. The rudder profile describes the sectional shape of the rudder. This profile determines the key hydrodynamic characteristics, i.e. the lift and drag coefficients with respect to the angle of attack. The rudder area determines the magnitude of the forces induced by the rudder. While a larger rudder can generate more side force, it also creates more drag. A high aspect ratio rudder will create more lift and less drag, but will stall sooner.

Research at MARIN

At MARIN, research specifically on the rudder design for wind-assisted ships [60] has been conducted for a bulk carrier aiming at 25-30% fuel savings through wind-assisted propulsion. The characteristic fuel savings of the ship are important to consider when looking at results from past studies. Side forces increase for higher fuel savings, and propeller wake effects will be less significant. Designs deemed ineffective might actually be efficient for ships aiming for higher savings, as sailing forces increase and therefore efficient side force generation and constraints become more critical. Different rudder variations were investigated using a viscous flow model, accounting for non-linear lift and drag contributions but not for flow-straightening effects. Closing the gap between the hull and rudder reduces straight sailing resistance as it avoids flow separation, leading to additional fuel savings of 0.3%. Concerning other investigated design variations, only the twin rudder showed significant improvements, resulting in further fuel savings of 0.9%. However, these savings are largely irrespective of the wind-propulsion system, as even larger fuel savings of 1.2% were found for the same rudder design but without wind propulsion. The higher aspect ratio of the twin rudder is the main reason for the improved performance. The possible issue of the earlier stall-onset of the twin rudder due to the higher aspect ratio is acknowledged, leaving the question open whether the twin-rudder configuration has acceptable performance at larger rudder angles. A larger overall rudder area could allow for higher side force generation at lower angles of attack.

2.3.3. Additional Appendages

Research by Minami et al.

Rudders are not the only appendage to consider when designing a ship. Minami et al. [61] first investigated the potential of integrating additional underwater appendages specifically for wind-assisted vessels. For a 180m long wind-assisted cargo ship, different fin configurations were investigated for their potential to reduce heel and yaw angles. Towing tests and analytical calculations were conducted for various arrangements. Rectangular fins of varying dimensions were placed around midship or in aft positions, as centerboards or sideboards, always oriented orthogonally to the water surface. All of the configurations decreased the drift angle and the rudder deflection of the ship, while the heeling angle was largely unaffected. The x, y forces and x, z moments are reported for all variations. The centerboard located aft performed best, showing a decrease in drift and rudder angle and a reduction in overall resistance of 4.6%. In that case, drift angles reached up to 3.5°. Retractable designs should be investigated to reduce resistance when the ship is not sailing, and due to possible draft restrictions. The most notable limitation of this study is that the resistance decrease is based on a single wind speed, averaged over all apparent wind angles. The wind speed for this is said to be 15m/s, which would be unreasonably high. It is conceivable that a false unit is reported, and the results are based on a wind speed of 15kn instead. Still, the savings will be significantly impacted by taking lower wind speeds into account.

(a) Cases of fin configurations, fins 1-4 are mounted on each side of the hull, and 5-6 are mounted in the center.

(b) Drift angle under 15kn for varying wind angle.
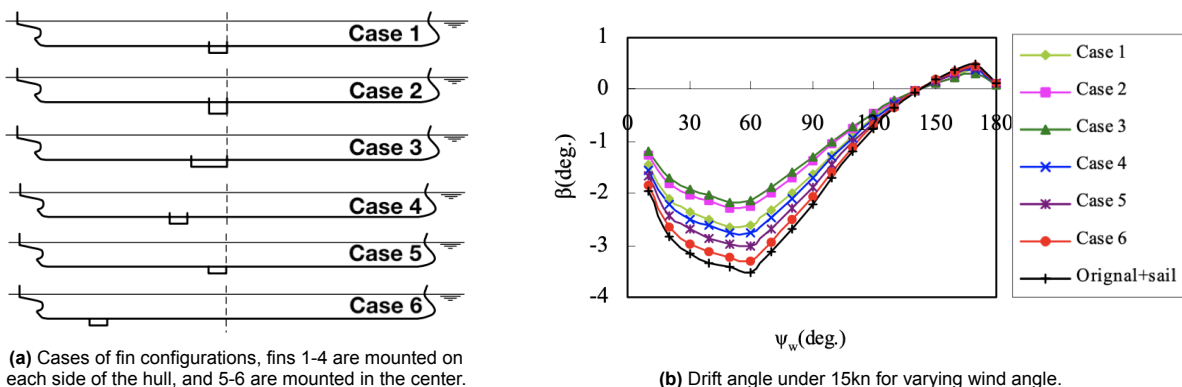
Figure 2.13: Drift angles for different appendage cases [61]. (modified)

Research by Van der Kolk

Van der Kolk built on the findings by Minami et al. as part of his doctoral dissertation [62], and in an associated published article [63]. Instead of fins, bilge keels of varying dimensions and positions are investigated experimentally using straight-line captive tests. As opposed to sideboards, these surfaces are oriented orthogonal to the hull. Bilge keels are beneficial in both moving the CLR aft and reducing its dependency on the drift angle. The length of the bilge keel mainly influenced the side force, while the position of the keel influenced the yaw moment. The device causes separation in the boundary layer of the vessel, significantly reducing the yawing moment. While an increase in the effective draft is demonstrated, the step to investigate how these benefits translate to fuel savings on a wind-assisted ship was not taken.

Research at MARIN

Research at MARIN aimed to investigate these potential fuel-savings [53]. The same vessel as for the earlier described rudder study [60] was used as a reference. Different bilge keel and course fin variations were appended to the hull. All these appendages moved the CLR more aft, and increased the effective draft, confirming the results by Minami et al. and Van der Kolk. However, when implementing the appended hulls in a power prediction program (PPP) and determining fuel savings through a simulated operation, the benefits did not carry over. The increased straight sailing resistance outweighed the better sailing efficiency for all course fin and bilge keel variations. Still, the conclusions drawn from these results do not suggest that bilge keels should not be included in the design of wind-assisted ships. It is argued that bilge keels should be integrated based on seakeeping considerations, outweighing the slight increases in fuel consumption of 0.2 to 0.7%. A case for further investigation of course fins is not given, but the fact that results may vary based on ship type is acknowledged.

Research at SSPA

Giovannetti et al. [51] are the first to discuss the role of low-fidelity tools for estimating the hydrodynamic forces of wind-assisted ships with appendages. It is presumed that coming up with effective designs requires assessing a large variety of appendages at different locations, geometric variations, and angles of attack. This is said to only be possible with lower-fidelity tools with fast execution times. The biggest issue with semi-empirical models is expected to be the complexity of the downwash from upstream appendages, as that is a major limitation when analyzing sailing yachts - the keel downwash significantly affects the effective angle of attack of the rudder.

CFD and towing tank tests were conducted for an appended version of the Oceanbird concept, described later in 2.5. While positive effects on side force generation and CLR are noted, the performance was analyzed using a velocity prediction program (VPP) instead of a PPP, so the impact on fuel savings is unclear. The low-fidelity approach and its limitations are only described qualitatively but were not computed and, therefore, cannot be compared to the CFD and towing tank results.

Research by Kramer and Steen

Most recently, Kramer and Steen [64] numerically investigated various appendages as part of a study on the sail-induced resistance of a 120m long cargo ship. This study followed the holistic approach of looking at the effect of appendages on the final fuel consumption during operation. Two geometries were investigated: bilge keels and a high-aspect center keel. For the center keel, a dynamically-controlled version was also investigated. By having an adjustable angle, the generated side force was decoupled from the drift angle of the vessel so that the keel could be loaded more heavily. The retractability of the keel avoids parasitic drag in unfavorable wind conditions. A system similar to roll-stabilizing fins is hypothesized.

Contrary to the MARIN study, sail area and ship speed were kept variable to determine the importance of these design variations depending on how much the ship is wind-supported. The sail-induced resistance was reduced by a factor of three by implementing the dynamic keel, while bilge keels and static keel only reduced it by around 1.4. This also reflects in fuel savings. Bilge keels only lead to small fuel savings in the extreme cases of either very large sail area ($4000m^2$) or very low ship speed (8kn). If wind propulsion is the dominating thrust provider, these appendages could become beneficial from a fuel-saving perspective as well. The dynamic keel outperformed the other appendages considerably by reaching fuel-savings of more than 4% across all ship speeds and sail sizes, see Figure 2.15.

It is concluded that appendages should always be evaluated with respect to other design constraints. If limits on steerability or heel angles are reached, bilge keels could effectively increase fuel savings by avoiding penalties in the sail area that come into play otherwise. The dynamic keel clearly showed the best performance, but the added complexity of such a system is recognized. The decision to position the keel in the middle of the ship, as opposed to e.g. more toward the aft to generate a moment to offload the rudder more, as the study of Minami et al. would suggest, is not elaborated upon.
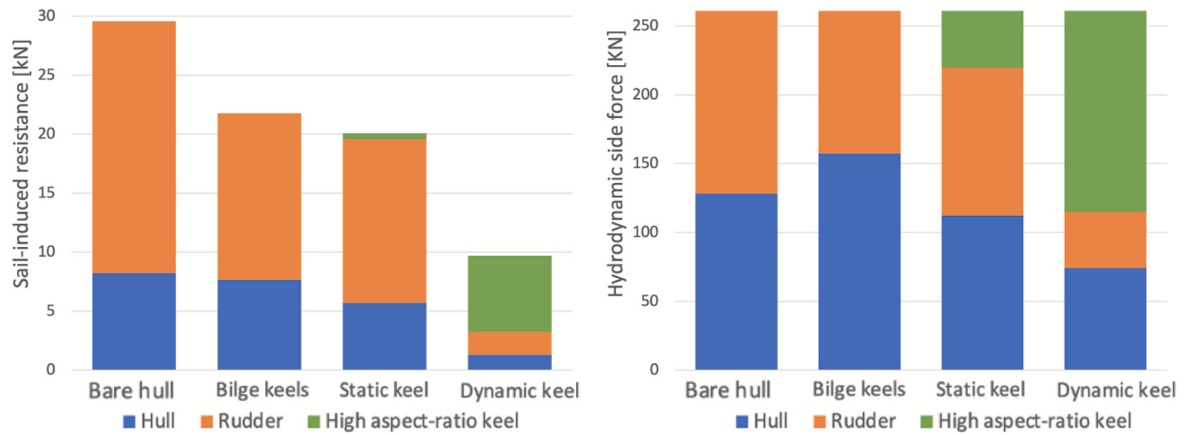
Figure 2.14: Sail-induced resistance and hydrodynamic side force for different appendages [64]. Values are for a ship speed of 12 knots and a side-force-to-resistance ratio of 2.
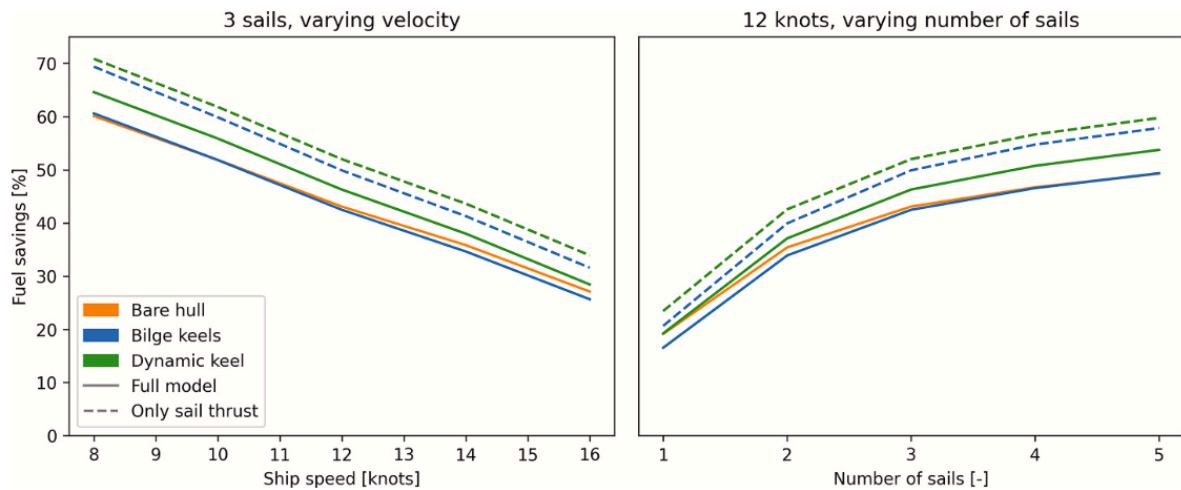
Figure 2.15: Fuel-savings for different appendage cases, as a function of ship speed and sail area [64].

2.3.4. Ballast Systems

Literature on ballast systems designed in the context of wind-assisted vessels is not available, while they are already mentioned in concept designs, discussed later in 2.5. The concept of movable ballast to improve sailing performance has been investigated in the context of competitive sailing. DeBord [65], compared the performance of different methods the center of gravity could be offset on a 24m racing yacht. A fixed ballast was compared to a water ballast and a canting keel (ballast in the form of a hinged keel). Both movable ballast systems outperformed the fixed ballast case by decreasing the resistance for all wind speeds and angles. Direct applicability of these results to wind-assisted ships is not guaranteed. The water ballast case was compared to a ship with the same displacement, meaning that no penalty was attributed to the increase in weight of implementing the system.

On the other hand, most cruise ships already feature a water ballast system for seakeeping and trim. Also, constraints on allowable heeling angles are much stricter on cruise ships compared to a racing yacht, which further promotes the usage of a ballast system.

2.3.5. Regeneration

The development of regenerative braking for maritime applications is limited. Most common are retractable appendages for small sailing vessels, so-called hydro-generators [66]–[68]. These turbines are optimized to recover energy from sailing vessels, with the drawback of increased drag. Vendors of controllable-pitch propellers for sailing vessels also promote regeneration capabilities [69], [70]. Commercial systems have power ratings of 5-3000W at turbine diameters of around 0.2-0.4m. Using the propulsor itself in a regenerative mode is less common, but a case study of a commercial application in a sailing cruise vessel exists [71], [72]. In its regenerative plugin hybrid-electric propulsion system, up to 5kW are generated at a speed of 5kn while sailing.

Most recently, Foundation[0] [73] was presented as an open-source, open-data platform for sharing developments in sustainable maritime travel and hospitality. Hydro-generation is mentioned as a focus point. While no data or full research report has been published as of May 2023[1], results from a case study on a hypothesized wind-powered Panamax are described, shown in Figure 2.16. It can be seen that considerable power can be harnessed with only marginal speed reductions, and that regeneration favors higher speeds. The main challenge is seen in optimizing the propeller geometry for propulsion and regeneration[2].

Figure 2.16: Regeneration study for a Panamax-sized wind-powered ship. Operating points show the propeller P/D ratio (from 0.6 to 1.4) [73].

---

[1]Update, March 2024: Foundation[0] has released two papers on the design of propellers for integrated regeneration capabilities [74], [75]. These papers were originally published by MARIN, and conclude on 250kW regeneration at 16kn for the 69m long sailing yacht 'ZERO'. The largest challenge appears to be the trade-off between regeneration efficiency, hull pressure fluctuations, and propeller cavitation.

[2]Update, March 2024: In the last year, two M.Sc. thesis projects were conducted at TU Delft, which research regeneration. Van der Plas [76] focused on early design-stage regeneration power prediction for sailing yachts. Van Heugten [77] investigated optimizing propellers for both propulsive and regenerative operation.

2.4. Existing Vessels

(a) Rigid sail configuration on New Aden [78].

(b) E-Ship 1 with tri-rudder configuration [79].

Figure 2.17: Commercial applications of wind-assisted propulsion systems.

There are vessels currently using wind assistance, and companies promoting market-ready retrofit systems. Around two dozen commercial wind-assisted ships are currently in operation [80]. The application is limited to cargo ships, except for a small number of ferries and leisure yachts. Within shipping, most wind-assist systems are retrofitted onto existing ships. As such, potential fuel savings are further limited by the original vessel design not being optimized for balancing side forces. This creates additional limitations, mainly regarding the ship's structural integrity, operability, and stability. These factors are also the primary technical concerns that shipowners express about implementing wind-assisted propulsion [81].

Fuel savings of current implementations are modest, with claimed route-level savings ranging from 5 to 25% [82]. There are commercial implementations of rigid sails, most notably on a 300.000DWT tanker 'New Aden' [83], claiming 10% reductions. Econowind [84] has installed turbosails on two general cargo vessels of 3600DWT and 6500DWT, claiming fuel savings of 10-15% using two sails per ship. Flettner rotors are the most prevalent technlogy. The largest fuel savings of 25% are reported for the 9000DWT Ro-Ro 'SC Connector' [85] and the 10.000DWT cargo ship 'E-Ship 1' [86]. According to the final report for E-Ship 1 [79], the hull and propeller/rudder configuration was optimized for the wind-assisted operation, leading to additional 3% and 5% savings, respectively. Most notably, this resulted in a triple-rudder configuration, from having to deal with a large moment on the ship. The choice of using more than one rudder allows high aspect ratio surfaces while increasing the total area.

The claims on fuel savings should be handled with care, considering the ambiguity in how fuel savings can be defined and measured. However, even when adopting an optimistic stance on the values, none of the existing vessels come close to 50% savings.

2.5. Vessels in Development

Further information can be drawn from currently developed wind-assist concepts. Seeing which designs are adopted in commercial applications gives insight into the feasibility and expected efficiency of particular approaches. It should be noted that there is always uncertainty in the accuracy of the information disclosed for concept designs, which can still be subject to change. An overview of prominent designs is given in Table 2.5.

Table 2.5: Specifications of new vessel concepts using rigid-sail wind-assisted propulsion.

Vessel	Type	L_{pp} [m]	B [m]	B/T [-]	v_s [kn]	Fr [-]	A_{sail} [m^2]	A_{sail}/LT [-]	Savings
Windcoop[a]	Gen. Cargo	70	13	4.3	8	0.16	1460	20	90% +
Canopée[b]	RoRo	118	22	4.4	16	0.24	1452	11.5	15-40%
Neoline[c]	Gen. Cargo	136	24.2	4.4	11	0.15	3000	21.2	80-90%
Silenseas[d]	Cruise Ship	190	25	2.8	12	0.14	4350	21.9	50%
Oceanbird[e]	RoRo	200	40	4.4	9-10	0.11	6300*	30.1	90%

[a] [87], [b] [88], [c] [89], [d] [90], [e] [91]
*estimated

The listed ships vary in dimensions, speed, and expected savings. Looking at the main particulars, it can be noted that while the size of the vessels varies considerably, most designs fall very close to each other in terms of beam-to-draft ratio. This parameter strongly influences wind-assisted ships' performance, marking the tradeoff between stability and efficient side force production. Apart from Silenseas, all ships are wider than conventional design guidelines suggest. Watson [92] finds an average B/T of 2.2-2.5 for merchant ships. Most general cargo, tankers, and bulk carriers fall within this range. The design guide by Papanikolaou [32] gives an average B/T of 2.1-2.3 for slow cargo ships. It is stated that both frictional and residuary resistance is generally minimized for a B/T of 2.5. The fact that all cargo ships in this list exceed this design guideline suggests that stability concerns for wind-assisted ships aiming at high fuel savings may be significant. The trade-off between better side force generation and increased stability leans towards the latter. The current Silenseas concept, as the only passenger ship, is the only outlier. Appendix B contains a comparison of the main particulars between the wind-assisted concepts and the conventional fleet.

All ships sail at relatively low speeds, with Froude numbers between 0.11 and 0.16. The exception here is Canopée, which sails faster than the other vessels. This is reflected in the proposed fuel savings, which are also much lower. It is difficult to evaluate the sail area with respect to the savings because of the dependencies on resistance and speed. However, it is possible to evaluate the sail area with respect to the hydrodynamic surface area. Neglecting the effect of additional appendages, it can be inferred that it will be more challenging to balance side forces when the chord-span area of the aero-surfaces (i.e. the sails) is much higher than the chord-span area of the hydro-surfaces (i.e. the hull). This ratio appears relatively similar for most concepts, with factors around 20. Canopée has a much lower factor, which can be explained by the lower fuel savings and overall lower sailing thrust component. Oceanbird appears most ambitious, with significant side force having to be balanced by the hull.

More details on the hull form, including appendages, are disclosed for some of the concepts. These are illustrated in Figure 2.18. The most recent Windcoop design features a 2.5m deep center keel and a large high aspect ratio spade rudder. The ship aims for the highest relative amount of wind propulsion, only aiming to use engine power in unfavorable wind conditions. From that perspective, it makes sense that a fixed keel, similar to the one of a sailboat, is implemented. A previous render of Windcoop, shown in 2.18b, shows a single-shaft, twin-rudder configuration. These rudders are not downstream of the propulsor but on either side, similar to a twin-rudder sailing yacht configuration. The line of reasoning for this configuration might be that the ship is expected not to use its propeller most of the time, so the placement with respect to the propulsor is not as relevant. Having twin rudders increases the aspect ratio, leading to a more efficient side force and moment generation.

Canopée is the only vessel in the list already in construction, leading to higher fidelity of the available design data. An earlier render of the vessel showed a high-aspect-ratio fin close to the ship's bow. Considering draft restrictions, it is conceivable that the fin uses a retractable mechanism. This can be compared to Neolines' 8.5m deep retractable high aspect ratio center keel.

Oceanbird uses controllable fins. Furthermore, skeg-like gondolas are employed in front of both propellers. These skegs fully extend the draft of the aft sections to the maximum draft at midships. Information is given on the heel constraint; it is stated that the ship uses a ballast system for active heel compensation. However, it is also mentioned that even without compensation, Oceanbird would not heel more than 5° when fully powered in beam winds.

(a) Windcoop, recent version [87].

(b) Windcoop, older version [93].

(c) Canopée [94].

(d) Neoline [89].

(e) Oceanbird [91].
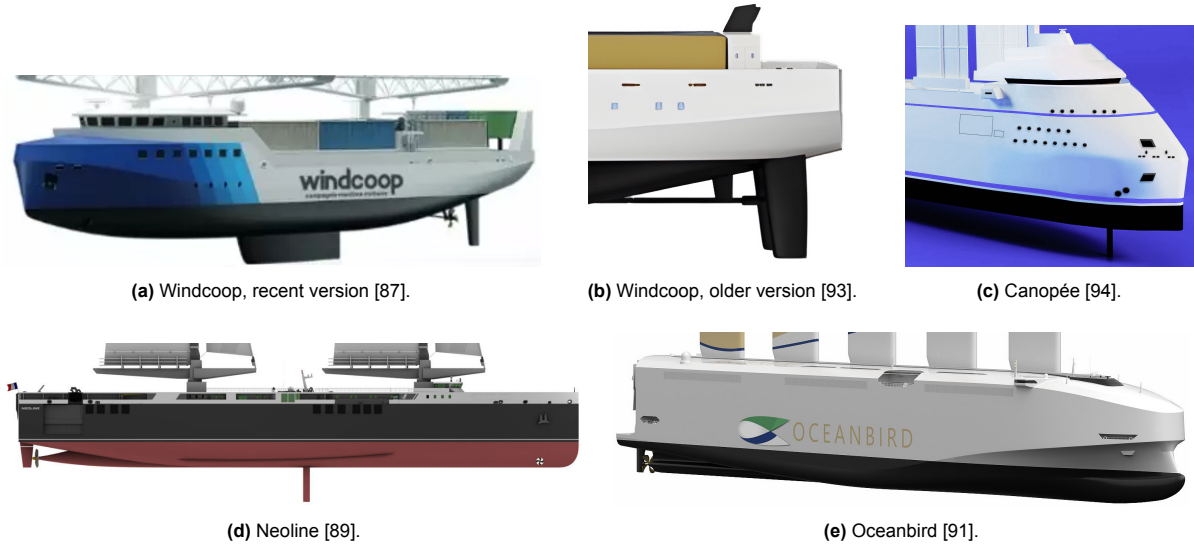
Figure 2.18: Overview of different underwater design features found in concept designs.

3

Methodology

3.1. Workflow Overview
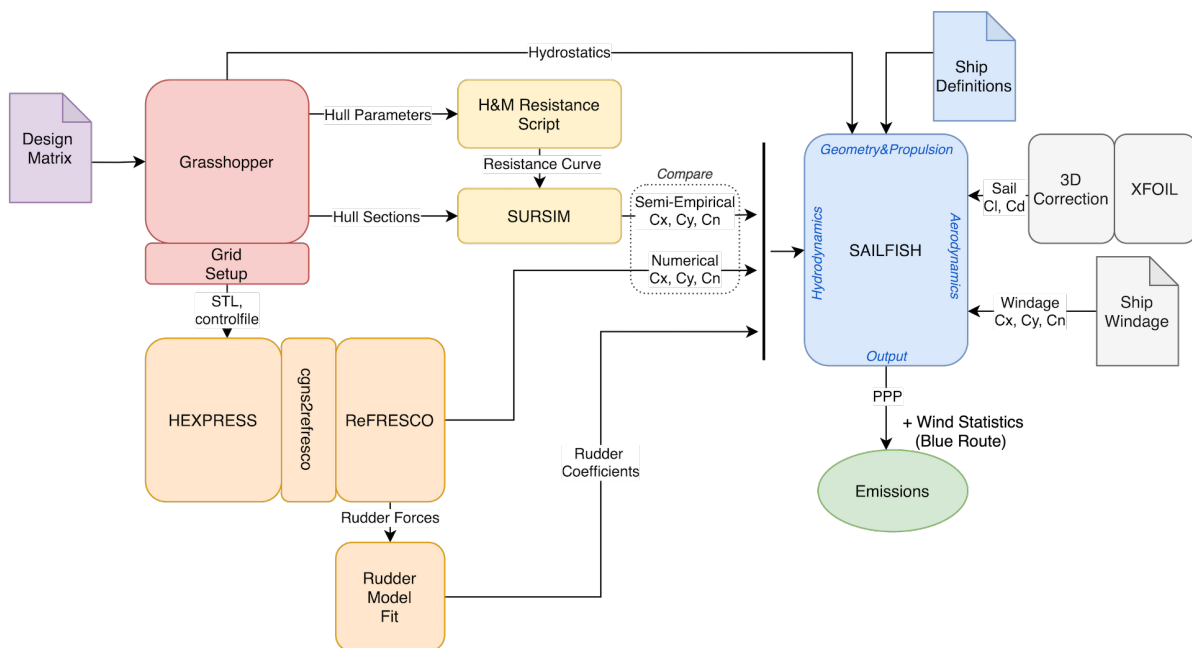
Figure 3.1: Methodology for estimating fuel-savings based on ship design parameters, focusing on the hydrodynamic aspects.

As part of the integrated approach, various aspects of the operation of the wind-assisted ship have to be modeled. Following the flowchart shown in Figure 3.1, a design matrix (diagram: purple) is the input for the construction of a variety of ship geometries (diagram: red). These geometries are used in either the semi-empirical method (diagram: yellow) or for the numerical CFD computation (diagram: orange).

Both approaches compute the resistance and the forces on the hull under drift. This results in a table of coefficients C_X, C_Y, and C_N, as a function of the drift angle. Since both approaches yield the same coefficients, a valuable comparison between the two tools is possible. The only distinction is that the numerical method also allows for a more accurate description of the forces and interactions of high-aspect ratio appendages, such as rudders or anti-drift fins.

Sailfish (diagram: blue) then uses either the semi-empirical or numerical dataset. It solves the steady equilibrium condition of the ship for each defined wind condition, considering hydrodynamic, aerodynamic, operational, and propulsive definitions.

The aerodynamic system (diagram: grey) can be split into the contribution of the sails, calculated using XFOIL, and the contribution of the ship's windage.

Finally, a Power Prediction Program (PPP) can be constructed, containing the ships' emissions for a range of wind speeds and directions. Multiplying the PPP matrix with a corresponding matrix of wind statistics estimates the total operational emissions of a ship design (diagram: green). The relative fuel savings can then be determined using a reference calculation without wind propulsion.

The following sections describe the workings of each of these components in detail.

3.2. Design Matrix

Design matrices were defined to denote the parameter variations that are investigated in this study. Based on the research goals, three computational batches were defined:

Table 3.1: Design Matrices for Computation Batches.

BATCH 1 - Ship Variations

Parameters	Value List	Unit
Beam-to-Draft Ratio	[2, 2.8, 3.6, 4.4]	[-]
Hull Deadrise Angle	[0, 5, 10, 15]	[deg]
Skeg Variant	[None, Short, Long]	[-]
Drift Angle	[0, 2.5, 5, 7.5, 10]	[deg]

BATCH 2 - Rudder Investigation

Parameters	Value List	Unit
Beam-to-Draft Ratio	[2, 2.8, 4.4]	[-]
Hull Deadrise Angle	[0]	[deg]
Skeg Variant	[None, Long]	[-]
Drift Angle	[0, 6]	[deg]
Rudder Angle	[0, 3, 6, 9, 12]	[deg]

BATCH 3 - Anti-drift Fin

Parameters	Value List	Unit
Beam-to-Draft Ratio	[2.8]	[-]
Hull Deadrise Angle	[0]	[deg]
Fin Area	[20, 35, 50]	[m^2]
Fin Position (station)	[10, 18]	[-]
Fin Angle	[0, 6, 12]	[deg]

Batch 1 aims to investigate how the hull design can be optimized for wind-assisted propulsion. The literature review identified three promising ways to increase the side force generation. A lower B/T ratio increases the side force generation but makes the ship more slender, lowering its roll stability. A deadrise angle, or the addition of a skeg, may increase the side force generation but may also result in higher resistance.

All 48 variations were investigated at five drift angles, from 0° to 10°, at the fixed operational speed of 12 knots, leading to a total of 240 computations.

Batch 2 looks at the rudder performance of six designs in more detail. A rudder sweep was conducted, in which the rudder angle was altered from 0° to 12°, both without and with a drift angle of 6°. To avoid an overly inflated number of computations, the design variations were limited to three B/T ratios, only one skeg variation, and no deadrise variation.

In total, this results in 60 additional computations, also computed at the fixed operational speed of 12 knots.

Batch 3 considers the introduction of a fin as an additional high-performance appendage. The ship design remains constant, while six fin configurations varying in position and size of the fin (under constant aspect ratio) were added to the hull. A version of the fin as an active appendage, being able to change angle-of-attack just like a rudder, was also investigated. To limit excessive calculation numbers, only the angle of the fin was varied, instead of both fin and drift angles. Using a rudder model [95], the results can still be interpolated to account for both drift and fin angle variations.

With these considerations, 18 further computations make the analysis of the anti-drift fin possible.

3.3. Geometrical Preparation

A parametric model of the ship geometry was created in Grasshopper, a visual programming language embedded in Rhino that allows for scriptable parametric design variation. Based on up to 10 design variables, this model constructs the ship geometry, positions appendages, and adapts dimensions for constant displacement. Then, it exports all files necessary for the CFD grid generation and the calculation in SURSIM, along with additional geometric and hydrostatic information.

The parent hull form is the MARIN Ferry, which provides an excellent reference since it has similar main particulars to the Silenseas cruise ship, as shown in Table 3.2. The main particulars of the ship are adjusted to match those of Silenseas. The geometry is shown in Figure 3.2. More extensive design data of the reference MARIN Ferry is shown in Appendix C.

Table 3.2: Comparison of main particulars of the MARIN Ferry and Silenseas vessels.

Parameter	Description	MARIN Ferry	Silenseas
LOS	Length Overall Sub.	201	190m
B	Beam	30	25m
TA	Draft, aft	7m	9m
TF	Draft, forward	7m	9m
DISM	Displacement Mass	25112t	23000t

Table 3.3: Appendage sizes and aspect ratios.

Appendage	Proj. Area	AR
Rudder	20.7m^2	1.5
Short Skeg	189m^2	≈ 0.06
Long Skeg	293m^2	≈ 0.06
Fin	20-50m^2	3

(a) Hull lines and sectional area distribution of the MARIN Ferry.

(b) Model of the ferry with superstructure and skeg.
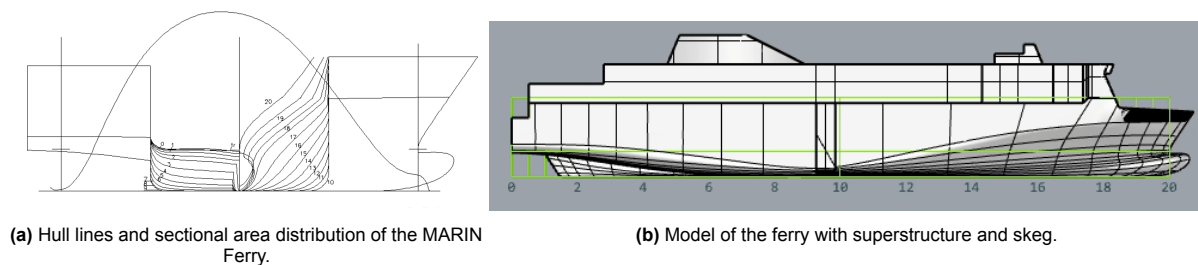
Figure 3.2: Geometry of the MARIN Ferry reference model.
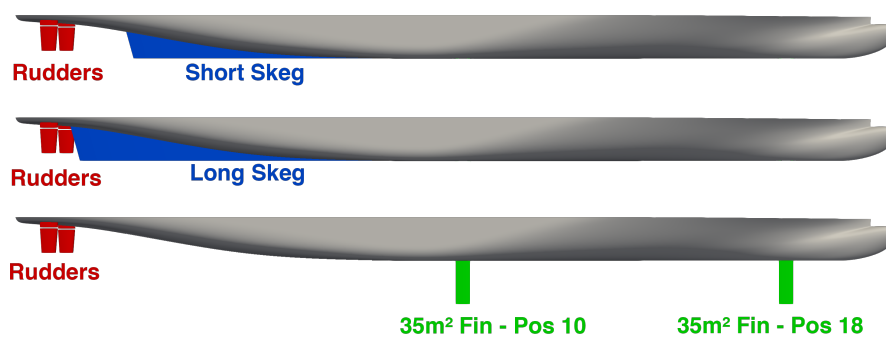
Figure 3.3: Layout of the various investigated appendage geometries.

Altering the B/T ratio was achieved through relative scaling of the beam and draft. For the deadrise, the hull curves were modified to accommodate a 15° deadrise angle. In Grasshopper, interpolating the surface control points between the 0° and 15° deadrise geometry gives the intermediate cases.

The skeg geometries are based on the outline of the skegs from a study by Ferrari et al. [54]. These were adapted to be optimal for mesh generation; rounded edges along the bottom of the skeg were flattened into straight edges to avoid acute angles, which would lead to very non-orthogonal cells in the gridding process. For the same reason, the trailing edge was flattened to feature a thin, flat surface instead of a sharp edge.

The rudder and rudder headbox were modeled based on the schematics of the MARIN Ferry. Similar to the skeg, it was made sure that there were no sharp angles or corner radii. The rudder shaft exposed in the gap between the rudder and rudder headbox was omitted to reduce the complexity of the model, given its very minor force contribution.

The fin was modeled using a NACA0009 foil section, which has the ideal thickness (9% of the chord length) for maximum efficiency at the operational Reynolds number ($Re = 2e7$). Using a NACA foil shape [96] allows for easily reproducible results since it is a very common and standardized design. The cross-sectional shape was extruded to the desired length to form the final fin.

A fair comparison between the design variations is essential. To ensure this, the displacement of the ship was kept constant across all designs. Generally, it would be enough to adjust the draft of the ship to rectify the differences in displacement. In this case, this would lead to poor results, as changing the draft would, in turn, alter the beam-to-draft ratio, which is another fixed design parameter. Because of this, an iterative approach was used, where both beam and draft are altered proportionally until the displacement reached a tolerance of 0.25%. This was possible by using the Anemone plugin, which allows for for and while loops across grasshopper components.

3.4. Semi-Empirical Method for Hydrodynamics

Two empirical tools are needed to determine the required hydrodynamic data equivalent to the CFD output: one for estimating resistance and one for calculating forces and moments under drift.

In Section 2.2.2, DESP, a tool based on the Holtrop and Mennen approach [39], was introduced. This method allows for estimating the ship resistance at various speeds based on geometrical coefficients. The DESP tool itself is not used for this research due to licensing restrictions. Instead, a complete custom implementation of the same Holtrop and Mennen method was written in Matlab. This allows for a more streamlined workflow and a higher degree of customization. The code was validated against the open-access ShipLab application from NTNU [97].

Table 3.4 shows the required input data for the resistance analysis. All data is extracted from Grasshopper and added to a .csv table for each design. In a `holtropPrePro()` step, these input parameters are used to calculate a further 32 coefficients. These are then used in a `holtropSolve()` function, which gives the ship resistance (and contributions) for several ship speeds.

Table 3.4: Resistance Estimation Input Ship Data.

Parameter	Description	Unit
LWL	Waterline Length	[m]
B	Beam	[m]
TA	Draft, aft	[m]
TF	Draft, forward	[m]
CB	Block Coefficient	[-]
CSM	Midship Section Coefficient	[-]
CWL	Waterline Coefficient	[-]
LCB	Longitudinal Center of Buoyancy	[-]
cstern	Stern type (Gondola, V-Shape, Normal, U-Shape)	[string]
bow	Bulbous Bow	[bool]
tr	Submerged Transom	[bool]
app	Appendage Resistance Factor	[-] (list)
app_area	Appendage Area	[m^2] (list)

Next, SURSIM was used to estimate the hydrodynamic forces under drift. The theory behind the tool is described in Section 2.2.3 'SURSIM'. Next to the resistance curve, SURSIM bases its calculation on ship sections. The ship was divided into around 90 sections, which is just below the limit of the maximum number of sections that SURSIM supports. More sections were dedicated to the aft and bow regions, since the changes in geometry are more pronounced there.
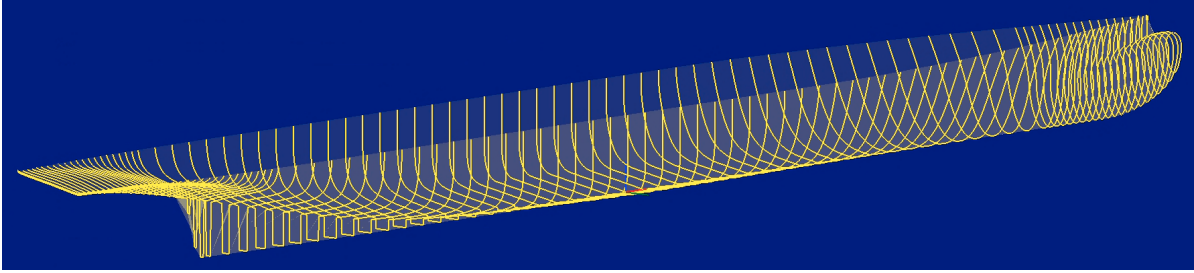
Figure 3.4: Example of the section curves used as input for SURSIM.

SURSIM then performs a sweep of drift angles and outputs the total forces and moments on the hull. From there, the same post-processing as for the forces computed through CFD was applied, described later in Section 3.6 'Post-Processing of Hydrodynamic Data'.

3.5. Numerical Method for Hydrodynamics

3.5.1. Grid Setup

The grid generation step is prepared in Grasshopper, which outputs an STL file containing the boundary surfaces of the simulation domain, and a control file to define the grid settings. These files are then read by HEXPRESS, which generates a 3D anisotropic hexahedral mesh. The goal of the grid setup is to achieve a sufficiently sized domain and refined grid to achieve a mesh-independent result while not reaching an excessively high cell count, which would lead to large computational times.

A rectangular domain with a width and length of 10*LPP and a height of 5*LPP was used to avoid wall interaction effects and represent deep water conditions. A closed domain is achieved by intersecting the underwater ship geometry with the top surface of the domain box. HEXPRESS supports refinement levels in integer steps, with each refinement level subdividing each cell into eight new cells.

The starting point for the refinement step is defining the initial cell size (ICS), set to 7 cells per LPP. From this, the base refinement is then calculated according to:

$$R_0 = \text{round}\left(\log_2\left(\frac{N_b \cdot ICS}{B}\right)\right) \approx 6 \tag{3.1}$$

N_b was set to 55 in this equation, based on common practices at MARIN. This means 55 cells per ship beam are strived for. Since the beam in this equation varies between different designs, the base refinement could also vary. However, values range only from around 5.9 to 6.1, so the base refinement was set to 6 for all grids.

A number of refinements are defined to inform the cell size for various components. Table 3.5 gives an overview of the refinement levels. Surface refinements are only applied to the boundary, while box refinements are applied to an entire volume.

For the skeg, each surface was attributed a different refinement based on its relation with the flow, and geometrical size. Instead of listing each surface, the range of refinements is given here.

Finding the correct refinement level for each component is an iterative process. Setting the refinement levels, generating the grid, and evaluating it using grid statistics and visual inspection (especially in critical regions with large curvatures) gives insight into how well the grid adapts to the geometry. The process and associated guidelines used are in line with the method MARIN applies to similar projects.

3.5.2. Grid Generation

The grid generation in HEXPRESS consists of five steps. The first step fills the domain with cartesian (prismatic) cells according to the initial cell size. After that, the mesh is adapted, using the refinement levels set for various surfaces and volumes within the mesh. Cells intersecting the geometry are re-moved and the individual cells are subdivided anisotropically to match the curvature of the geometry.

Table 3.5: Refinement levels for various components.

Component	Region	Refinement Type	Refinement Level
Hull	Midship	Surface	6
Hull	Aftship	Surface	8
Hull	Foreship	Surface	8
Hull	Bow	Surface	8
Hull	-	Box	6
Transom	-	Surface	9
Rudder/Rudder Headbox/Keel	Leading Edge	Surface	10
Rudder/Rudder Headbox/Keel	Mid Section	Surface	8
Rudder/Rudder Headbox/Keel	Trailing Edge	Surface	11
Rudder/Rudder Headbox/Keel	Horizontal Plane	Surface	10
Rudder/Rudder Headbox	Gap	Box	10
Keel	-	Box	9
Skeg	Front Section	Surface	8-11
Skeg	Mid Section	Surface	7-8
Skeg	Aft Section	Surface	8-10

In the snapping step, the mesh is projected onto the surfaces, points are moved to intersection points, smoothing is applied, and additional cells may be inserted. Possible negative, concave, twisted, or relaxed cells are removed during optimization, and the mesh quality is improved. The target set in the optimization is a minimum cell orthogonality of 30°. This metric will be further discussed in the next section.

The last step in the grid generation is the insertion of the viscous layer. This is a crucial step, as it determines how the modeling in the near-wall regions is dealt with. The different approaches are explained in detail in Section 2.2.4 'ReFRESCO', where the concept of $y+$ and wall functions was presented.

For this study, wall functions were used. As such, the viscous layer insertion targets the first cell center to fall around $y+ = 200$, into the log-law layer.

3.5.3. Grid Properties

The number of cells is a deciding factor for the computational time. The average cell number per grid in the main calculation batch was around 10 million, and the most complex mesh contained 17 million cells. The chosen refinement levels ensure the grid is well resolved, yet fast to compute. The reason why some grids have a higher cell count is either because of having additional appendages, or because of having a large transom, which is another surface with high refinement levels. For this comparative study, it is more important that the grids are similar than that they have an equal cell count.

Metrics to judge the mesh quality help find the right number of grid refinement levels. Cell orthogonality measures how skewed the normal vector of a shared cell side is with respect to the connecting line between two cell centers. Lower orthogonality leads to higher numerical instability and potentially diverging solutions. After the viscous layer insertion, the average minimum orthogonality per grid is 15°, and all grids have a minimum orthogonality above 10°. Before viscous layer insertion, all grids have a minimum orthogonality above 30°. This is in line with the guidelines for comparable computations performed at MARIN.
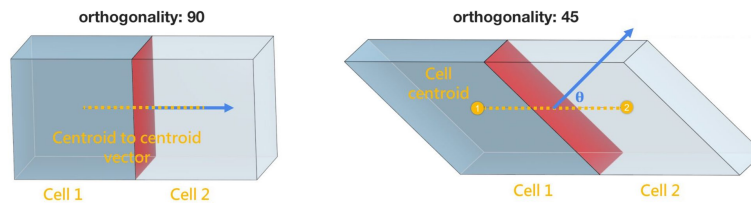
Figure 3.5: Orthogonality between two grid cells [98] (modified).

The adjacent volume ratio is another good quality indicator. It denotes the maximum fraction in volume between a cell and its neighbors. Sudden jumps in cell size should be avoided. For the grids in this study, the maximum adjacent volume ratio never exceeds 20.

Table 3.6 shows the grid statistics for the three calculation batches.

Table 3.6: Grid statistics for the three calculations batches.

BATCH 1 - Ship Variations

Parameter	Average	Min	Max
Number of Cells	10M	4.5M	17M
Min. Orthogonality	15.2°	10.3°	20.3°
Max. Adjacent Volume Ratio	17.2	13.9	19.4

BATCH 2 - Rudder Investigation

Parameter	Average	Min	Max
Number of Cells	9.7M	6.4M	14.3M
Min. Orthogonality	17.4°	15.4°	19.9°
Max. Adjacent Volume Ratio	16.5	13.9	19.1

BATCH 3 - Anti-drift Fin

Parameter	Average	Min	Max
Number of Cells	14.1M	11.7M	16.6M
Min. Orthogonality	12.7°	10.7°	19.8°
Max. Adjacent Volume Ratio	18.1	14.2	19.9

Visualizations for the final generated grids are shown on the next page. Figure 3.6a shows the computational domain and the volume refinement around the entire ship. In Figure 3.6b, the various refinement levels for the ship's mid, fore, and bow sections are visible. Figure 3.6c shows the viscous layer insertion at various stations along the hull. The number of cells roughly doubles in this step. The regions shown in Figures 3.6d and 3.6e have the highest refinement. For example, the trailing edge of the rudder features around eight cells in the transverse direction, ensuring the curvature in this region is accurately resolved. It is visible how the trailing edges and leading edges are more refined and how the grid transitions between the areas.

(a) Grid domain

(b) Bow refinements

(c) Viscous layer insertion

(d) Skeg and rudder refinement

(e) Rudder gap and trailing edge refinements
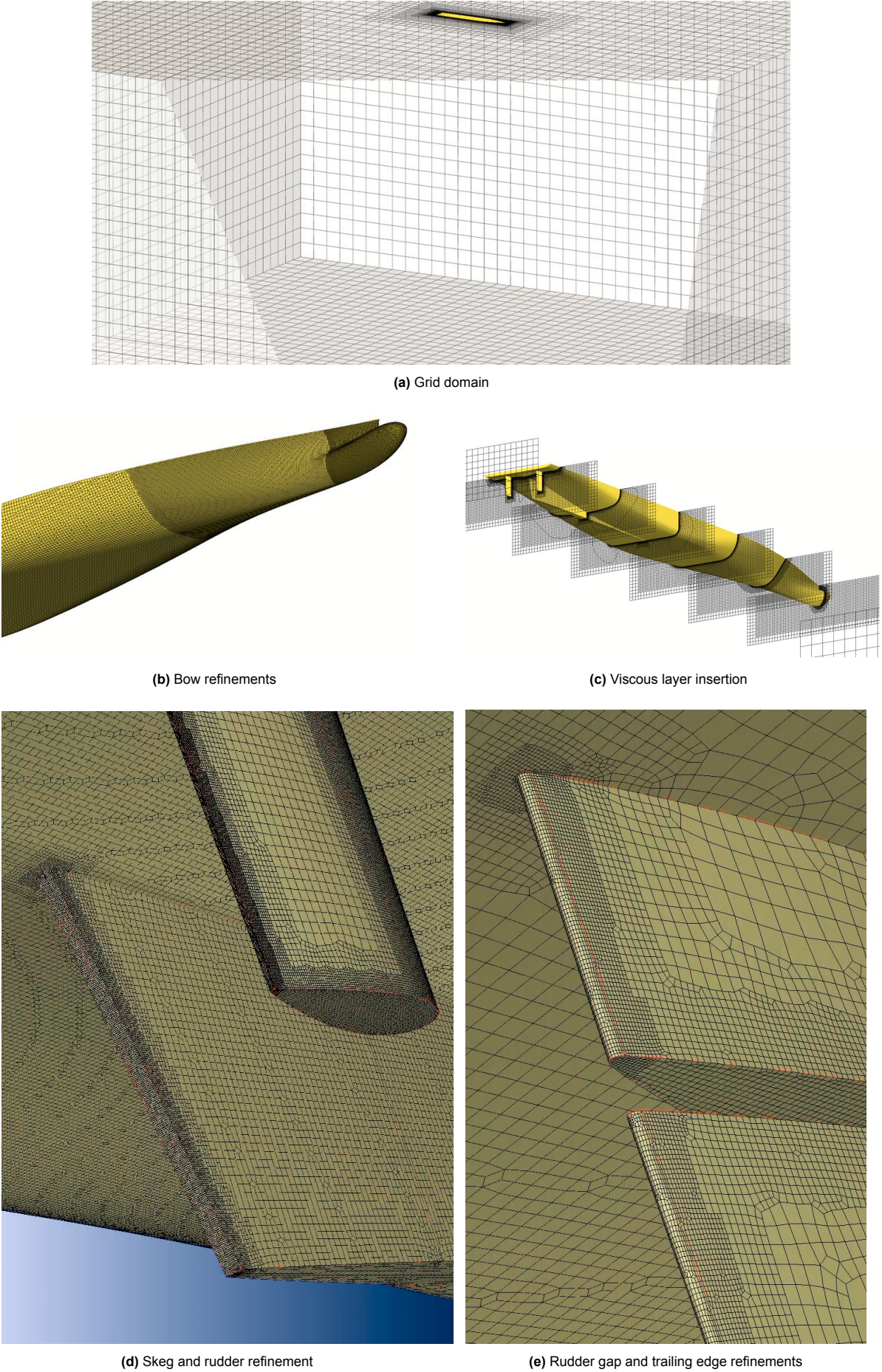
Figure 3.6: HEXPRESS mesh visualizations.

3.5.4. Solver Setup

In this study, RANS double-body simulations are conducted. The theory behind RANS is explained in detail in Section 2.2.4 'ReFRESCO', including information on turbulence modeling, near-wall modeling, and surface treatments. The propeller was not included in the CFD analysis. It will be characterized in Section 3.8.1 'Propulsive System'.

Boundary Conditions
The continuity and momentum Equations 2.37a and 2.37b, forming the RANS method, are applied over a control volume. This volume is the domain shown in Figure 3.6a. Boundary conditions have to be defined on each surface to define the local state of the flow. The mesh is described in a body-fixed reference system, a necessary condition for a steady simulation with an otherwise moving object; as such, the incoming flow is defined equal to the ship speed. To further facilitate the computation, the drift angle of the ship is also applied to the incoming flow, rather than rotating the body, so that the same grid can be used for all drift variations of a specific design.

On five out of six domain boundaries ('starboard', 'portside', 'inlet', 'outlet', 'bottom'), the same boundary conditions are defined through the 'AutoDetect' feature, which identifies whether there is incoming or outgoing flow through the boundary. The bottom of the domain was also included instead of tagging it as a wall. As such, it is not seen as a physical wall but instead simulates an effective infinite water depth. For these surfaces, the velocity condition was set based on a velocity vector:

$$\begin{bmatrix} u \\ v \\ w \end{bmatrix} = \begin{bmatrix} v_s \cos(\beta) \\ v_s \sin(\beta) \\ 0 \end{bmatrix} \tag{3.2}$$

defined as a function of ship speed and drift angle. In a double-body simulation, a pressure boundary condition is also applied to these boundaries, set to a reference pressure of zero. Hydrostatic pressure, a result of the body force of the fluid, does not have to be considered.

Lastly, the turbulence intensity had to be defined. The Eddy viscosity factor accounts for the energy loss through transport and dissipation of turbulence lost when averaging turbulent effects. As such, it is a non-physical parameter, defined together with a turbulence intensity factor I:

$$I = \frac{u_{\text{fluct}}}{\bar{u}} \tag{3.3}$$

The non-dimensional Eddy viscosity was set to 10, and turbulence intensity to 1%, based on ReFRESCO guidelines.

The surfaces of the physical geometry (hull, appendages) receive wall boundary conditions. This includes a no-penetration condition, stating that the velocity normal to the wall has to be zero, and a no-slip condition, stating that the tangential velocity also has to be zero.

The top of the domain is a symmetry plane in a double-body simulation, mirroring the flow on the xy plane. The boundary condition on a symmetry plane is that the velocity gradient at the plane should be zero. This allows for flow along the boundary.

Solver Settings
Three equations - the continuity (pressure) equation, the moment transport equation, and the turbulence equation - have to be solved.

The continuity equation, fundamental for ensuring mass conservation, is solved using the Conjugate Gradient (CG) method. The momentum transport equation and the turbulence equation are solved using the Generalized Minimal Residual (GMRES) solver.

The iteration, relaxation, and tolerance factors used come from the MARIN guideline control setup for calm water double-body simulations. The only factor adapted specifically for these computations is the eccentricity correction. This correction uses derivatives to compute values on the wall based on close-by face centers, instead of just taking over the value from the closest face center. The factor for the near-wall face interpolation was lowered from 5.0 to 1.0. A higher interpolation factor is more accurate, but less robust around high aspect ratio cells. Convergence behavior was greatly improved by lowering this value.

3.5.5. Convergence and Residuals

The solver's success can be quantified by looking at the convergence of the results and the associated residuals. The solver reduces the calculation's residual error over the course of 5000 iterations. After that, the computation is terminated. Therefore, it is very important to check the residual error, as the completion of the calculation itself does not indicate correct results. As a matter of fact, as long as the calculation does not diverge, there will always be some output.

The residual error is expressed as the L_2 and L_∞ norm and calculated for each velocity component, pressure, and turbulent kinetic energy and frequency. The L_2 norm is the root mean square of all cell residuals, while the L_∞ norm is the maximum residual.
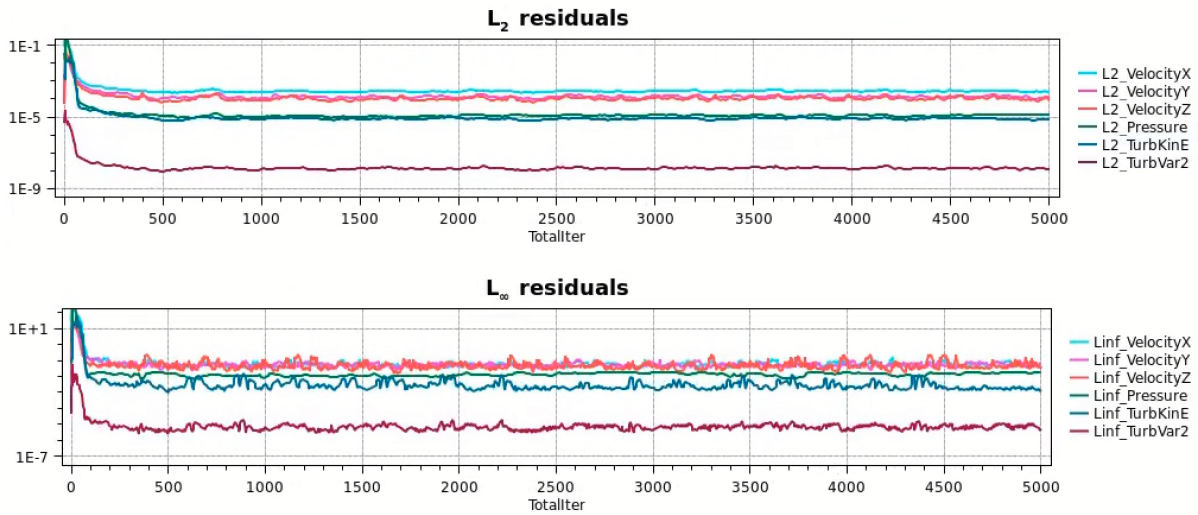
(a) L_2 and L_∞ Residuals for β=0°.
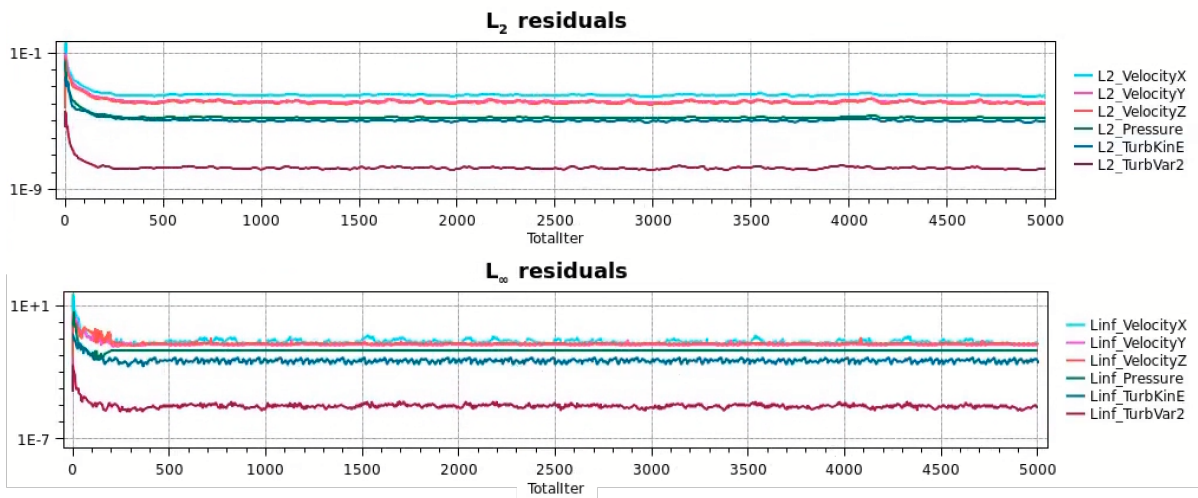
(b) L_2 and L_∞ Residuals for β=10°.

Figure 3.7: Residuals for Ship #22, at two drift angles.
(B/T: 2.8, Deadrise: 5deg, Skeg: Long)

Residuals were found to be very similar between designs, so Figure 3.7 shows the evolution of the convergence for a typical case at 0° drift, and the maximum drift of 10°. It can be seen that the residuals stabilize within the first 500-1000 iterations.

The L_2 and L_∞ norm do not vary significantly with the drift angle. At both 0° and 10° of drift, L_2 pressure residuals are of the order 1e-5, and velocity residuals of the order 1e-4. The L_∞ norm is around 1e-1 for the velocity and around 1e-2 for the pressure. The turbulent kinetic energy behaves similarly to the

pressure, and the turbulence frequency has a much lower residual than the other variables. The L_2 norm is around three orders lower than the L_∞ norm. This means that the high residuals are in specific regions only.

It is important to know where in the domain the high residuals are. This may reveal areas of insufficient grid quality, or regions with challenging flow characteristics. In Figure 3.8, the pressure residuals for the same ship are visualized. Only the pressure residuals are shown, as velocity and turbulence residuals show critical cells in the same regions.

The cells with high residuals are located at regions with drastic changes in geometry, such as the transom or the leading edge of the skeg. There, it is challenging to define the flow as it wraps around a sharp edge and likely separates. High residuals are also visible in other reversed flow regions, such as the bulbous bow and around the rudder. Overall, the regions where high residuals remain are regions with very unsteady flow conditions. The calculations in this study are steady, and as such do not take into account time fluctuations. As such, they represent inherent limitations of the method and are not indicators of poor mesh quality or erroneous solver settings.

(a) High-pressure residuals.

(b) Cells with a pressure residual above 1e-4.
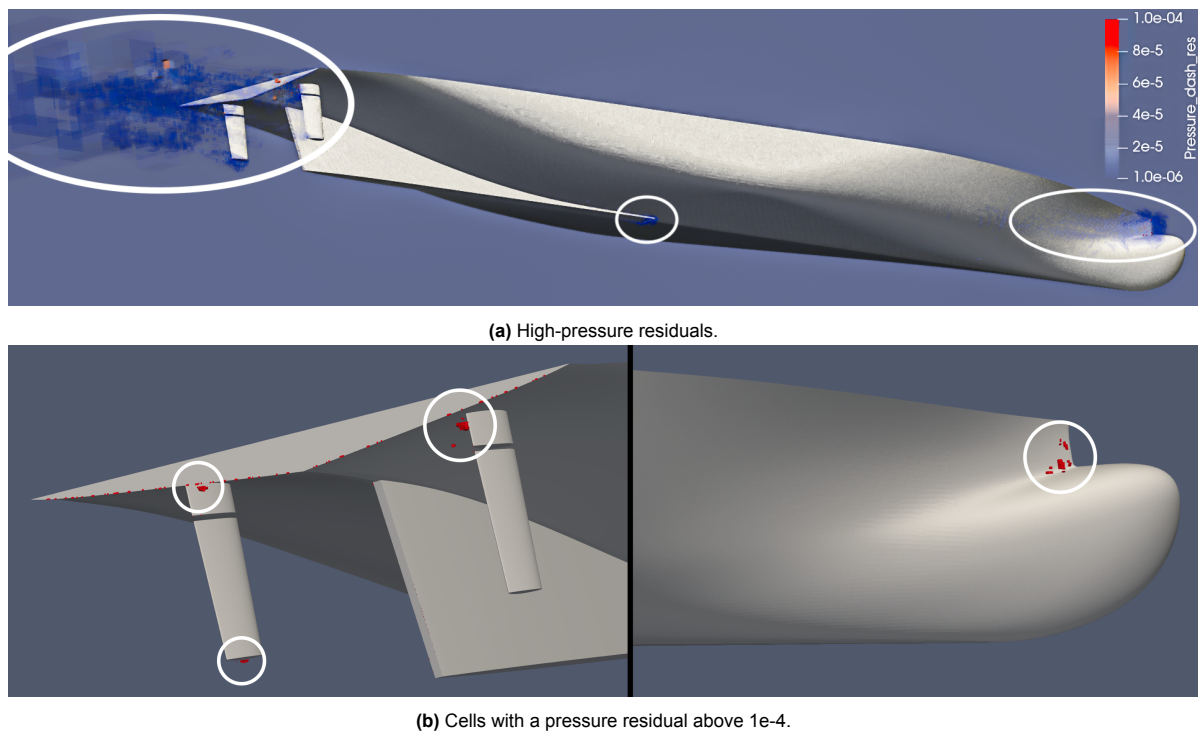
Figure 3.8: Pressure Residuals for Ship #22, at 5 degrees of drift.
(B/T: 2.8, Deadrise: 5deg, Skeg: Long)
The view is oriented to show the leeward side of the ship.

Still, fluctuations remain. Looking at the evolution of the CFD results can give even better insight into the source of these deviations. Figure 3.9 shows the fluctuations in the side force prediction. Most of the fluctuations result from the transom, with the contributions by the rudder, and especially the hull, being much lower. Thus, the residuals are mainly due to the reverse flow of the submerged transom. It should be noted that while the variance in the result looks drastic, it is not that impactful. First, the final result is an average of the last iterations instead of just the final value, as explained in the next section. Also, the transom only makes up a small fraction of the total forces on the hull.
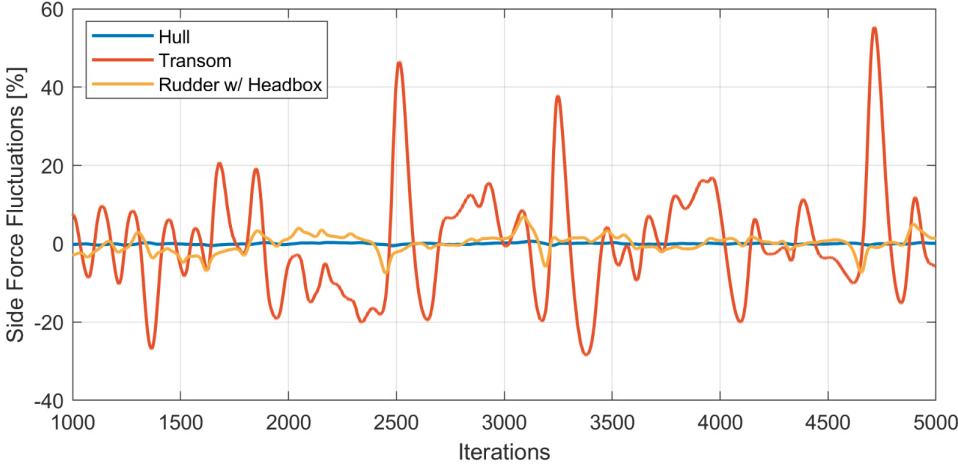
Figure 3.9: Fluctuations in F_y for Ship #22, at 5 degrees of drift.
(B/T: 2.8, Deadrise: 5deg, Skeg: Long)

Another aspect to check in order to confirm a correct solver process are the $y+$ values. As explained in Section 2.2.4 'ReFRESCO', $y+$ denotes the dimensionless distance from the boundary wall. The grid was set up in a way that allowed the first cell layer to fall into the logarithmic boundary layer, at a $y+$ of around 200. Figure 3.10 shows the $y+$ distribution for one of the simulations. The $y+$ is in the correct range, showing that the viscous layer was inserted and computed correctly.
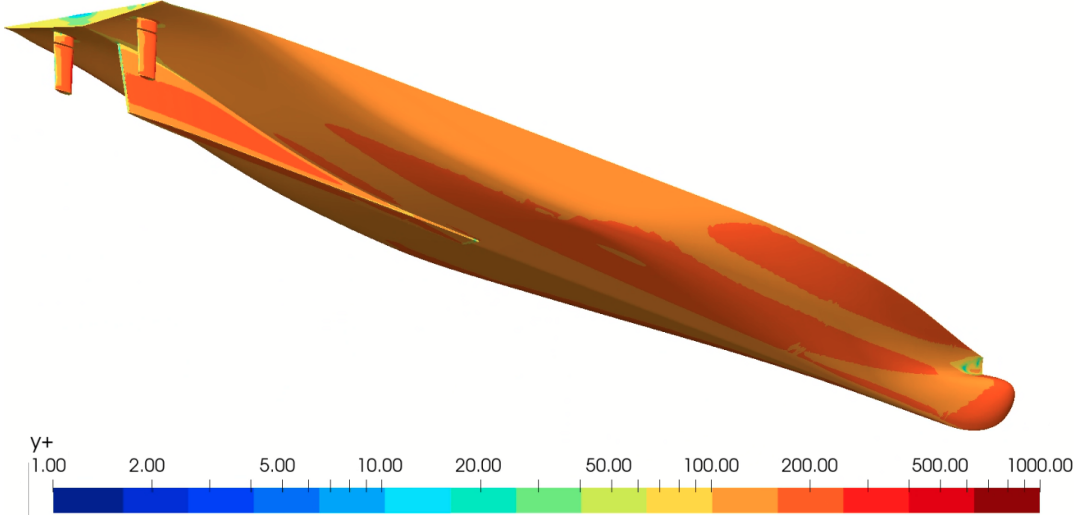
Figure 3.10: Surface $y+$ for Ship #22, at 5 degrees of drift.
(B/T: 2.8, Deadrise: 5deg, Skeg: Long)

3.6. Post-Processing of Hydrodynamic Data

ReFRESCO outputs a CFD General Notation System (CGNS) file. It contains all parameters and variables from the computation. To speed up the post-processing, during the calculation, some variables are already stored through the setup of monitors. These monitors track and save a variable throughout the iterations. The following surface monitors were set up to track the total forces (F_x, F_y, F_z) and moments (M_x, M_y, M_z) per component:

- Hull
- Transom
- Skeg
- Rudder Headboxes
- Rudders

- Rudder PS *(Batch 2 only)*
- Rudder SB *(Batch 2 only)*
- Anti-drift Fin *(Batch 3 only)*

For the rudder investigation, two additional line monitors were set up 0.25 chord lengths ahead of each rudder to measure the effective rudder inflow angle φ_{eff}.

Instead of just taking the results from the last (5000th) iteration, the values for the last 2000 iterations were averaged. This way, fluctuations of residual errors are averaged out. The exact number of iterations to average over (taking the last 4000 as opposed to the last 500) did not have any notable effect on the result.

3.6.1. Hull

Determining the hydrodynamic coefficients is necessary for further use of the hydrodynamic results in the power prediction program (PPP) in Sailfish. They are the following:

$$R = X(\beta = 0) \tag{3.4a}$$

$$C_x(\beta) = \frac{X(\beta) - X(\beta = 0)}{\frac{1}{2}\rho T L v_s^2} \tag{3.4b}$$

$$C_y(\beta) = \frac{Y(\beta)}{\frac{1}{2}\rho T L v_s^2} \tag{3.4c}$$

$$C_n(\beta) = \frac{N(\beta)}{\frac{1}{2}\rho T L^2 v_s^2} \tag{3.4d}$$

The input forces and moments are the sum of all the ship components, including appendages such as skegs and rudders.

While these equations are all that is necessary for the next computational steps, the quality of the analysis and comparison of the results can be greatly enhanced by computing further coefficients. This includes computing the center of lateral resistance, as defined in Section 2.1.5 'Sailing Balance':

$$CLR = \frac{N}{Y} \tag{3.5}$$

Furthermore, going from a body-fixed to a flow-fixed reference frame allows for better analysis of the force components. Lift and drag coefficients can be defined for this:

$$C_L = -C_y \cos\beta + C_x \sin\beta \tag{3.6a}$$

$$C_D = -C_y \sin\beta - C_x \cos\beta \tag{3.6b}$$

In Section 2.1.2 'Forces on a Foil in 3D', a theoretical model for the lift and drag, decomposed into linear, induced (for drag), and non-linear components, was presented. Since this model is based on widely used parameters, fitting to such a model can provide further insight into the origin and characteristics of the different forces and their mechanisms. The chosen scaling functions with respect to the drift angle are the ones developed at MARIN [53], which are optimized for the low drift angles encountered

in sailing (as opposed to e.g. maneuvering models, which deal with much larger angles):

$$C_L = \overbrace{0.5\pi AR \sin\beta \cos^2\beta}^{C_{L,\text{lin}}} + \overbrace{CD_{90} \sin^2\beta \cos\beta}^{C_{L,\text{non-lin}}} \tag{3.7a}$$

$$C_D = C_{D0} + \underbrace{\frac{C_{L,\text{lin}}^2}{e\pi AR}}_{C_{Di}} + \underbrace{CD_{90} \sin^3\beta}_{C_{D,\text{non-lin}}} \tag{3.7b}$$

The two equations are dependent and contain four fitting parameters (AR, CD_{90}, $C_{D,0}$, and e). To solve this optimization problem, the `fmincon` solver [99] from the Matlab Optimization Toolbox was used, as it is suited for constrained multivariate optimization problems. Since there are two equations to optimize, an error function was defined:

$$\text{error} = \sum(C_{L,\text{data}} - C_L)^2 + \sum(C_{D,\text{data}} - C_D)^2 \tag{3.8}$$

It was chosen not to normalize the lift and drag coefficients so that the magnitude of the forces is respected during the fitting process. This is possible because both C_x and C_y coefficients are non-dimensionalized with the same factor.

From the fitting parameters, two further constants can be derived: the effective aspect ratio and the effective draft [34]:

$$AR_{\text{eff}} = AR \cdot e \tag{3.9a}$$
$$T_e = \sqrt{0.5 A_W AR_{\text{eff}}} \tag{3.9b}$$

3.6.2. Rudder and Anti-drift Fin

Like for the hull, a theoretical model can also be used for the rudders and fins to determine parameters that describe their forces, based again on the formulation for lift and drag coefficients. At MARIN, the Rudder 2020 Model [95] is being developed. It contains 12 coefficients to describe the force characteristics of a rudder. This model provides valuable further insight into the flow, and the resulting coefficients are also necessary for implementing the rudder in Sailfish. The numbering of the coefficients is kept in line with the Rudder 2020 report.

Starting with the inflow angle, which might differ from the angle of the ship due to flow straightening effects, an effective rudder angle is defined:

$$\delta_{\text{eff}} = \delta - \arctan\left(C_3 \frac{\sin\beta}{\cos\beta}\right) \tag{3.10}$$

with C_3 being the flow straightening coefficient, describing the interaction effect of the hull on the rudder.

The effective aspect ratio of the rudder differs from the geometric aspect ratio because of tip and base flow effects, so a correction factor is defined:

$$AR_{\text{eff}} = C_7 AR_g \tag{3.11}$$

The lift of the rudder can then be described by:

$$C_L = [dC_L/d\delta]_{\delta=0} \cos(\delta_{\text{eff}}) \sin(\delta_{\text{eff}}) \tag{3.12}$$

with the lift slope containing coefficients C_8 and C_9 as further correction factors:

$$[dC_L/d\delta]_{\delta=0} = \frac{C_8 \pi AR_{\text{eff}}}{AR_{\text{eff}} + C_9} \tag{3.13}$$

As previously described, the drag coefficient can be divided into a resistance (C_{D0}) and an induced drag (C_{Di}) component. In the rudder model, the resistance is described based on an empirical formulation:

$$C_{D0} = \frac{2 \cdot 0.075 \cdot C_{10}}{(\log_{10} Re - 2)^2} \tag{3.14}$$

and the induced drag by:

$$C_{Di} = \frac{([dC_L/d\delta]_{\delta=0}\sin(\delta_{\text{eff}}))^2}{C_{11}\pi AR_{\text{eff}}} \tag{3.15}$$

Lastly, a coefficient accounts for the effect of the rudder on the hull forces. The pressure distribution around the rudder will also have an effect on the pressure distribution on the hull, defined so that:

$$C_{12} = \frac{Y_{\text{rudder}} + Y_{\text{hull}}}{Y_{\text{rudder}}} \tag{3.16}$$

with the output averaged over multiple rudder angles under zero drift.

An overview of the coefficients is given in the table below:

Table 3.7: Rudder model coefficient description.

Coefficient	Type	Description
C3	Interaction	Hull-Rudder Interaction (Flow Straightening) #1
C5	Interaction	Hull-Rudder Interaction (Flow Straightening) #2
C7	Lift	Effective Aspect Ratio Correction
C8	Lift	Lift Slope Dividend
C9	Lift	Lift Slope Divisor
C10	Drag	Form Drag Coefficient
C11	Drag	Oswalds Efficiency Factor
C12	Interaction	Rudder-Hull Interaction

C_5 is conceptually identical to C_3, and exists in the case of twin rudder configurations, like is the case for the MARIN Ferry, to have distinct coefficients for each rudder. An optimization script was also developed for this model, based again on the `fmincon` solver from the Matlab Optimization Toolbox. The model contains four dependent equations, describing the lift and drag for zero and six degrees of drift, and six fitting parameters. The error function is then:

$$\begin{aligned}
\text{error} = \sum(C_{L,\text{data},0°} - C_{L,0°})^2 + \sum(C_{D,\text{data},0°} - C_{D,0°})^2 \\
+ \sum(C_{L,\text{data},5°} - C_{L,5°})^2 + \sum(C_{D,\text{data},6°} - C_{D,6°})^2
\end{aligned} \tag{3.17}$$

Again, it was chosen not to normalize the lift and drag coefficient so that the magnitude of the forces is respected in the fitting process. Also, the 0° and 6° errors are given equal weight. There is no second result under drift for the anti-drift fins, as the straightening effect is expected to be negligible, so $C_3 \approx 0$.

As suggested by the indexing, some of the rudder coefficients have not yet been mentioned. These are listed in the table below:

Table 3.8: Additional rudder model coefficient description.

Coefficient	Type	Description
C1	Interaction	Wake Fraction Ratio
C2	Interaction	Axial Momentum Correction
C4	Interaction	Hull-Rudder Interaction (Flow Straightening) during turn #1
C6	Interaction	Hull-Rudder Interaction (Flow Straightening) during turn #2
ζ	Interaction	Propeller-Rudder Ratio
CRZ	Interaction	Propeller Swirl Component

Coefficients $C_{4,6}$ are not applicable, as they deal with flow interactions while turning, which does not occur for steady-course sailing conditions. The other coefficients deal with the interaction with the propeller and will be discussed in the context of the propulsion system, in Section 3.8.1 'Propulsive System'.

3.7. Aerodynamic Data

The aerodynamic data is an input for the Sailfish model, which determines all forces above the waterline based on ship and wind speed. The focus of the study lies on the hydrodynamic forces. As such, it is important that the wind forces are in the correct order of magnitude and behave correctly for different wind speeds and angles, but they do not have to come from a complex aerodynamic model.

Two contributions to the aerodynamic forces are identified. The forces generated by the sails and the forces generated by the ships' topside and superstructure, referred to as windage.

3.7.1. Sail Forces

With knowledge of the dimensions of the three Solid Sail rigs used by Silenseas, shown in Table 3.9, the forces generated by the sails can be estimated. First, the forces on a 2D section are computed using XFOIL. The symmetric NACA0012 airfoil section was assumed for the rigid sails. The choice of airfoil was based on reaching the highest lift-to-drag ratio at $Re = 1e7$, which was found to be characteristic of the sail's operating regime. XFOIL was able to calculate lift and drag coefficients until 20°, close to the stall angle. The remaining angles, all the way to 180°, were extrapolated using the Montgomerie method [100].

Next, a 3D correction was applied according to the theory described in Section 2.1.2 'Forces on a Foil in 3D', assuming an elliptical lift distribution on the sails. Interactions between the sails are neglected, so the positioning of the sails is only relevant for the position of the center of effort (CE). The sails were positioned so that the CE lies at midship.

Parameter	Value
Number of Sails	3
Sail Area (each)	1450m^2
Sail Height	81m

Table 3.9: Silenseas Rigid Sail Data.
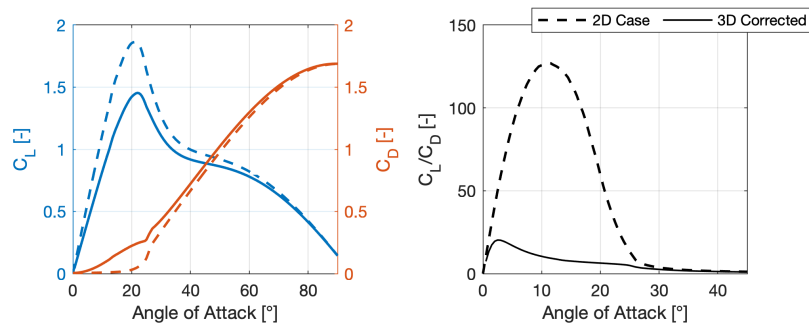
Figure 3.11: Wingsail lift and drag, for the 2D and 3D case.

3.7.2. Wind Forces on the Ship

The wind forces on the ship itself are complex, as the geometry of the hull and superstructure is highly irregular. In the past, windage coefficients have been derived for the MARIN Ferry. They consist of C_x, C_y, and C_n coefficients as a function of the wind angle TWA. This dataset was used in this study. The data is confidential and not presented in this report.

3.8. Operational and Supplementary Data

3.8.1. Propulsive System

The definition of the propulsive system is essential to evaluate the ship's operation in conditions for which sail propulsion alone is not enough to power the ship. The focus of this study is the investigation of variations in hull geometry and appendages, and their relative performance in wind-assisted conditions. Some simplifications in the definition of the propulsion system were necessary to make an efficient analysis possible. A complex propulsive model would also make it harder to pinpoint the source of discrepancies in the operational analysis, should they appear.

The engine was assumed to behave linearly, meaning the emissions are proportional to the engine power, and efficiency factors are constant. The rotation rate of the propeller is uncoupled from the engine rotation rate through a gearbox, which also has a constant efficiency factor attributed to it. Fuel

savings are reported with respect to propulsive fuel consumption, so auxiliary engines for energy needs outside of the powertrain are not considered. The final emissions are given according to the EEDI/E-EXI/CII standards, as grams of CO_2 per tonne-mile [18].

The propeller was defined as a Wageningen C-Series CPP so that performance is not hindered by poor pitch ratios in wind-assisted conditions. Table 3.10 illustrates the relevant input parameters. The values are based on the existing design data for the MARIN Ferry. It is assumed that factors with a geometrical dependency (wake fraction, thrust deduction factor, relative rotative efficiency) are constant throughout the hull variations.

Table 3.10: Propulsive system input parameters.

Engine Parameters

Parameter	Value	Unit
Engine Brake Power	5000	[kW]
Auxiliary Engine Power	0	[kW]
Engine Efficiency	0.705	[-]
Gearbox Efficiency	0.97	[-]
Shaftbearing Efficiency	0.99	[-]
SFC (MDO)	175	[g/kWh]
Density (MDO)	0.855	[t/m^3]
LHV (MDO)	42700	[kJ/kg]
CF (MDO)	3.206	[-]

Propeller Parameters

Parameter	Value	Unit
Propeller Type	CPP	[-]
Propeller Series	C-Series	[-]
Diameter	5.4	[m]
Pitch-Diameter Ratio	1.212	[-]
Number of Blades	4	[-]
Wake Fraction	0.064	[-]
Expanded Area Ratio	0.505	[-]
Thrust Deduction Factor	0.122	[-]
Open Water Efficiency	0.98	[-]
Relative Rotative Efficiency	0.977	[-]
Power Delivery Efficiency	0.705	[-]

Some of the rudder coefficients previously mentioned relate to the propulsive system. Table 3.11 shows the values. C1 describes the ratio of wake fractions between the propeller and rudder. A fraction of 1 indicates that the wake fraction of the rudder is assumed to be equal to that of the propeller. Still, the slipstream contraction behind the propeller might not be fully developed at the rudder position. Therefore, C2 corrects the longitudinal speed component at the rudder's position with respect to the axial-induced velocity of the propeller.

The geometric coefficient ζ is the ratio between propeller diameter and rudder span. The propeller's swirl component is not considered in the rudder definition. Swirl affects the flow velocity on the rudder and may alter its performance. For the MARIN Ferry, a robust description of this effect is neither available nor previously implemented and will therefore be assumed zero, as often done in general [95].

Table 3.11: Rudder model coefficients relating to propulsion system.

Coefficient	Description	Value
C1	Wake Fraction Ratio	1
C2	Axial Momentum Correction	0.56
ζ	Propeller-Rudder Ratio	0.96
CRZ	Propeller Swirl Coefficient	0

3.8.2. Wind Statistics

Defining wind conditions is essential in evaluating wind-assisted ships since fuel savings are linked directly to sufficient wind power availability. For shipping, the Marine Environment Protection Committee (MEPC) of the IMO released guidance for evaluating wind-assisted propulsion methods [101] for the Energy Efficiency Design Index (EEDI). Part of this is releasing a global wind statistics matrix containing weighted wind statistics of the major international shipping routes to quantify fuel savings. The wind statistic matrices contain a probability value for each combination of wind speed and direction. Such guidelines still need to be put in place for passenger ships. As such, three routes were defined

to represent unfavorable, average, and favorable wind statistics relative to the MEPC.1/Circ.896 data. The routes are based on commercially available trips, and the wind statistics were determined using Blue Route [102]. Figure 3.12 illustrates the selected trips.

(a) MSC Opera East Mediterranean itinerary.

(b) MSC Seascape Caribbean itinerary.

(c) Holland America Line North Atlantic itinerary.
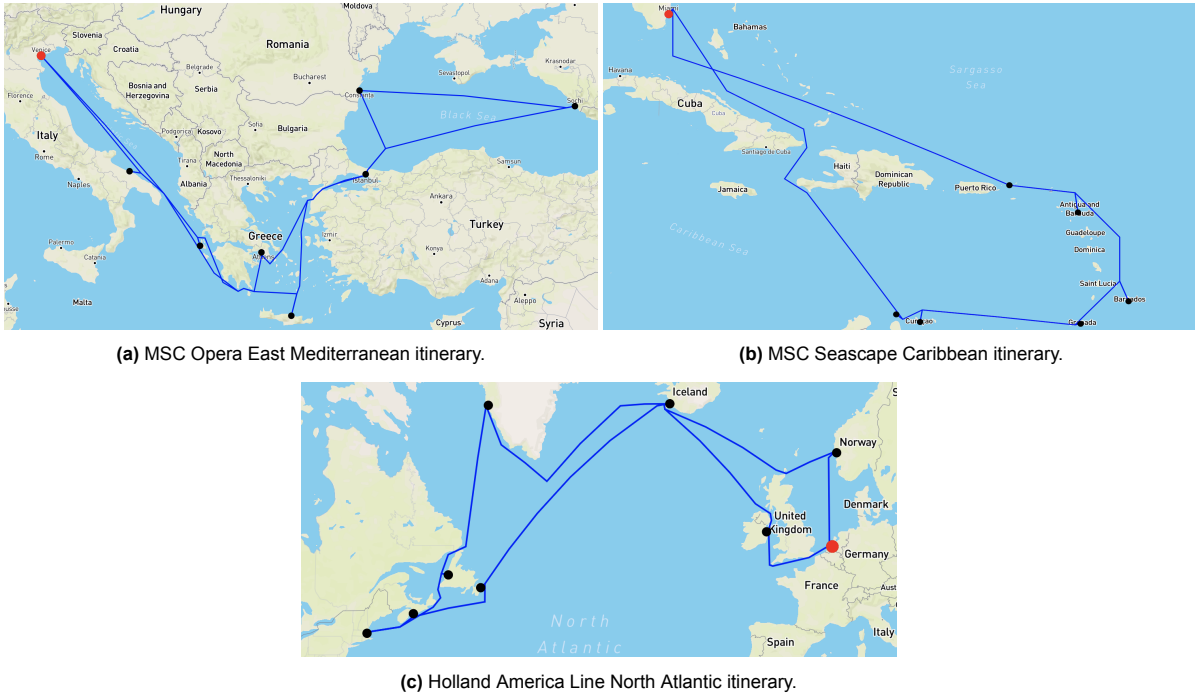
Figure 3.12: Reference cruise ship routes, representative for different wind conditions.

A representative way to quantify wind statistics is using a Weibull distribution, as it has good agreement with real-world wind distributions [103]. It is defined as:

$$P(v) = \frac{\beta}{\eta} \left(\frac{v}{\eta}\right)^{\beta-1} \exp\left[-\left(\frac{v}{\eta}\right)^{\beta}\right] \tag{3.18}$$

The scale parameter η reflects the characteristic wind speed, while the shape parameter β determines the variability. Gusty locations will have a low value (1.5-2) for the shape parameter, while regions with very steady winds will have a high value (3-4). Fitting the Blue Route data to the Weibull model gives the parameters shown in Table 3.12.

The route in the Mediterranean delivers low average wind speeds and very high variability, making it unfavorable for effective sailing. The Caribbean route is comparable to the global average conditions from the MEPC but with a higher consistency due to prevailing trade winds. The North Atlantic route can be considered very favorable. While the variability is lower, the average wind speed is much higher. It should be noted that for this study, the wind statistics matrices are used directly instead of the Weibull parameters. This eliminates the additional errors involved in the fitting procedure.

Route	η [m/s]	β [-]
MEPC.1/Circ.896	7.82	2.29
Mediterranean Route	5.87	1.74
Caribbean Route	7.76	3.06
North Atlantic Route	9.11	2.01

Table 3.12: Weibull parameters for selected wind statistics.
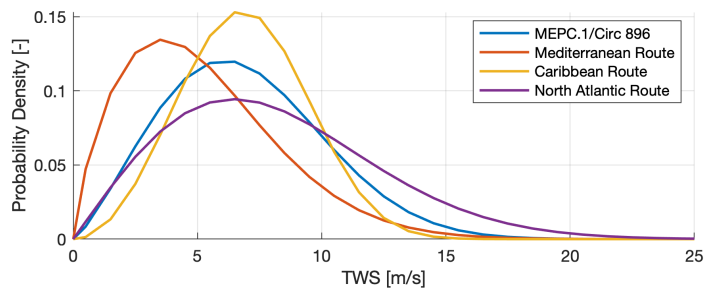
Figure 3.13: Wind probability distributions for different data sets.

3.9. Power Prediction Program

Power prediction programs (PPPs) were used to predict the emissions and the fuel savings of the ship. They were calculated using Sailfish, as described in Section 2.2.5 'Sailfish'.

Sailfish considers the systems shown in the method flowchart in Figure 3.1, including propulsion, hydrodynamic, and aerodynamic data. While all of these aspects have been individually described in this chapter already, Table 3.13 below gives a general overview of the data source to provide maximum clarity on the origin of the final results.

For each design, all the data was parsed into a .yaml file that was then read when executing Sailfish. During execution, equilibrium conditions are calculated for each (72) wind directions and for wind speeds up to 26m/s, considering all the aforementioned systems. From the result, 26x72 matrices were created for all relevant parameters, e.g., force components, ship and rudder angles, sail forces, propeller thrust, and engine emissions.

Table 3.13: Schematic overview of important parameters used for the power prediction in Sailfish.

Systems	Datasets	Variables	Description	Source	Reference
Hydrodyn.	Resistance	$[v_s, R]$	Resistance Curve	Computed	3.6.1
	Maneuvering	$[\beta, Cx, Cy, Cn]$	Forces, Moments under Drift	Computed	3.6.1
	Rudder Model	[C1, C2] [C3, C5, C12] [C7-11]	Propeller Interaction Hull Interaction Rudder Performance	Reference Computed Computed	3.6.2 3.6.2 3.6.2
	Anti-drift Fin Model	[C1, C2] C3 C12 [C7-11]	Propeller Interaction Hull Interaction Hull Interaction Fin Performance	≈ 0 ≈ 0 Computed Computed	3.6.2 3.6.2 3.6.2 3.6.2
Hydrostat.	Geometrical Data	$[L, L_{os}, B, B_{wl}, T]$ $[C_b, C_m, C_w, DISV]$	Main Particulars Ship Coefficients	Computed Computed	- -
	Stability	[KM, KG, GM]	Stability Coefficients	Reference	-
Aerodyn.	Sail Data	$[N_{sails}, A_{sails}, x_{sails}]$	Sail Dimension and Position	Reference	3.7.1
		$[\alpha, Cl, Cd]$	Sail Performance	Computed	3.7.1
	Windage	[Ax, Ay] $[\alpha, Cx, Cy, Cn]$	Superstructure Area Superstructure Forces	Reference Reference	3.7.2 3.7.2
Propulsion	Engine	$[Pb, Ne, \eta_{shaft}, \eta_{gearb.}]$	Engine Parameters	Reference	3.8.1
	Fuel	$[SFC, \rho, LHV, CF]$	Fuel Type (MDO)	Reference	3.8.1
	Propulsor	$[type, series, D, P/D, Z, Ae/Ao, w_p, t, \eta_{0,r,p}]$	Propeller Parameters	Reference	3.8.1
	Operational Data	v_s Wind Matrix	Ship Speed Route Wind Statistics	Definition Reference	- 3.8.2
	Constraints	$\varphi = 5°$ $\delta = 15°$ $\delta = 12°$	Heel Angle Rudder Angle Anti-drift Fin Angle	Definition Definition Definition	- - -
Solver	DOF	'Surge, Sway, Heel, Yaw'	Equilibrium Computation	Definition	-

<div style="text-align: right; font-size: 4em;">4</div>

Results - Hull Design Variations

The results in this chapter are primarily presented in a flow-oriented reference frame. This has several advantages. First, the resulting force components can be identified directly as lift and drag. Physical formulations and derivations can thus be referenced straight away, such as the decomposition into linear and induced drag. Secondly, this way the coefficients represent the ship's equilibrium most directly. The ship has to overcome the drag force to move forward and uses the generated lift to balance the component of the sail forces that does not contribute to the propulsion. Whenever forces are denoted as lift F_L or drag F_D, they are oriented in a flow-fixed frame of reference. Forces F_x and F_y denote a ship-fixed coordinate system.

The calculations were done in batches, as described in Section 3.2 'Design Matrix'. This chapter treats the hull variation results from Batch #1.

4.1. B/T Ratio Variations

Lift and Drag Forces
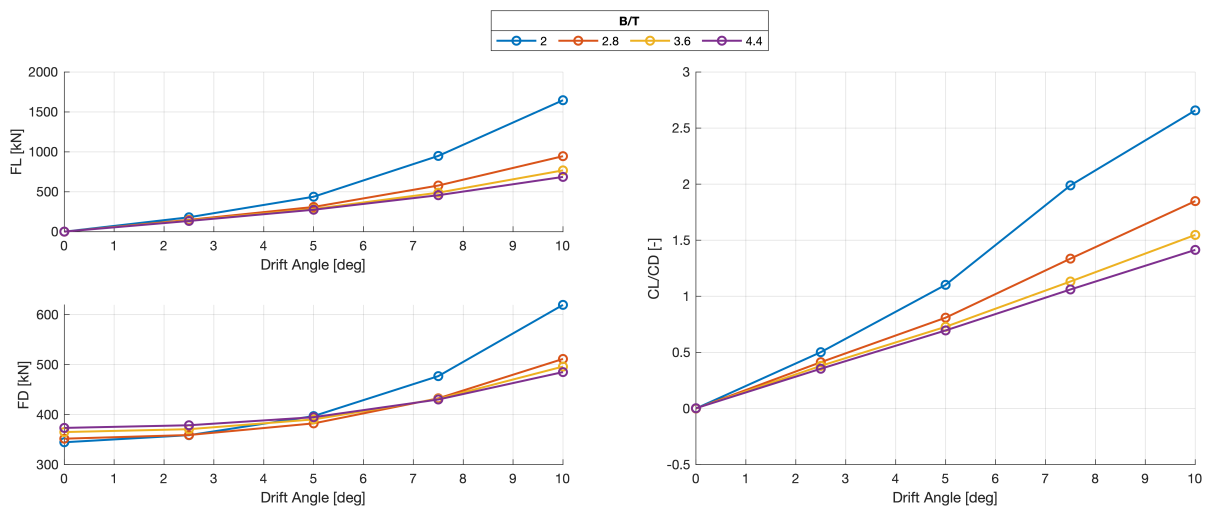
Figure 4.1: Lift, drag and lift-over-drag coefficients for different B/T ratios. (v_s: $12kn$)

Figure 4.1 shows the lift and drag forces for a range of drift angles for ships with different B/T ratios ranging from 2.0 to 4.4. For this comparison, the forces are reported instead of non-dimensional coefficients, as the coefficients include the draft as a factor, making direct comparison unclear.

Looking at the lift, it can be seen that most designs (except for B/T 2.0) behave linearly until around 5° of drift. Until then, the lift slope is also similar between the different ships. Only at higher angles do the

<div style="text-align: center;">49</div>

more slender ships set themselves apart. The expected trend of slender vessels generating more lift is visible, but for small drift angles, the effect is very small. From B/T 4.4. to 2.8, the lift only increases by around 10% at 5° of drift.

The linear component of the lift is almost unaffected by the B/T ratio. At low drift angles, where the linear component dominates, the designs with B/T 2.8 to 4.4 have very similar lift production. The differences only gain significance at higher drift angles due to non-linear effects.

The resistance is consistently lower for the more slender ships - each step in decreasing B/T decreases the resistance by around 4%. The drag decrease does not remain constant under drift. For higher drift angles, the slender hulls start to experience drag more than the wider hulls. The B/T 2.0 case especially shows a sharp increase in drag at higher angles. This increase in drag is correlated with the increased lift generation of the slender hulls. The effect can be traced back to the induced drag effect, which depends quadratically on the lift slope. As the lift increases strongly, so will the drag, especially for lifting surfaces with a very uneven 'downwash' or non-elliptical lift distribution, which is the case for a ship with a parallel mid-body and a very low aspect ratio.

The lift-to-drag ratio shows a clear trend of slender ships performing better than wider ones. Apart from the B/T 2.0 case, and especially at lower drift angles, the differences in lift are modest, and improvements are mainly due to the lower resistance.

Figure 4.2: Vortex development between drift angles of 2.5° and 7.5°.

Figure 4.2 shows the vorticity close to the hull for three ships at a drift angle of 2.5° and 7.5°. It appears that the reason for the non-linear behavior is that the majority of the lift generation is due to the generation of a strong vortex close to the bow of the ship. This vortex only develops at a higher angle. At 2.5°, it is still weak, barely reaching the aft of the ship. At 7.5°, it travels along the entire ship

length. The strength of this vortex also correlates to the trends found in the lift coefficient for different B/T ratios. For all three designs, the vortices are similarly weak at 2.5°; likewise, the lift coefficients barely deviate from each other at this drift angle. At 7.5°, the vortex is especially stronger for the B/T 2.0 case. Also the lift coefficient is then much higher for that design.

In theory the linear lift component is dependent on the geometric aspect ratio of the lifting surface. For a ship, this is the ratio T/L. This ratio increases as the B/T ratio decreases and the ship becomes more slender. However, the aspect ratio here is already very low, ranging from around 0.04 for the widest ship, to 0.06 for the most slender. Therefore it seems that the effect of B/T on performance under drift is largely based on non-linear lift generation and on differences in resistance.

Moment Generation
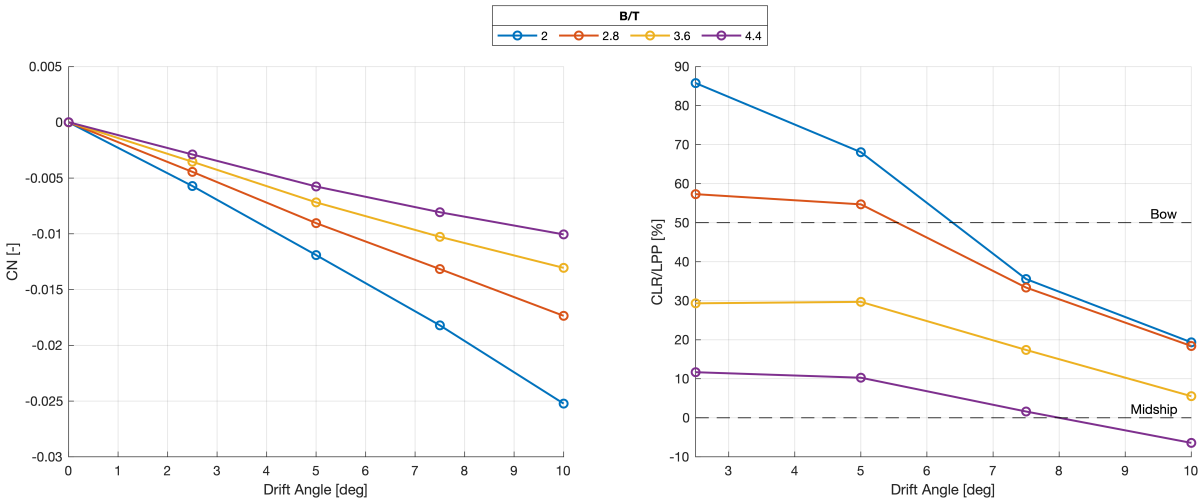
Figure 4.3: Moment coefficient, and non-dimensional CLR for different B/T ratios.

Figure 4.3 plots the moment coefficient and center of lateral resistance (CLR) for the various designs. The CLR is non-dimensionalized with the ship's length, so a value of 0 represents midship, and ± 0.5 the bow/aft, respectively. The moment is found to be larger for the more slender hulls. As a result, the CLR is further forward from midship for the slender ships. The effect is significant, as the widest hull at 2.5° of drift has a CLR around 20m ahead of midship, while the most slender hull has a CLR around 70m ahead of the bow. Generally, having a CLR close to or slightly ahead the center of effort (CE) of the sails is beneficial, as it ensures better trim in the sailing condition and less rudder action necessary to provide that moment balance. For the Silenseas cruise ship case the CE is assumed at midship given the longitudinally centered positioning of the sails, so a CLR close to midship is most favorable.
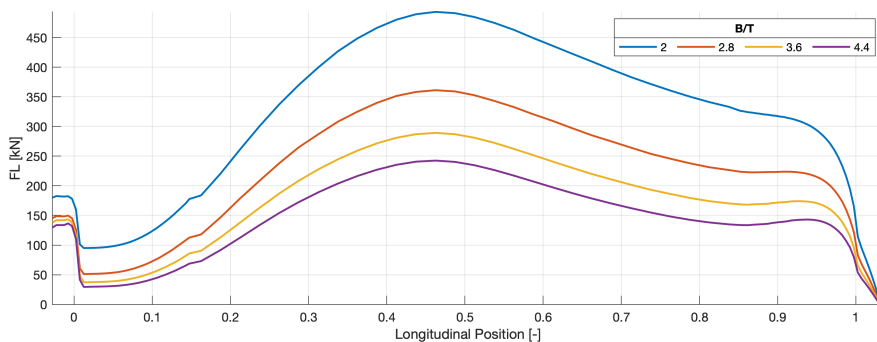
Figure 4.4: Bow-to-stern lift integration for different B/T ratios, at 2.5° of drift. (v_s: $12kn$)

Earlier it was found that the lift generation between the hulls is similar at low drift angles. The moment, on the other hand, already deviates significantly at low drift angles. Figure 4.4 shows the integration of

the lift force from bow to stern at a drift angle of 2.5°. The x-axis shows the non-dimensional position, with 0 being the aft perpendicular and 1 the bow perpendicular.

The lift distribution of the hulls (and the final lift forces) are quite similar between designs. However, there is a large difference in forces at the bow, where slope of the curve, i.e. dF_L/dx, is much higher for the slender hulls. This results in a much stronger moment, even if the final forces are similar. Since the bow region has the most substantial impact on the moment, the large forces at the bow are much more impactful than the recovery towards the aft of the ship.

Overall, the better lift performance of slender ships does not come with a resistance penalty. In fact, the improvement in resistance is almost as large as the improvement in lift. This means that strictly from a lift-to-drag perspective, the slender ships are always better. However, this benefit comes with unfavorable (higher) moment generation and possibly stability concerns, both of which will be picked up again in Chapter 7 'Results - Power Prediction in Sailfish'.

4.2. Skeg Variations

Lift and Drag Forces
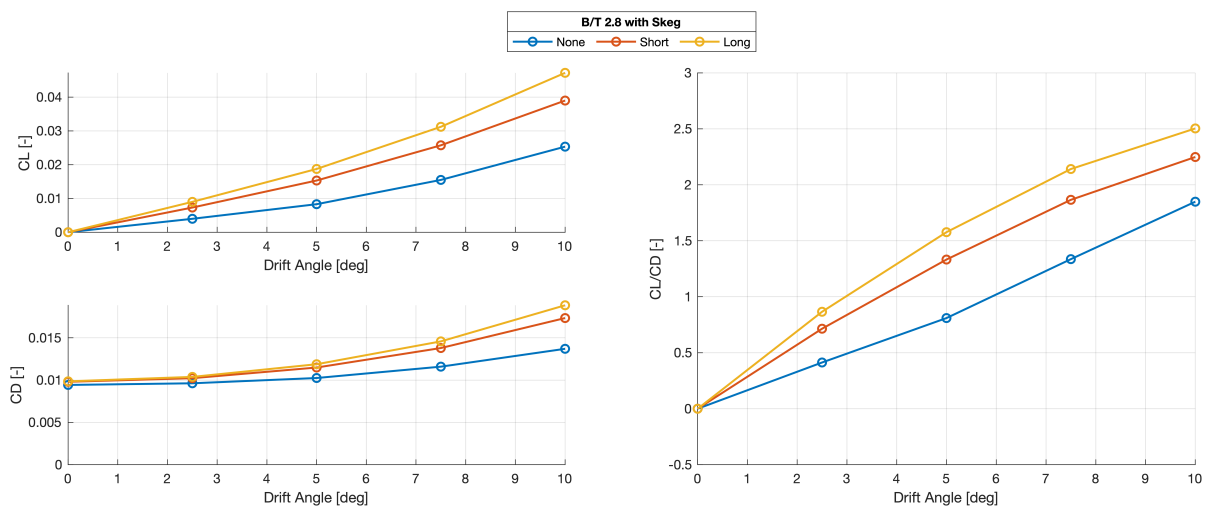
Figure 4.5: Lift, drag and lift-over-drag coefficients for different skegs.

In Figure 4.5, the lift, drag, and lift-to-drag coefficients are shown for the unappended hull and the short/long skeg case. It can be seen that the skeg increases the lift significantly throughout the range of drift angles. There is a resistance penalty of 3.9% for the short skeg and of 6% for the long skeg, which further amplifies with increased drag at higher drift angles. Still, the skegs also show favorable performance in the lift-to-drag ratio, with the appended cases outperforming the bare hull for all drift angles.

Compared to the changes in hull shape, there is a visible improvement in the linear lift slope for the skegs. Figure 4.6 shows the decomposition into linear and non-linear lift. This decomposition is based on the maneuvering model used at MARIN, described in Section 3.6 'Post-Processing of Hydrodynamic Data'. The plot on the left shows the decomposition for various drift angles and designs, while the plot on the right shows the associated coefficients, i.e. the (effective) aspect ratio for the linear lift, and cross-flow drag coefficient for the non-linear lift.

Mainly an increase in the linear lift component can be noted. The effective aspect ratio increases by a factor of 3 when adding the long skeg. The non-linear lift also improves, but much more modestly. Therefore, contrary to the effect of reducing B/T, the better lift performance already becomes significant at low drift angles when adding the skeg. With the linear lift component impacted, the performance is better right away.
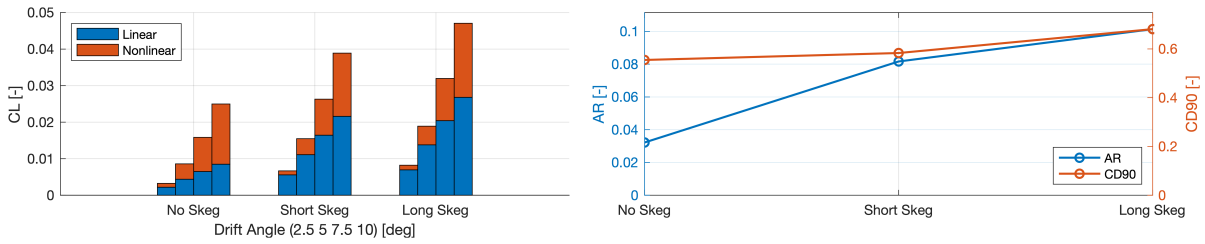
Figure 4.6: Left: Linear and non-linear contributions to the lift coefficient for different drift angles and skegs. Right: Aspect ratio and cross-flow drag coefficients for different skegs.

Moment Generation
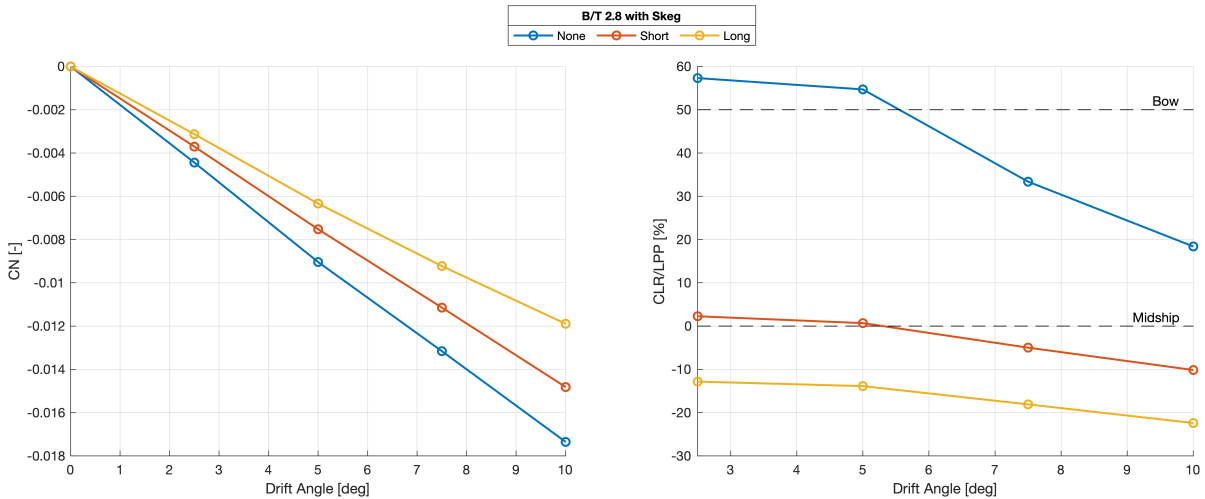
Figure 4.7: Moment coefficient, and non-dimensional center of lateral resistance for different skegs.

A clear improvement is visible in the moment generation shown in Figure 4.7. This is logical, as adding a lifting surface towards the aft of the ship will counter the earlier shown effect of the bulk of the lift being generated at the forefront of the ship. By developing a lift force at the aft of the ship, the moment arm is reduced. As a result, C_N is lower when skegs are introduced, and the CLR shifts back considerably. Even adding the short skeg moves the CLR back so much that it falls into the optimal region around midship for all drift angles. The long skeg does not further improve the CLR position, arguably even worsening it again as it falls behind the CE at midship.

This can be confirmed by looking at the lift integration shown in Figure 4.8. The forces on the hull are nearly identical for the front two-thirds of the ship. Only at the aft, the lift increases significantly when adding the skegs. This skeg force acts far behind the original CLR, and is therefore very effective at moving it further aft.
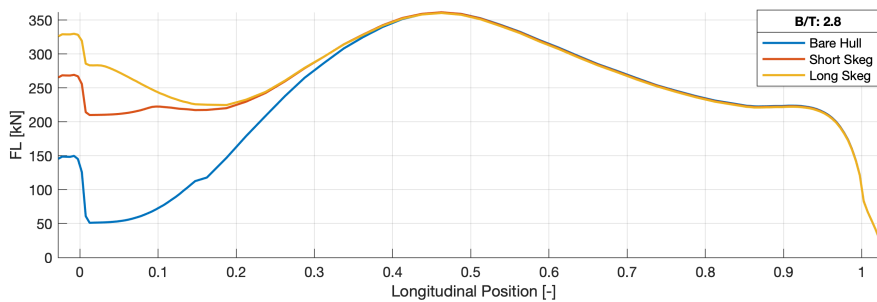
Figure 4.8: Bow-to-stern lift integration for different skeg configurations, at 2.5° of drift. ($v_s : 12kn$)

Performance Indication

Only evaluating designs through their lift-to-drag ratio can be deceptive for wind-assisted ships. While it is true that a higher lift generation is beneficial for sailing equilibrium, the objective is not to maximize lift, but to minimize resistance for a particular lift force. To sail in certain wind conditions, there will be a fixed side force on the ship due to the sails. To sail as effectively as possible, the ship should be able to balance that side force with as little resistance increase as possible.
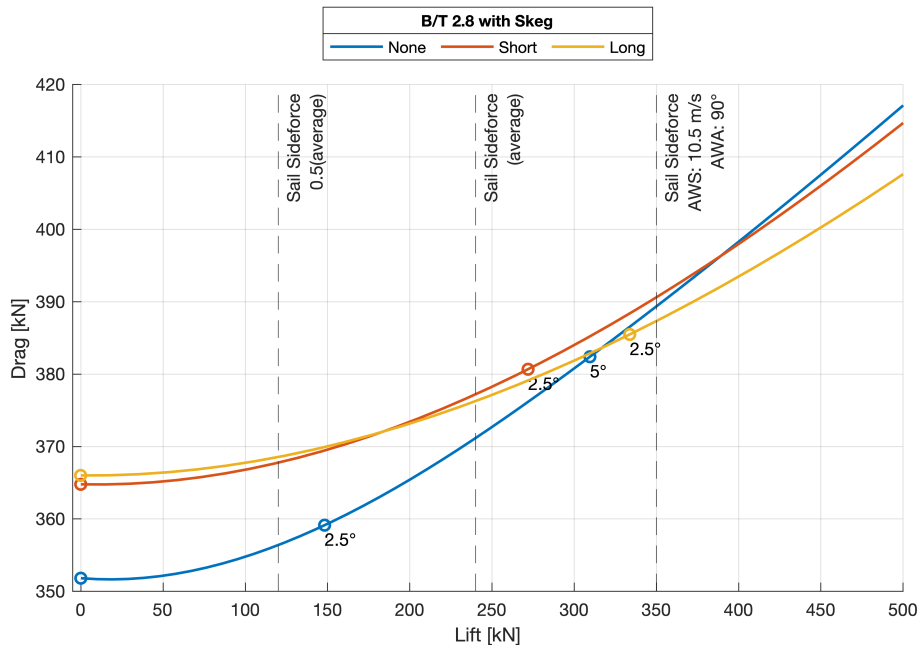
Figure 4.9: Effective performance of the skeg for side force generation.
Corresponding ship drift angles annotated.

Figure 4.9 shows the drag generated by the different hull designs for a set amount of lift production. The unappended hull has the lowest resistance, but as the lift requirement increases, the appended hulls generate the same lift under less drag. At around 310kN of lift, the long skeg starts to outperform the bare hull. This means that the hull with the long skeg is more efficient when sailing in a condition with more than 310kN of sail side force.

The question becomes whether conditions of more than 310kN of sail force are encountered often enough to make the skeg viable. For this, three values are highlighted on the x-axis. The first two show 50% and 100% of the average sail side force expected based on MEPC.1/Circ.896 wind statistics, as described in Section 3.8 'Operational and Supplementary Data', and a preliminary sail force calculation based on sail coefficients from Section 3.7 'Aerodynamic Data'. The reason to highlight both 50% and 100% of this force is that not all of it will have to be balanced by the hull. Considering the moment balance, some rudder action will likely be necessary, which causes additional lift. A full equilibrium state analysis would give the complete picture, taking into account wind statistics and rudder action. This is done later with Sailfish, in Chapter 7 'Results - Power Prediction in Sailfish'.

This plot already indicates if the improvements are in the correct order of magnitude. Even at 100% of sideforce balance, the bare hull is still more effective at the most probable force condition. The other annotated point at 350kN is the beam reach (90° TWA) condition for which the ship becomes fully sail-propelled. Under the assumption that the operational speed is fixed, the forces on the sail will not exceed this point, as for higher wind speeds, the sails would be reefed. Even at this extreme condition, the long skeg is barely more effective, and considering that 10-20% of sideforce may very well be attributed to the rudder, it is implausible that the skeg is a beneficial appendage from a sailing perspective. It can also already be noted that the short skeg is never the optimum solution, as it never causes less drag than both the bare hull and long skeg case.

Considerations such as maneuverability could still affect this conclusion. On the plot lines, the corresponding drift angles are annotated. The appended cases need a much lower drift angle to reach the lift condition. When the bare hull is already at 5°, the appended ships are only at about 2.5°.

4.3. Influence of B/T Ratio on Skeg
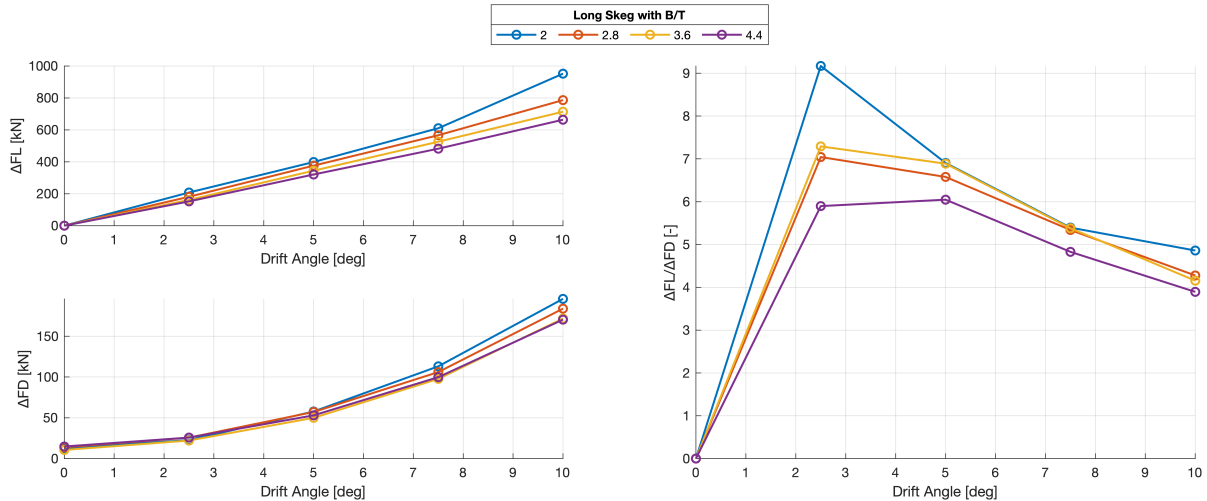
Figure 4.10: Forces generated by the long skeg for ships with different B/T ratios.
$(\Delta F_{L,D} = F_{L,D \text{ with skeg}} - F_{L,D \text{ without skeg}})$

The plots in Figure 4.10 show the forces generated by the skeg only, so that their relative performance for different B/T ratios can be considered. The forces by the skeg are calculated by subtracting the result for the total force of a ship without a skeg from the ship with a skeg. This way, the force developed on the hull due to the skeg is considered, which would not be the case by simply looking at the forces on the skeg surface.

The effect of the skeg is slightly more pronounced at lower B/T ratios, with both lift and drag contributions being higher. This is likely due to geometrical variations in the designs. For the ship to be more slender under constant displacement, the ship is scaled down in y and scaled up in z. In doing so, the projected area of the skeg increases, as it also has to be scaled in z with the same factor to still extend between the depth at the parallel midbody of the ship to the depth at the aft of the ship. Ships with higher draft can therefore be seen as slightly more suitable for the introduction of the skeg, as they provide more room for the skeg to be added, even if the effect is minimal.

Furthermore, the skeg is most effective at lower drift angles, having a maximum lift-to-drag ratio between 2.5° and 5°. This is advantageous as the ship will likely sail at low drift angles as well.

4.4. Deadrise Variations

Lift and Drag Forces

The deadrise angle is another potential hull modification that could improve the hydrodynamic lift generation. Figure 4.11 shows the lift and drag coefficients for different deadrise angles. Only the results for B/T 2.8 are illustrated here, as the trends are consistent across all B/T variations. The lift improves slightly, but only for high deadrise and drift angles. At low drift angles, there is no significant improvement in lift generation. Effects are marginal and not consistent - from one drift angle to the next, different deadrise angles become better than others. This suggests that the slight improvements are also affected by the uncertainty of the simulation.

Nonetheless, at low drift angles, the lift-to-drag performance is consistently higher with deadrise. This stems from the lower resistance of the hull when the deadrise is introduced. The more deadrise angle is introduced, the lower the drag coefficient becomes. The only exception is the effect of induced drag, which only becomes apparent at high drift angles.
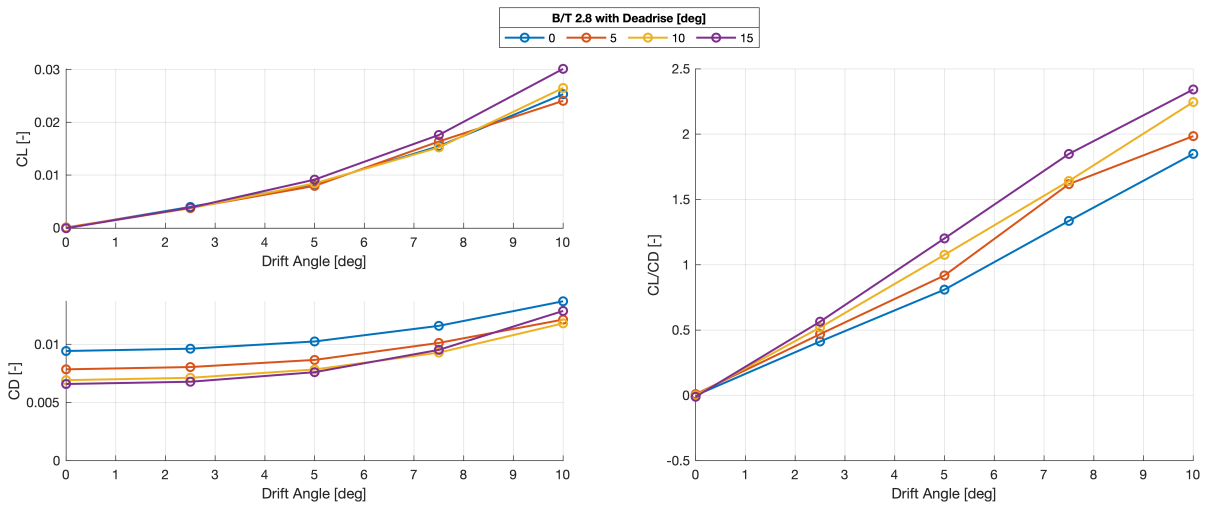
Figure 4.11: Lift, drag and lift-over-drag coefficients for different deadrise angles.

At first, this effect is counter-intuitive. Introducing deadrise causes the ship's wetted surface to increase, resulting in a higher frictional resistance. Looking at the resistance decomposition in Figure 4.12 gives more insight. It is evident that the improvements in resistance due to deadrise stem purely from a reduced transom drag. The resistance of the rest of the hull remains largely unchanged.
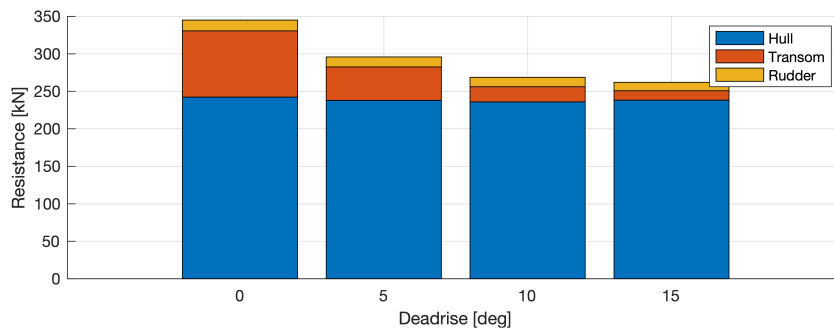
Figure 4.12: Resistance decomposition for different deadrise angles. (v_s: $12kn$)

Introducing deadrise reduced the transom area. The transom resistance is considerable, as it is a region with very low pressure and reversed flow. This is illustrated in Figure 4.13, where the pressure coefficient on the transom surface is plotted for the 0° and 15° deadrise cases. The area is smaller, but more importantly there is a much better pressure recovery on the triangular aft section. While the 0° case has a strong trailing low-pressure region, the pressure on the transom for the 15° case is almost zero. The introduction of the deadrise leads to a more streamlined flow, with less separation at the transom, reducing the overall resistance of the ship.
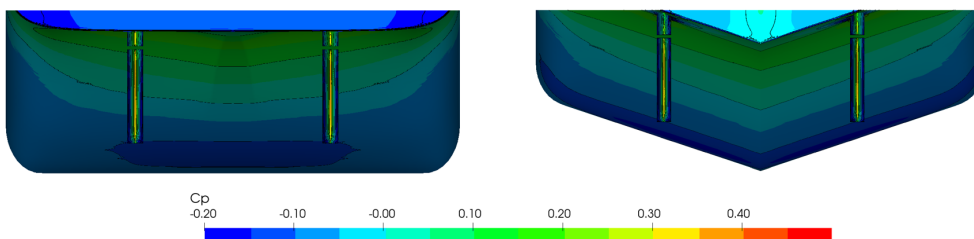
Figure 4.13: Pressure distribution on the transom for 0° and 15° deadrise cases.

There are two aspects to interpret from these results. First, no significant improvement in lift through the introduction of a deadrise angle can be noted. Only in the extreme cases, i.e. very large deadrise angle and drift angle, the lift generation is affected.

The improvements in resistance should be taken with caution. While in theory, the reduction in drag would be beneficial, this result likely does not translate to reality as it stems purely from the difference in pressure on the transom.

The computations are done in a steady setting with a double-body approximation. This neglects the pitching motions and overall trim of the ship. The ship with deadrise would have a longitudinal center of buoyancy that is shifted forward, leading to increased submersion in the aft. Furthermore, there is much less reserve buoyancy for the narrower aft of the ship with deadrise, meaning that pitching motions would also lead to considerably higher transom submersion. In effect, the transom resistance is a very fickle phenomenon that can easily be affected by factors beyond the current modeling approach, including trim, pitching, or wave-induced and wave-making resistance.

Moment Generation

There is a correlation between the deadrise angle and the moment coefficient. The increased deadrise angle helps reduce the moment and, as a result, reduces the CLR. However, the effect is very slight, much smaller than that of the skeg, and also lower than the effect of increasing B/T. Only for a large deadrise angle does the CLR drop, and even then, the change is still below 20% compared to the original value.
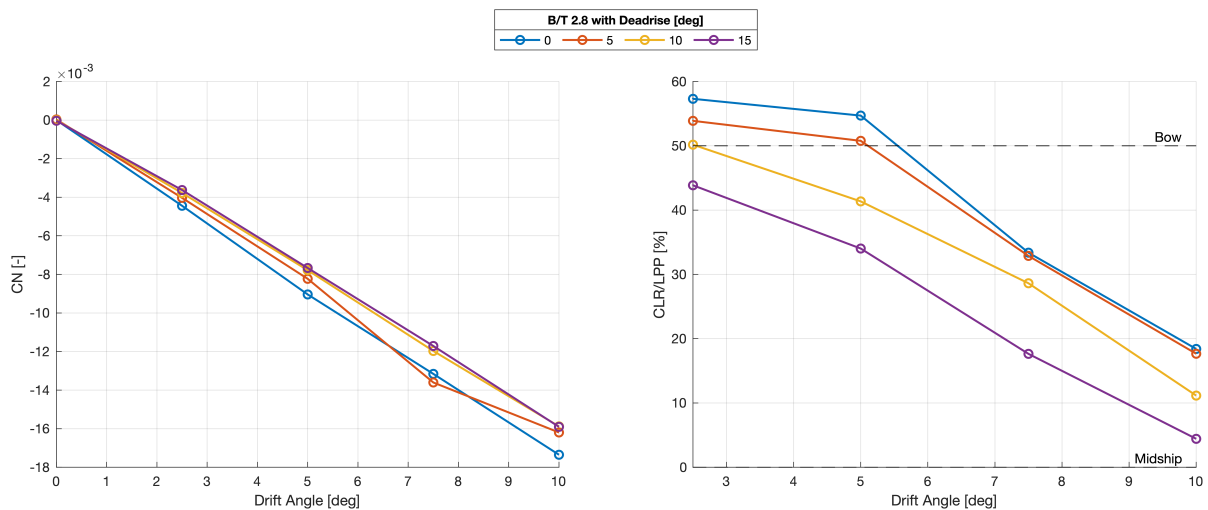
Figure 4.14: Moment coefficient, and non-dimensional center of lateral resistance for different deadrise angles.

4.5. Comparison to SURSIM

SURSIM is an empirical tool to estimate hull forces in a maneuvering context, as described in more detail in Section 2.2.3 'SURSIM'. This section compares the results from CFD with those of equivalent computations in SURSIM.

4.5.1. B/T Ratio

Figure 4.15 shows the lift and drag coefficient plotted from CFD and SURSIM calculations. While the trend of slender hulls producing more lift matches, the magnitude of the lift force is much larger for SURSIM. The curves also follow a much more linear curve, and the results are more uniformly spaced. While for the CFD results, the lift improvement only comes at higher drift angles, SURSIM shows improvement much earlier. The stark difference for the B/T 2.0 case also does not appear in the SURSIM results.

The resistance at 0° of drift is well predicted, and accurate within 1.5% of the CFD results. For higher
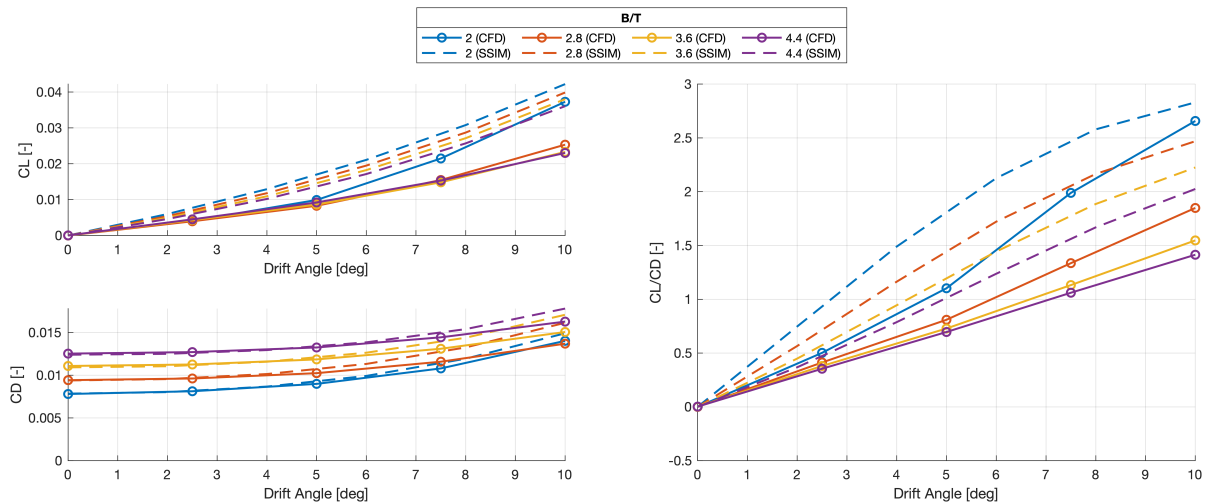
Figure 4.15: Comparison between CFD and SURSIM results of lift, drag, and lift-over-drag coefficients for different B/T ratios.

drift angles, the drag is slightly overestimated by SURSIM, but the overall match between the results is still good. The spike in the induced drag for the B/T 2.0 case is not captured, as can be expected given the lift results.

The same differences can be noted for the lift-to-drag curves. Especially for lower angles, the values are quite off due to the differences in lift estimation between the two methods. While the overall curves are not too far from each other, there is not enough fidelity in the SURSIM results to differentiate accurately between designs. This is because the discrepancy in the values is still much larger than the difference between the designs.

Figure 4.16 dives deeper into the lift prediction by SURSIM, which is the largest source of error in the data. In 4.16a, the SURSIM results are subdivided into linear and non-linear components. Contrary to the CFD results, where the improvements in the lift were predicted to be very non-linear, SURSIM shows a clear improvement in the linear lift for the more slender ships.
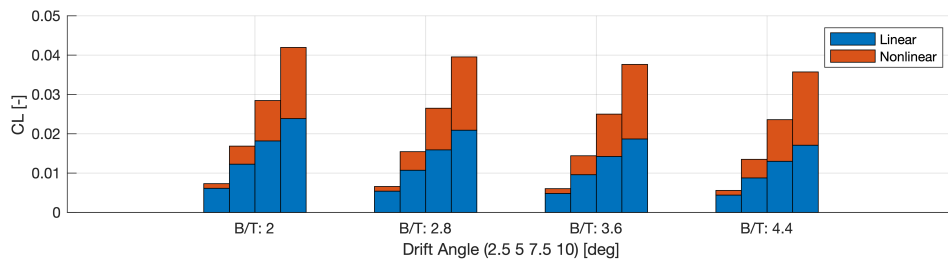
(a) Linear and non-linear contributions to the lift coefficient, for different drift angles and B/T ratios, from SURSIM.
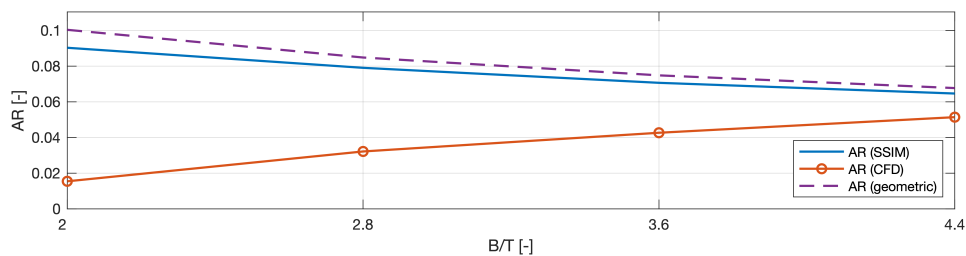
(b) Comparison between CFD and SURSIM fitted lift coefficients.

Figure 4.16: Lift decomposition of SURSIM results.

Looking at the corresponding linear lift coefficient in 4.16b, the aspect ratio reflects this trend. The aspect ratio in SURSIM follows a straight line, indicating a geometric relation. This can be verified with a rudimentary calculation of the aspect ratio, which was done by calculating the aspect ratio over 20 sections:

$$AR = 2AR_g = 2\frac{1}{20}\sum_{i=1}^{20}\frac{T_i}{LPP} \tag{4.1}$$

The factor of two accounts for the double-body approximation. Looking at the resulting line plotted in the figure, it can be seen that SURSIM closely follows the geometric expectation. The fact that SURSIM ends up with slightly higher values is also logical, as the bulbous bow and rudder were neglected in the hand calculation, both of which will further increase the aspect ratio.

While SURSIM follows a valid approach, the trend from the CFD results is actually the opposite. The linear lift contribution (i.e. the aspect ratio) increases for the wider hulls, which is opposite the geometrical expectation. The flow around the ship is too complex to be described fully using the maneuvering model with just aspect ratio and cross-flow drag coefficients alone.

If the theoretical equations do not fit well, it cannot be expected that SURSIM will give more accurate results. It was shown that the vortex forming along the hull strongly correlates to the lift generation. This is a phenomenon that SURSIM, and the underlying wing theory, is not able to predict.
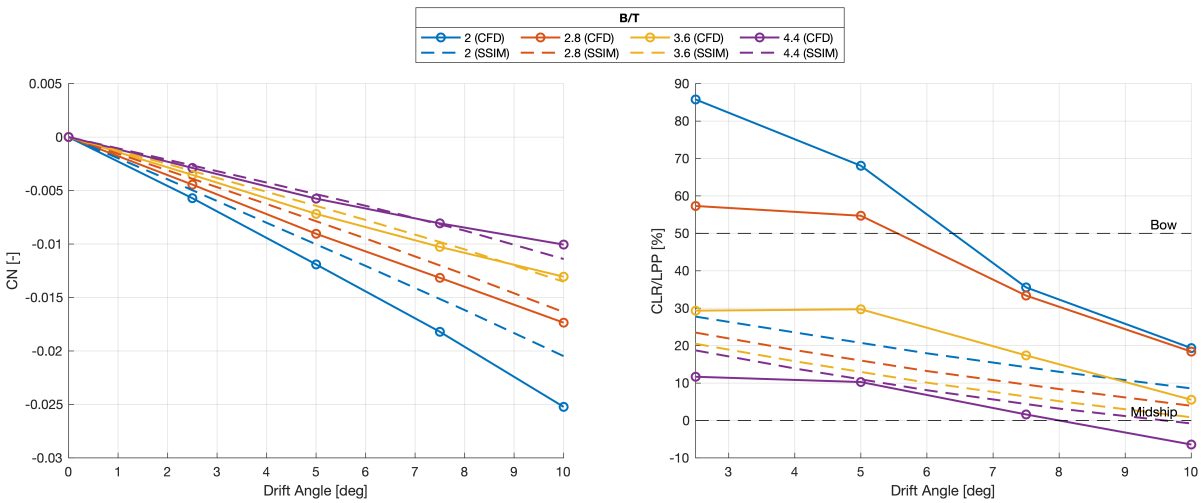
Figure 4.17: Moment comparison between CFD and SURSIM results for different B/T ratios.

Figure 4.17 shows the comparison in moment estimation between the SURSIM and CFD results. The moment coefficient is estimated quite well, with errors increasing for the most slender ship, which was also found to show the most non-linear lift generation. It seems that SURSIM is able to predict the distribution of pressure on the ship quite well, but the magnitude differs. As a result, the moment coefficient shows good agreement, but the estimation of the CLR is very off due to the substantial differences in estimating the lift. Alternatively, the agreement could just be a result of a compensation of errors in lift and moment estimation.

4.5.2. Skeg

To avoid re-iterating errors in the force prediction for the hull designs, the hull forces are subtracted from the results reported in this section. This allows comparison of the skeg forces only. Figure 4.18 shows the forces on the long skeg for all B/T ratios. The trends are similar in that the skeg is more effective for the slender ships, but SURSIM under-predicts the lift considerably, so a comparative analysis between designs would not be possible using just the SURSIM calculations. The drag is also different; SURSIM estimates a higher resistance but lower drag under drift compared to the CFD results. While these opposing effects cancel out each other in the lift-to-drag performance at higher angles, leading to almost identical results, the overall agreement between the results is still considered poor.
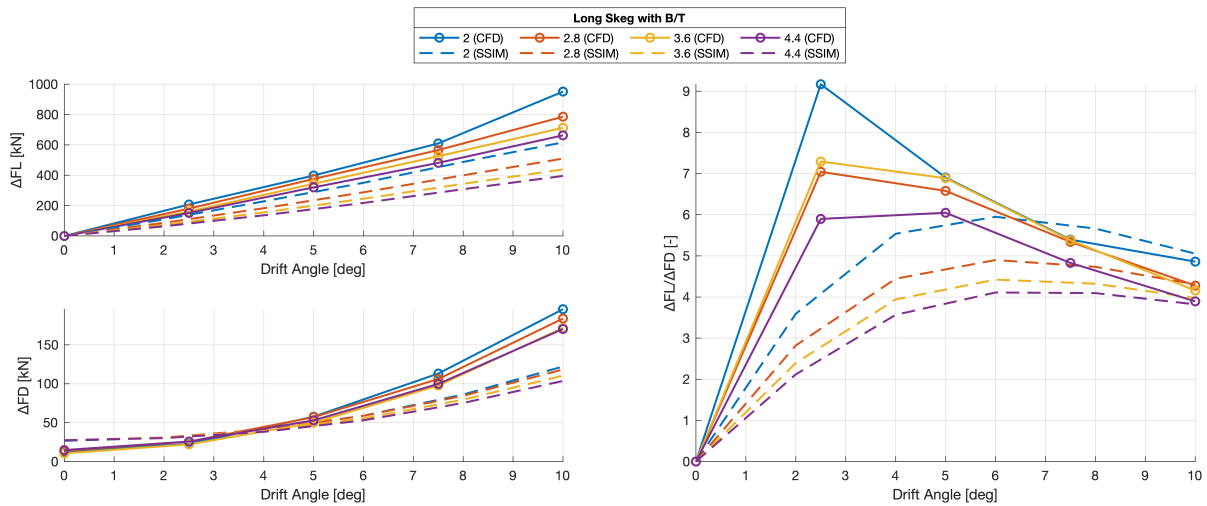
Figure 4.18: Comparison between CFD and SURSIM results of lift, drag, and lift-over-drag coefficients for different skegs. $(v_s: 12kn)$

4.5.3. Deadrise

The effect of introducing deadrise is not captured well in the SURSIM results. Just as before, the differences in the forces are plotted so as not to repeat the errors between the original designs. The CFD results show increased lift force generation due to the deadrise at higher drift angles. This is to be expected due to the more effective foil shape of the hull through the introduction of the deadrise, which sharpens the edge and slightly increases the aspect ratio of the hull. The aspect ratio increases as displacement is kept constant between designs, so by 'cutting off' part of the hull through the deadrise angle, the overall draft increases to compensate. The SURSIM results do not show this, with the lift being effectively constant throughout the design variations, if not dropping slightly.
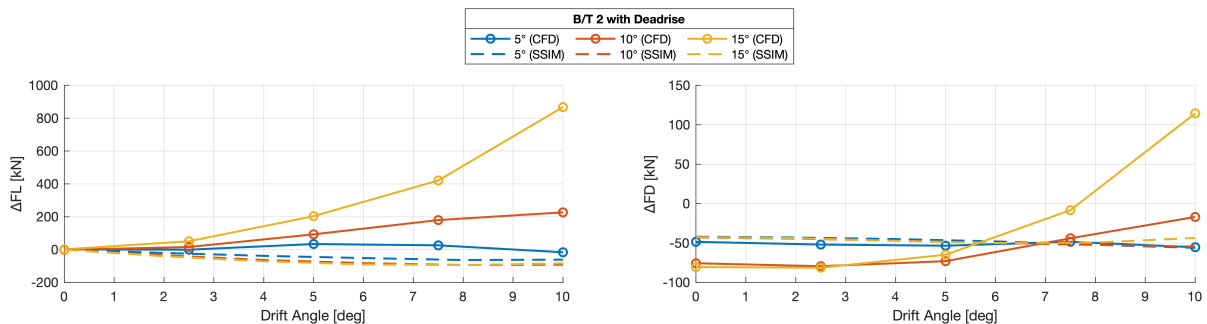
Figure 4.19: Comparison between CFD and SURSIM results of lift, drag, and lift-over-drag coefficients for different deadrise angles. $(v_s: 12kn)$

It was also shown that introducing the deadrise lowers the resistance due to the better pressure recovery at the transom. The SURSIM results do not show this effect. A slight decrease in drag is visible for all deadrise cases, but neither the magnitude nor trend of the drag force for different designs or drift angles matches the CFD results. Overall, the SURSIM results do not capture the effects of the deadrise angle.

5

Results - Rudder Interaction Effects

The complexity of the flow at the aft of a ship begins with the development of the boundary layer that grows progressively thicker from bow to stern, eventually contributing to turbulent flow conditions in the ship's wake, shaped by the hull geometry. The rudder operates in this environment, subject to a complex three-dimensional flow. In this chapter, the interaction of the rudders with each other, with possible skeg configurations, and the hull itself is studied and quantified.

The ship is configured with two rudders, one for each shaft line. Under drift, these are referred to as 'inner' and 'outer' rudders. The inner rudder is the rudder first encountered by the flow, while the outer rudder is the 'downstream' rudder.

As in the previous chapter, careful consideration of the frame of reference for the various angles of different surfaces is crucial for a correct analysis. In this chapter, rudder angle δ refers to the angle of the rudder with respect to the ship, while the angle of attack α refers to the angle of the rudder with respect to the flow.

The calculations were done in batches, as described in Section 3.2 'Design Matrix'. This chapter treats the rudder variation results from Batch #2.

5.1. Lift and Drag Curves

Figure 5.1 shows the lift forces on the rudders. The first column shows the inner rudder, the second the outer rudder, and the third the summed contributions. The top row shows the rudder forces for the most slender ship, and the bottom row the widest ship. The plots show results for 0° and 6° of drift for both no-skeg and long-skeg cases.

The first thing to note is that the lift is linear with the angle of attack. This is because the rudder is a high aspect ratio appendage; linear effects dominate, and non-linear effects are minimal. The ship has an aspect ratio of around 0.05 - the rudder of 1.5.

Interactions become apparent when looking at the plots individually. Starting with the inner rudder, it can be seen that all lines fall very closely to each other. This means that the forces on the inner rudder are not strongly affected by the introduction of the skeg, or by the drift angle. Also, the forces for the B/T 2.0 (top plot) and B/T 4.4 (bottom plot) are very similar. This shows that the inner rudder does not suffer from strong interaction effects. The only aspect to note is that the lift force is not precisely zero at a zero angle of attack. This shows that some bending in the flow slightly changes the inflow angle. This will be looked at in more detail later on.

The outer rudder tells a different story. This rudder is positioned 'downstream' under drift and is therefore more susceptible to interaction effects. Overall, lift generation is weaker for the outer rudder. While the inner rudder reaches lift forces of over 250kN, the outer rudder only reaches 210kN. Differences for different B/T ratios are also visible, with the slender ship having lower rudder lift generation overall.
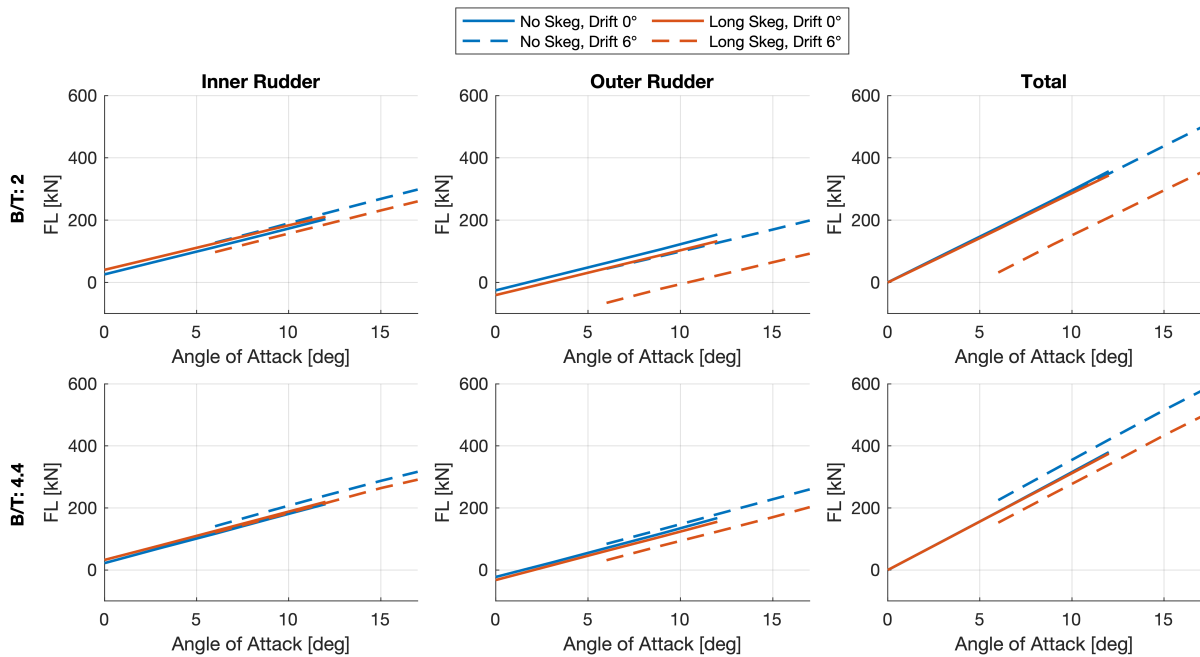
Figure 5.1: Rudder lift force for different B/T ratios, skeg configurations, and drift angles. $(v_s: 12kn)$

The strongest outlier is found to be the slender ship with long skeg. The dashed lines show how the lift changes under drift. A significant reduction in lift can be noted, with positive lift only generated above a 10° angle of attack. This indicates strong interaction effects.

As a result, looking at the total forces, this is also where most disparity is found. Introducing drift for the B/T 2.0 ship with skeg leads to a much worse rudder performance, while the performance without skeg (blue lines) is almost identical. In the bottom plot, only a much more modest drop in performance is found when introducing the skeg. In turn, without skeg, the rudder performance actually appears improved, as the dashed line is above the solid line, indicating higher rudder forces under drift.

While the effects look significant, the question remains whether these changes in force are actual losses or just offsets in the inflow angle, which could be rectified by adjusting the rudder angle. Based on the results above, for the most extreme case of having a slender ship with skeg under drift, the outer rudder angle would have to be adjusted by over 10° to reach a balanced performance. A first indication comes from the lift-to-drag ratio, shown in Figure 5.2.

From the figure, it can be seen that there are losses associated with the interaction; otherwise, all lift-to-drag curves would still look identical. A clear takeaway is that the performance of the inner rudder is always better than that of the outer rudder. The total performance almost always drops with drift, apart from the case of having a wide ship without skeg. The most significant impact is on the outer rudder for the slender ship with skeg, where the lift-to-drag ratio drops significantly and stays below one all the way to 12° of angle-of-attack.
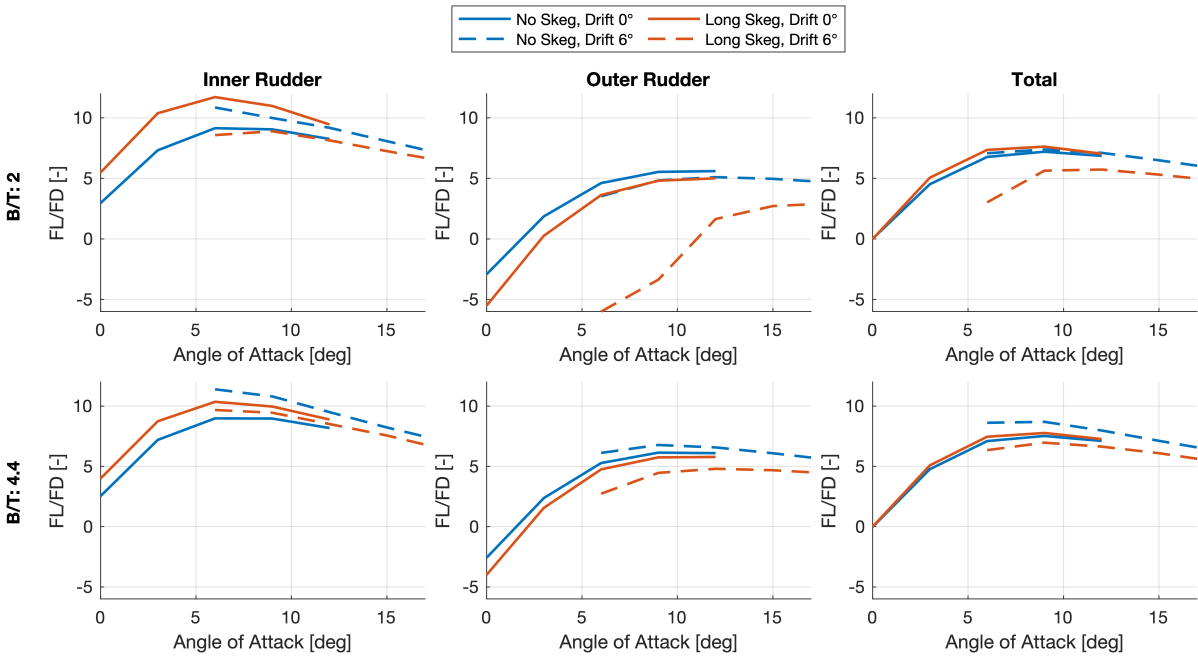
Figure 5.2: Rudder lift-over-drag ratio for different B/T ratios, skeg configurations and drift angles.

5.2. Effective Rudder Angle

The performance drop can be explained by looking at the effective rudder angle, which was calculated from the flow direction ahead of the rudder (25% of the chord length ahead of the leading edge). The results are illustrated in Figure 5.3. The z-position is non-dimensionalized, so position 0 indicates the top of the rudder, and position 1 the bottom edge. Plotted are the angles for both rudders, for all 4 designs, with and without drift.

(a) Ship with B/T: 2   **(b)** Ship with B/T: 4.4
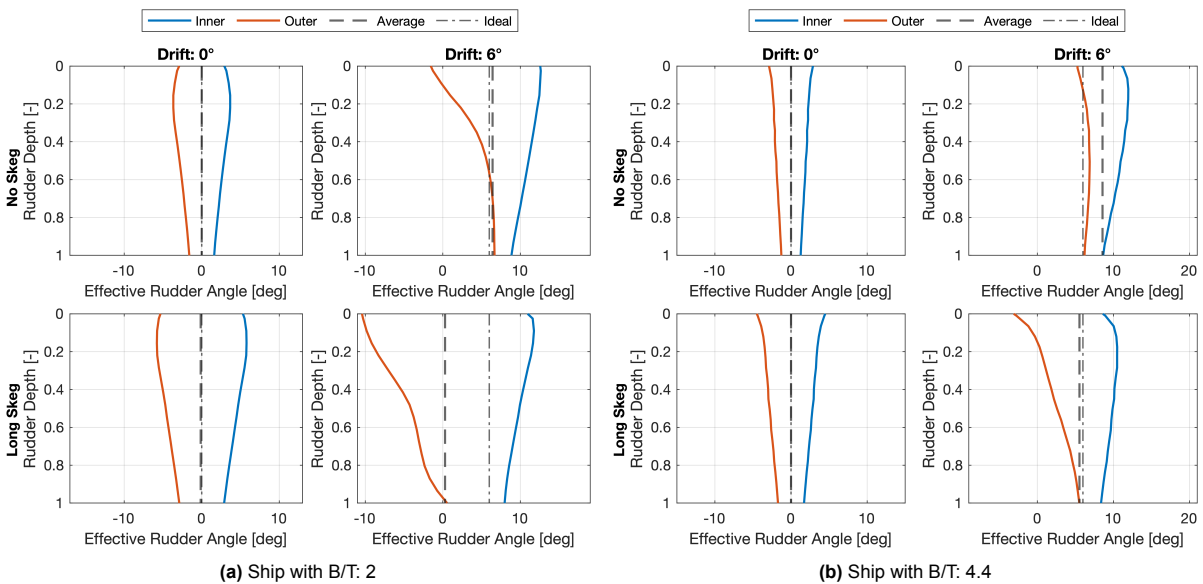
Figure 5.3: Effective rudder angle with and without drift, for different ships.

In an undisturbed case, all lines would fall onto the 'ideal' line, the expected inflow angle. However, it is clear that the outer rudder always experiences a reduction, and the inner rudder an increase in the effective rudder angle. Without drift, these changes are symmetrical so that the total force is still in line with expectation, albeit with slight losses.

Under drift, the outer rudder receives a much more uneven inflow, especially for slender ships and with skeg. This is logical, because there is more physical proximity between the rudders and the skeg for the slender ships, as the ship is more narrow. This amplifies the interaction effects.

Some of these effects can be rectified by altering the rudder angle, which can shift the lines to either higher or lower angles. However, the variations in z-direction cannot be captured. Losses associated with the strong variations in that dimension, especially visible for the slender ships and with skeg, cannot be recovered.

5.3. Flow Straightening

The effects can be attributed to flow straightening. Figure 5.4 shows how the flow angle changes in the aft of the hull, with and without skeg. It can be seen how the flow wraps around the ship so that the outer (bottom) rudder receives an inflow much lower than the 6° of the free stream. The effect is much more pronounced for the slender ships, and the skeg severely amplifies it further.

Earlier results showed that for the B/T 4.4 case without a skeg, the rudder performance improved under drift, leading to an effective negative flow straightening. The top right figure explains why. There is a strong straightening effect on the inner (top) rudder, so the performance of that rudder is increased. However, the outer (bottom) rudder is far enough away for the flow to readjust, leading to almost no straightening effect on the leeward side. As a result, the 'average' inflow angle is greater than 6°.

(a) Without Skeg

(b) With Skeg
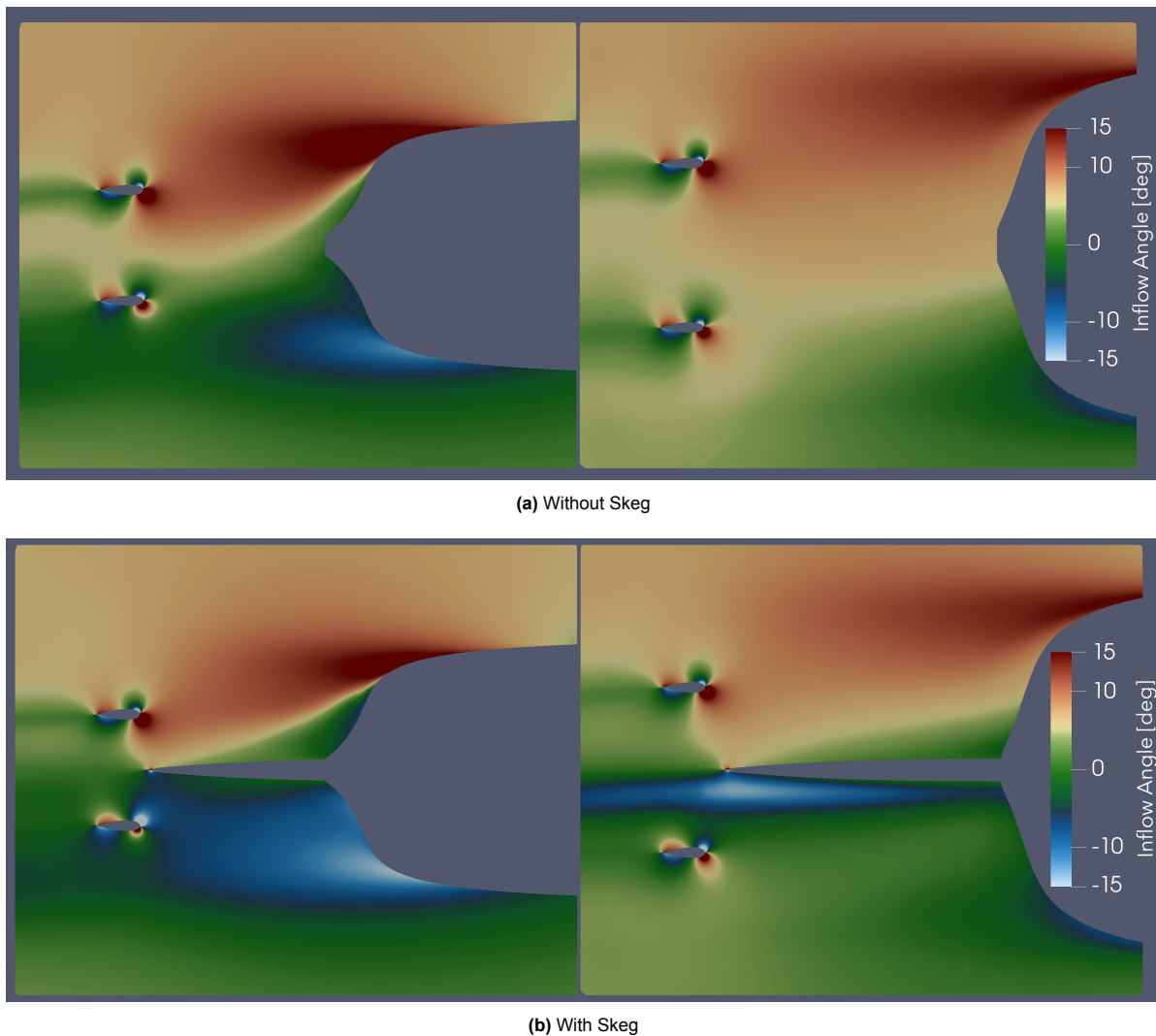
Figure 5.4: Flow angle under 6° of drift for B/T: 2.0 (left) and B/T: 4.4 (right).

5.4. Rudder Coefficient Fit

The effects described in this chapter must be quantified to be correctly applied when evaluating the ship's performance in sailing conditions in Sailfish. The fitting process is described in Section 3.6.2 'Rudder and Anti-drift Fin'. Table 5.1 shows the resulting coefficients for each design.

Starting with the lift, the three lift coefficients $C_{7,8,9}$ are summarized into a lift slope coefficient for a more accessible analysis, according to Equation 3.13. The earlier findings can be confirmed. The lift performance is higher if the ship is wider and there is no skeg, as both design choices increase the interaction effects.

The drag consists of the form drag coefficient C_{10}, and the Oswalds efficiency C_{11}. With the skeg, the form drag decreases but the induced drag (described by the Oswald efficiency factor) increases. It is likely that this is a phenomenon linked to the fitting procedure, i.e. that the drag curve is more non-linear with the skeg added, and therefore a better fit is achieved with attributing a larger non-linear contribution. The trends are captured, but the flow might be too complex for the underlying wing theory. While the differences look drastic, the total drag only varies slightly between designs. At 3°, the differences in C_D between designs are under 10%.

It should be noted that C_{10} is not used in the further analysis in Sailfish, and illustrated here only for completeness. This is because the rudder drag at zero degrees of drift is already part of the C_x coefficient of the hull.

C_3 describes the flow straightening, so the effect of the hull on the rudder. As expected, the straightening only really gains importance when the skeg is introduced, and then the impact on the slender ships is much more significant. The negative straightening effect of the wide hulls without a skeg, described in the previous section, is also apparent in two cases.

C_{12} is the second interaction coefficient, describing the effect of the rudder on the hull. The rudder alters the pressure distribution on the hull, which generally increases the overall forces. Without skeg, this coefficient is more or less constant. This makes sense, as the effect on the hull should be roughly the same. Introducing the skeg makes the hull interaction much stronger for the narrow ships. This is because for the slender designs, the physical proximity between rudders and skeg is increased.

The rudder model now allows to accurately incorporate the specific rudder performance of each design in the performance analysis, described in Chapter 7 'Results - Power Prediction in Sailfish'.

Table 5.1: Rudder Model Coefficient Fit Results.

Designs		Lift Coefficients				Drag Coefficients			Interaction Coeff.	
B/T	Skeg	C7	C8	C9	dCL/dAlpha	C10	C11	CD (at α: 3°)	C3	C12
2.0	None	1.52	1.88	3.98	1.63	4.02	0.68	0.022	0.06	1.32
2.8	None	1.54	1.48	2.47	1.79	4.05	0.77	0.024	-0.08	1.31
4.4	None	1.60	1.81	3.51	1.79	4.02	0.77	0.024	-0.17	1.28
2.0	Long	1.50	1.70	3.57	1.58	3.39	0.49	0.024	0.70	1.50
2.8	Long	1.49	1.85	3.71	1.66	3.63	0.56	0.023	0.46	1.38
4.4	Long	1.44	1.87	3.42	1.74	3.74	0.69	0.023	0.17	1.31

6

Results - Anti-drift Fin

Throughout this report, aspect ratio was repeatedly mentioned when discussing the performance of various lifting surfaces. Indeed, the trend that higher aspect ratios lead to better performance was found in that the skeg generates lift more effectively than changes in the hull form, and the rudder in turn more effectively than the skeg. Based on this, looking at a dedicated high-aspect ratio device to generate lift to counter the sailing forces is a promising concept.

In this chapter, the results from the anti-drift fin will be analyzed. Ultimately, the best performance is expected from an active device that can change its angle of attack and is retractable. The evaluation of such a device requires equilibrium calculations and will be picked up in the following chapter, Chapter 7 'Results - Power Prediction in Sailfish'. In this chapter, the results coming from the CFD calculations are interpreted, namely the results from Batch #3.

6.1. Anti-drift Fin Forces
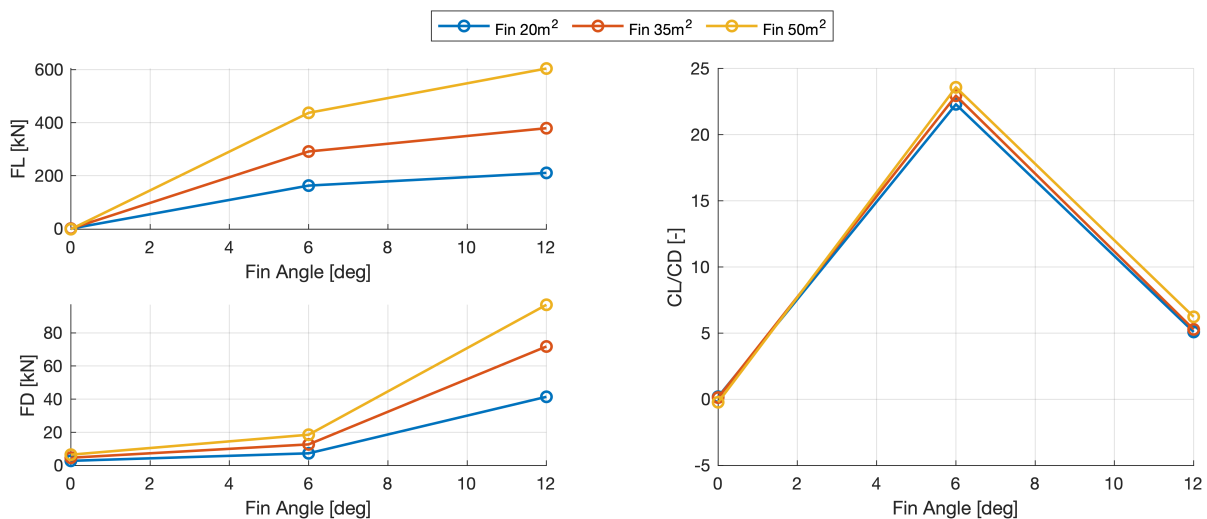
Figure 6.1: Lift, drag and lift-over-drag of different anti-drift fins. (v_s: $12kn$)

Figure 6.1 shows the lift and drag forces for varying fin sizes and angles. The drag was found to scale directly proportionally to the area, which makes sense since the overall geometry is identical, only sized up under a constant $AR = 3$. The lift increases slightly more, which explains the slight increase in lift-to-drag ratio visible for the larger fins, which deviates by around 5% between designs. A reason for this could be that for the larger fins, less fractional area is influenced by the disturbed flow around the hull.

Comparing the lift-to-drag ratio of the fin to that of the skeg and the hull, it is clear that the fin can yield

much better performance. For comparison, the best hull reached a lift-to-drag ratio of 2.5, the skeg of 9, while the fin is reaching a ratio of 24.

As such, a passive fin can already be expected to be beneficial for some operational conditions. An active angle-of-attack fin would allow optimal lift-to-drag ratios for all drift angles, and a retractable fin would fix the issue of resistance penalties for unfavorable wind conditions.

6.2. Model Coefficients Fit

To arrive at these results, accurate interpolation of the results and correct quantification of the interaction effects is necessary. To be compatible with Sailfish, the same coefficients as for the rudder fit are used, treating the fin as a rudder outside of the propeller wake.

For the anti-drift fin, no calculations under drift were conducted to limit the computational expense. This was done since hull-to-fin interaction was expected to be minimal since the fins were placed along the parallel midbody of the ship, and on the centerline. To confirm this, Figures 6.2 and 6.3 show the flow orientation under the ship at 6° of drift.
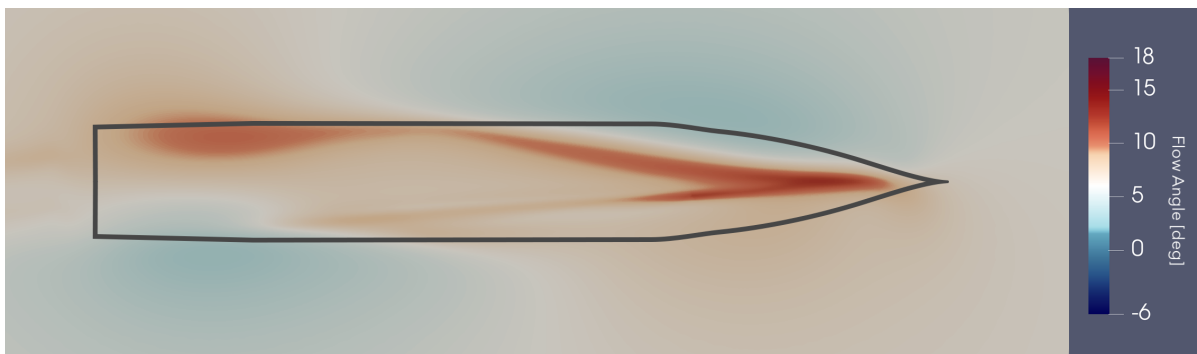
Figure 6.2: Flow direction 1m below the hull, at a 6° drift angle.
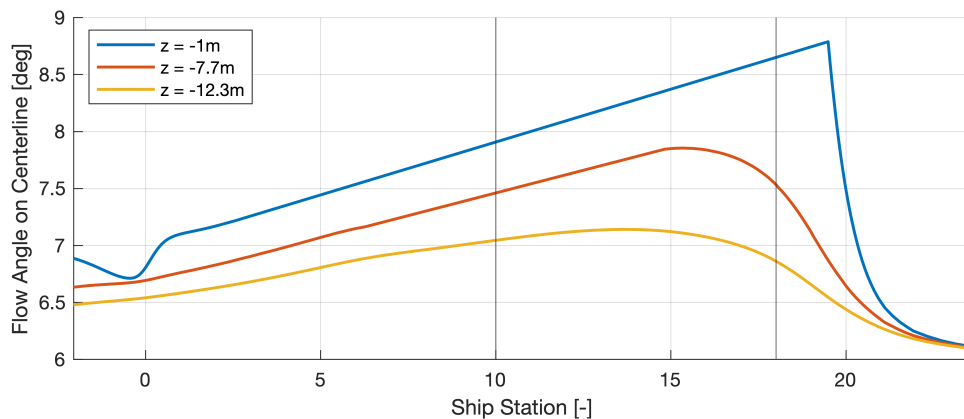
Figure 6.3: Flow direction below the hull, on the centerline, at a 6° drift angle.

Some variation is visible, but the effect is generally weakest on the centerline, which is where the fin is placed. The strongest variations are around the bow and the aft. Figure 6.3 plots the variation at different depths along the centerline. Depths -7.7m and -12.3m represent the geometric centers of the small and large fin, respectively. The positions of the fin at stations 10 and 18 are annotated. It can be seen that for both, the difference in effective angle is only between 1° and 1.5°. This is acceptable, considering such deviations in the calculation of rudder straightening coefficients only led to minimal correction factors. In comparison, deviations reached up to 15° in comparison for the rudder.

Table 6.1 shows the fitting results for the various anti-drift fins. Looking at the lift, the resulting coefficients are quite similar. The lift is slightly better for larger fin areas, as already shown earlier when looking at the forces. The lift is also marginally better for fins at midship compared to positions towards the bow. The form drag (C_{10}) is almost identical, and the Oswald efficiency (C_{11}) varies slightly, being higher for the larger fins. The Oswald efficiency overall is relatively low, but could be improved through a better fin geometry, with a better lift distribution. For this stage in the design process, these specifics are not critical. Ultimately, the differences in lift and drag are important to factor in but will likely not play a significant role in the evaluation. It can be seen that the nonlinear drag component C_{11} only plays a very minor role at the most frequently encountered fin angle of 6°. The drag coefficient is almost unaffected by the variations of C_{11}. The fin's size significantly impacts the total forces, and the position of the fin has big implications on the moment. As a result, the exact coefficient variations only play a minor role.

Lastly, the interaction coefficient C_{12} shows how much the fin alters the pressure distribution on the hull. This factor is significant, showing how important it is to calculate the fin forces in combination with the hull. The factor indicates that for some designs, almost half of the force comes from the induced pressure distribution on the hull. The fin positioned at station 18 especially shows a strong interaction effect. Again, as the size increases, the relative interaction effects decrease.

Table 6.1: Anti-Drift Fin Model Coefficient Fit Results.

Designs		Lift Coefficients				Drag Coefficients			Int. Coeff.
Area [m^2]	Station	C7	C8	C9	dCL/dAlpha	C10	C11	CD (at α: 6°)	C12
20	10	1.42	1.72	3.59	2.93	1.25	0.29	0.031	1.36
20	18	1.36	1.63	3.49	2.76	1.24	0.27	0.031	1.88
35	10	1.34	1.53	2.41	3.01	1.25	0.33	0.031	1.36
35	18	1.37	1.64	3.46	2.79	1.25	0.29	0.029	1.73
50	10	1.49	1.53	2.05	3.30	1.26	0.37	0.029	1.35
50	18	1.40	1.76	3.54	3.00	1.27	0.35	0.028	1.66

6.3. Forces and Moments on the Ship

This section uses the forces and moments on the ship under drift, with the forces of the fin included through the model defined above. The reference ship is the design with B/T 2.8 and no deadrise.
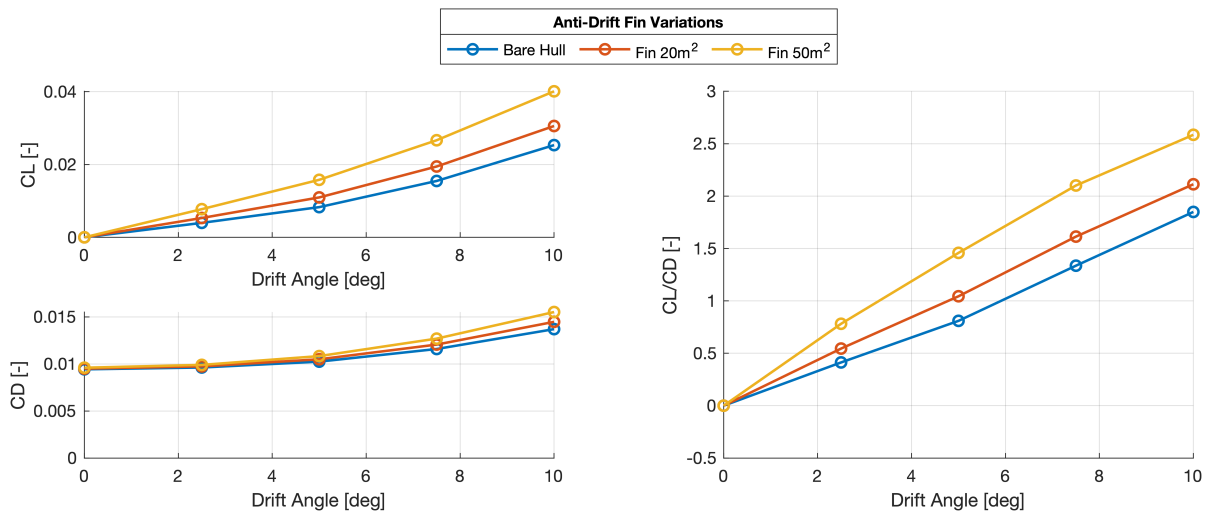
Figure 6.4: Lift, drag and lift-over-drag coefficients for ships with different anti-drift fins.

Figure 6.4 shows lift and drag coefficients for the unappended and appended cases. The results look promising at first sight, with a significant increase in the lift coefficient of the ship but only minimal resistance penalty (1% for the small fin, 2% for the large fin). As a result, the lift-to-drag curve also shows a clear improvement. Important to note is also that the improvements already set in at low degrees of drift, i.e. unlike the changes in lift through altering the B/T ratio.

Even at 2.5°, the fin already generates sufficient lift to impact the overall lift generation of the hull.
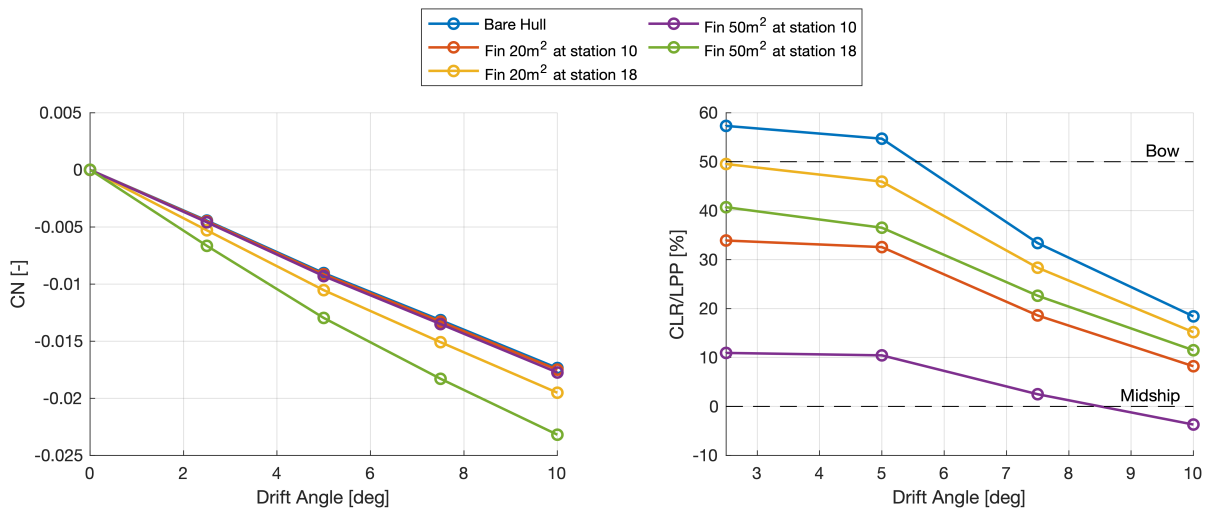
Figure 6.5: Moment coefficient and non-dimensional CLR for different fin configurations.

The position of the fin influences the resulting moment; this is shown in Figure 6.5. As expected, the fin positioned at the bow produces a larger moment. As a result, the fin positioned at midship does a better job at reducing the CLR, with the large fin reducing the CLR to almost midship. This can be very beneficial, as having a CLR fall close to the CE of the sails, which is at midship, improves the trim so that less rudder action is needed during sailing, and the ship has better maneuverability. These aspects will become apparent in the comparison in Sailfish in the next chapter. Still, the preliminary performance of a static fin can already be compared to that of the skeg and the bare hull.
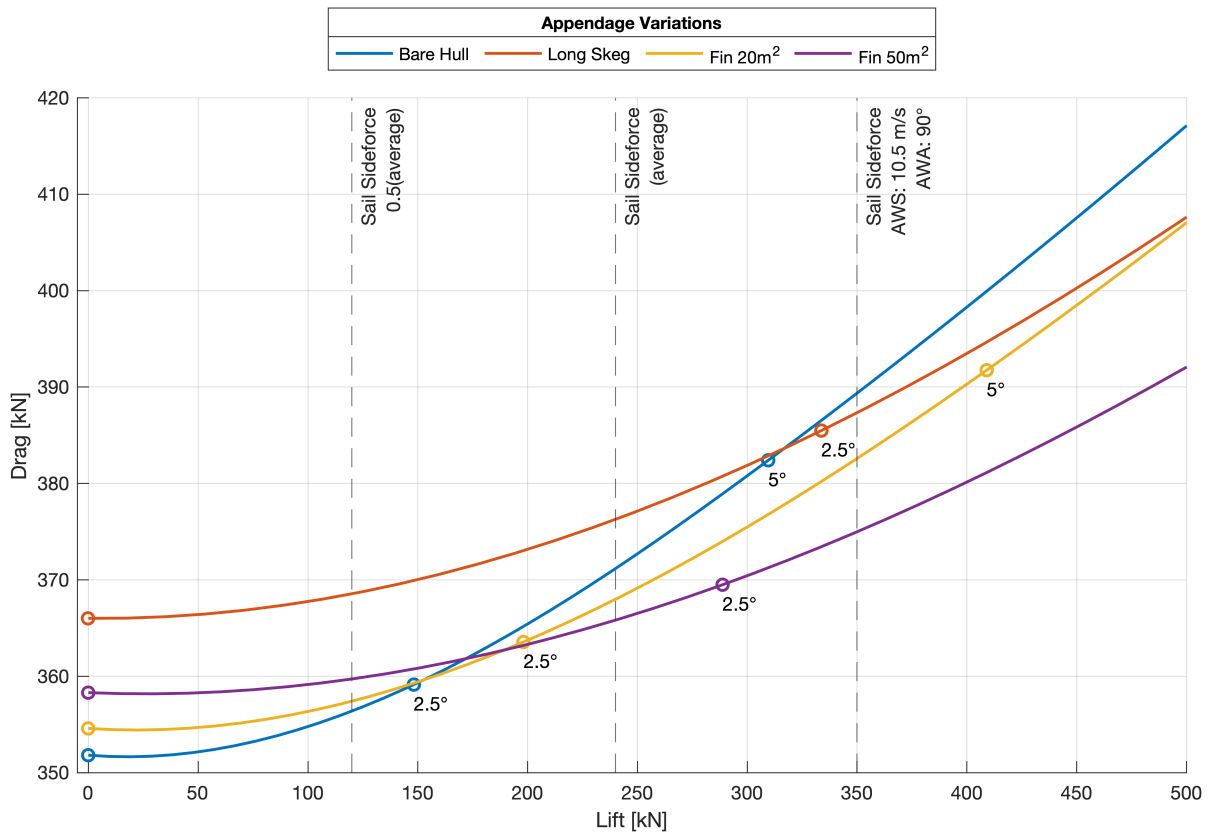
Figure 6.6: Effective performance of fixed anti-drift fins for side force generation. (v_s: $12kn$)

Figure 6.6 shows this comparison. This is an updated version of Figure 4.9, now including the fins. Compared to the skeg, the fins become more beneficial than the bare hull much earlier, at around 150-180kN, as opposed to the skeg, which requires 320kN of lift to be effective. This means that statistically, there will be many more conditions in which the fin reduces the ship's drag instead of adding to it. Also, comparing the skeg to the fin, it can be seen that the skeg is never more effective than the fin. As such, from a purely hydrodynamic point of view, adding a fin is always better than adding a skeg.

The trade-off between the fins and the bare hull is then whether the resistance penalty below 150/180kN is more significant than the resistance decrease above those thresholds. The statistically most encountered side force is in the regime where the fins are more beneficial, so even a non-retractable fin can likely lead to some performance increase. For a retractable fin, it is clear that the performance would increase, as the trade-off of resistance penalty below 150/180kN would be eliminated.

The analysis in Sailfish will provide more insight in this regard. It will also show the difference between incorporating the small fin as opposed to the large fin and how much more effective the appendage becomes if it functions with an active angle of attack. At the moment, the fin appears to operate at angles around 2.5° most of the time. The earlier analysis showed how the fin has a much higher effectiveness at higher angles, around 6°.

7

Results - Power Prediction in Sailfish

In the previous chapter, conclusions were drawn only based on the hydrodynamic forces on the hull under various drift angles. While this sort of analysis gives insight into the flow around the ship, it is not definitive in evaluating the performance of a design when it comes to the operation of a wind-assisted ship. There, much more variables come into play, such as the equilibrium between the rudder and hull, the forces on the sails, the overall propulsive system, and the weather conditions. These factors are incorporated in Sailfish. This allows an integrated approach to evaluating the designs, allowing the comparison of designs based on their expected emissions during operation.

Sailfish analyzes a ship's performance for a large range of wind speeds and angles. As such, it is most convenient to represent the results in polar plots. An important note is that some wind conditions are much more likely than others and, therefore, have a much more significant effect on the final output than others. Since this is not apparent right away from polar diagrams, Figure 7.1 shows the wind statistics associated with the MEPC.1/Circ.896 dataset, which is the reference for computing the emissions in this step because of its broad applicability as part of the EEDI/EEXI performance indicators [101]. It was also found to be reasonably close to the wind conditions encountered in typical cruising routes, as explained in Section 3.8.2 'Wind Statistics'.
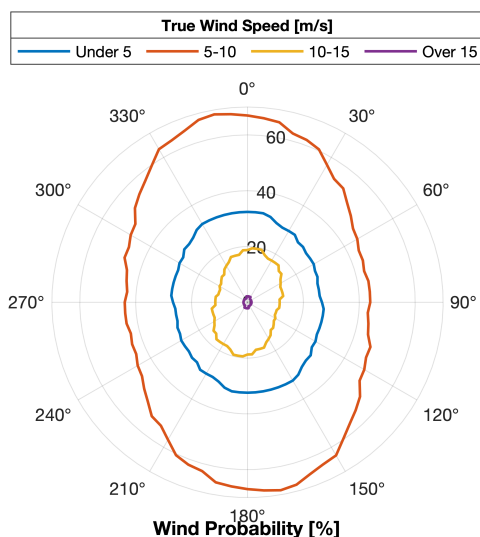
Figure 7.1: Polar plot of the wind probability statistics, from the MEPC.1/Circ.896 dataset.

The wind is usually in the 5-10m/s range, skewed towards head- and quarterly winds. This is because trade routes run east-west more often than north-south. Lower wind speeds also occur relatively frequently, around a third of the time, while wind speeds higher than 10m/s and especially 15m/s are quite unlikely. Therefore, these have a small statistical impact on the final emission results.

7.1. Bare Hull Variations

In Chapter 4 'Results - Hull Design Variations', the hull design was varied by changing the B/T ratio of the ship and by introducing a deadrise angle. It was found that the deadrise does not significantly affect the lift generation, while a more slender ship (so lower B/T ratio) is hydrodynamically favorable. Whether this translates to emissions savings was calculated using Sailfish, with the results shown in Figure 7.2.
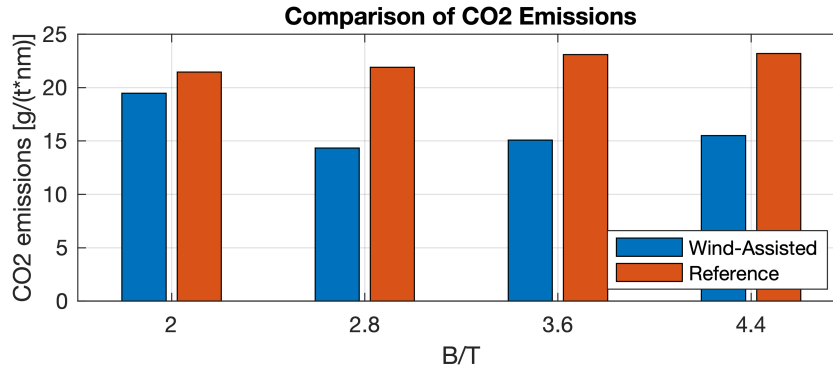
Figure 7.2: Emissions for ships with different B/T ratios.

As expected, the general trend of the results is that the performance of ships increases as they get narrower, confirming the results obtained previously. This trend is visible for both the reference case and the case with wind-assist. This is because the more slender ship not only produces more lift but also reduces the resistance, which also benefits the vessel without wind-assisted operation.

The exception that can be noted is for B/T 2.0, where the benefit of the wind-assisted ship almost completely disappears. While the emissions of the reference ship are still slightly lower compared to the B/T 2.8 case, the wind-assisted version stops having any significant benefit. This is a characteristic that is not expected based on the previously analyzed hydrodynamic factors, so the source of the deviation has to come from an operational aspect considered in Sailfish. It was found that the reason for the deviation is due to the reduced stability of the vessel at lower B/T ratios.
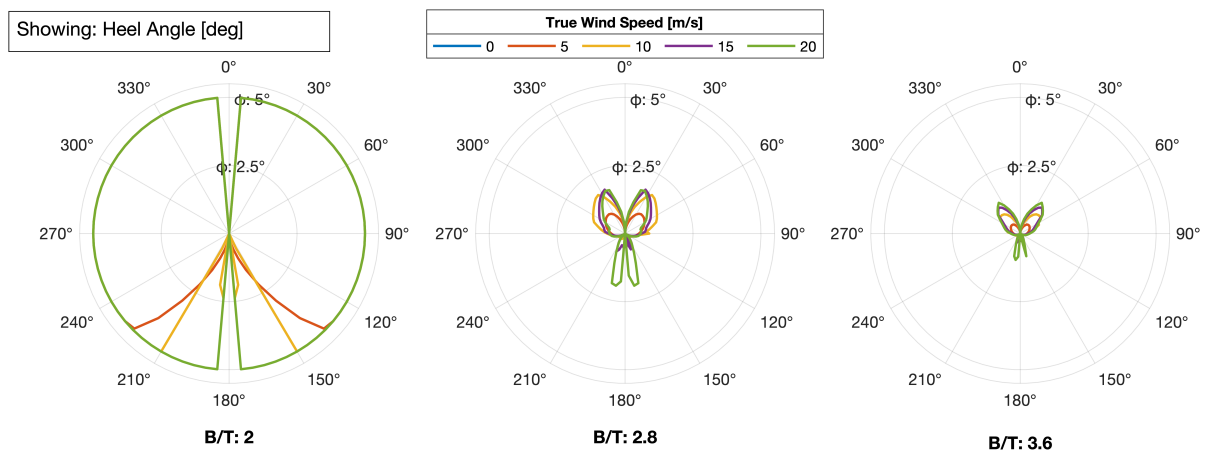
Figure 7.3: Polar plot of the heel angle for various wind conditions for ships with different B/T ratios.

Figure 7.3 shows polar plots of the heel angle for three B/T variations. The wider ships have good stability under sailing conditions, only reaching 1-2° of heel. The B/T 2.0 ship, on the other hand, completely maximizes the heel constraint set at 5°. This means the sails have to be reefed.

The sails are reefed to some extent for all wind speeds. Above 15m/s, the full power of the sails cannot be harnessed for any wind direction. Below 15m/s, the operation is still restricted to wind directions between 130° and 230°. With the early reefing, emissions are barely reduced because of the limited usage of the sails.

The effect is confirmed when looking at the hydrostatic stability of the three vessel designs, shown in Table 7.1. The slender ship is less stable because of its higher center of buoyancy and center of gravity. The metacentric height of the most slender ship is only 1.13. Increasing the B/T to just 2.8, it becomes almost 6. This difference greatly impacts the heeling of the ship under sails, as the B/T 2.8 case has no issues with extreme heel angles at all. The trade-off between stability and performance is clear, and the optimum probably lies somewhere in-between the two cases. A B/T ratio of 2.8 was chosen as the most reasonable option for further analysis.

Table 7.1: Hydrostatic stability for different B/T ratios.

B/T [-]	BM [m]	KB [m]	KG [m]	GM [m]
2.0	5.83	6.60	11.3	1.13
2.8	8.00	5.58	7.72	5.86
3.6	12.6	5.30	6.02	11.9
4.4	15.8	4.46	3.78	16.4

7.2. Passive Appendages

Adding additional lifting surfaces to the ship hull may improve its performance. The categorization as a 'passive' appendage denotes that there is no control strategy associated with any of the appendages; they are neither retractable nor can their orientation be altered during operation.

7.2.1. Optimal Skeg Configuration

Figure 7.4 shows the emissions for each skeg and B/T ratio combination. As before, the emissions refer to the aggregate emissions based on the ship traveling at 12kn, and the MEPC.1/Circ.896 wind statistics. The B/T 2.8 ships perform the best because of the stability aspects described before. As for the skeg, the trends are consistent for the B/T 2.8 and 3.6 cases. The long skeg performs best, followed by the bare hull. The short skeg performs the worst. In part, this matches the hydrodynamic analysis. There, it was found that the short skeg is never favorable compared to the long skeg. Indeed, apart from the B/T 2.0 case, which is not really worth considering due to the stability issues, the short skeg always performs worse.

The difference is that in the hydrodynamic analysis, it was concluded that it is implausible that the introduction of the skeg is worthwhile since the range of conditions for which the skeg is a resistance penalty, as opposed to a beneficial addition, is dominant. The range of conditions for which the skeg is hydrodynamically favorable was too small. Therefore, it was expected that the introduction of the skeg would increase the emissions. However, the Sailfish results show that the skeg performs similarly, even slightly better than the unappended hull. For the B/T 2.8 case, adding the long skeg leads to the best performance, even if the difference is so slight that it certainly falls within the uncertainty of the result. However, even the fact that the skeg is not significantly worse is surprising and will be analyzed further in Section 7.2.3 'Skeg and Fin Comparison'.

Emissions [g/(t*nm)]

	2.0	2.8	3.6	4.4
No Skeg	19.47	14.33	15.08	15.50
Short Skeg	20.40	14.51	15.13	15.62
Long Skeg	20.79	14.27	14.87	15.56

B/T Ratio [-]

Figure 7.4: Emissions for wind-assisted ships with different B/T ratios and skeg configurations.

7.2.2. Optimal Fin Configuration

Based on theoretical and computational groundwork, the fin is expected to perform much better than the skeg because it is a much more effective lifting surface, thanks to its high aspect ratio. As such, it can generate much more lift at a smaller drag penalty. Looking at the results from various fin configurations, shown in Figure 7.5, only modest emissions improvements are noted. Based on the hydrodynamic findings, the fin is supposed to outperform the skeg considerably. However, looking at the emissions, the savings are small and comparable to the ones of the skeg. The larger fins perform better, matching the CFD comparison's expectations.

The comparison between the fin positioned at midship (position 10) and the bow (position 18) gives a first insight into why Sailfish's operational results do not fully reflect the expectations from the hydrodynamic analysis. The fin positioned at midship performs much better, while the fin at the bow does not work and actually leads to a worse performance than even the unappended hull. This indicates that the root of the differences in the results stems from the yaw (moment) balance, not the sideforce balance.

No matter where they are positioned, the fins produce roughly the same lift but very different moments. This also matches the deviations found for the skeg. The skeg, which exceeded expectations in terms of performance, is positioned the furthest back out of all appendages and, therefore, has the most significant impact on moving the center of lateral resistance (CLR) of the hull back. This was shown previously in Chapter 4 'Results - Hull Design Variations' in Figure 4.7, and then later for the fin in Chapter 6 'Results - Anti-drift Fin' in Figure 6.5. This indicates that the appendage's role of reducing the moment of the ship might be just as important as generating additional lift.
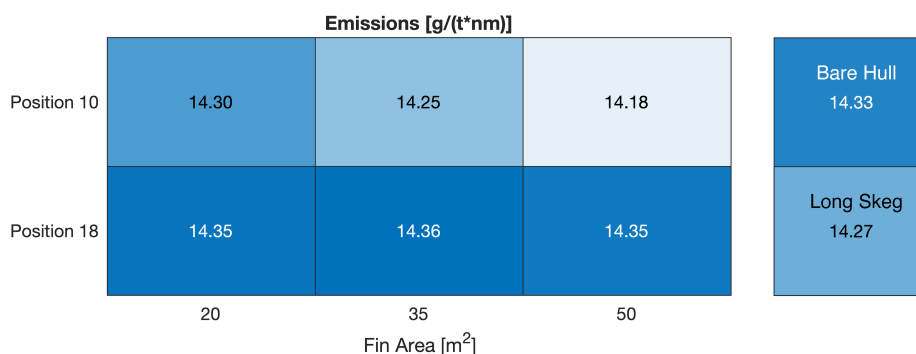
Figure 7.5: Emissions for wind-assisted ships with different passive fin configurations.

7.2.3. Skeg and Fin Comparison

Figure 7.6 shows the emissions for the different appendages for a range of wind conditions. At high wind speeds a trend of decreasing performance in wind directions between 60° and 90° can be noted through symmetric spikes in emissions for the bare hull and slightly for the passive fin as well. This also appears in the fuel savings shown in Figure 7.6, where the fuel savings drop significantly for the bare hull between 60° and 90°.

The fuel savings clearly show how the ship using the long skeg can sail much closer to the wind. The bare hull performance drops to 50% at wind angles of ±40°. With the fin, this is delayed to ±30°. The ship with skeg still reaches over 80% fuel savings at that same heading.

Clear losses occur in the upwind conditions - the ship is out of trim. In these cases, there is a large moment is on the ship, and both the bare hull and fin configurations struggle to achieve equilibrium without reefing the sails. This is confirmed in Figure 7.8, in which the rudder angle is plotted.

For both the bare hull and the passive fin cases, the rudder angle reaches its constraint of 15° in upwind headings. Even at 10m/s, the operation of the rudder is limited in wind directions between 35° and 70°. For high wind speeds, this occurs over almost the full range of wind directions. The long skeg ensures moment equilibrium without reaching the rudder constraint for any wind condition.

As soon as the rudder hits 15°, equilibrium can only be ensured by reefing sails, reducing the potential savings. The limit on the rudder angle is imposed to safeguard the ship's maneuverability while sailing.

While the fin is the superior performing appendage in theory, its position at midship is still too far forward to achieve the moment reduction of the skeg.
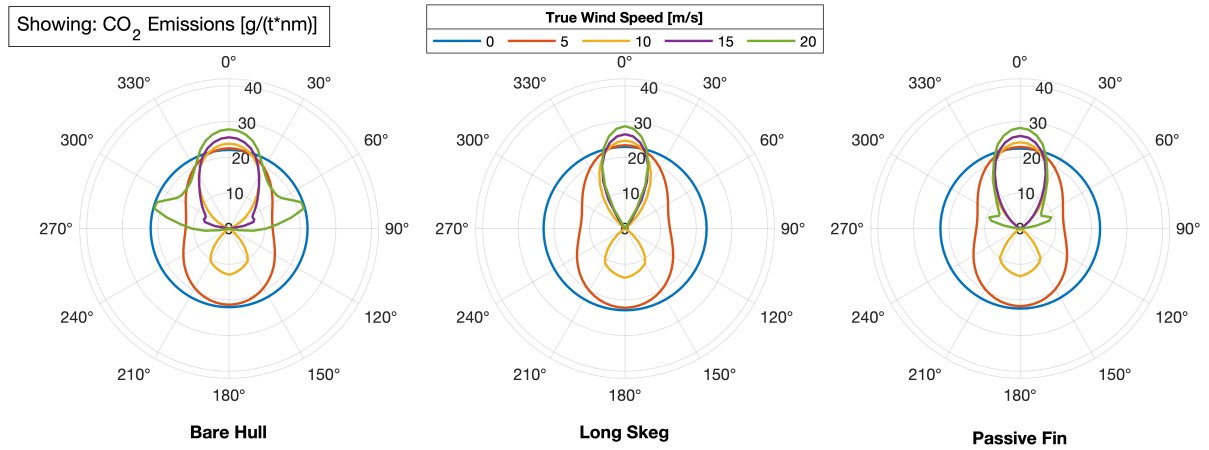
Figure 7.6: Polar plot of the CO2 emissions, for various wind conditions and appendages.
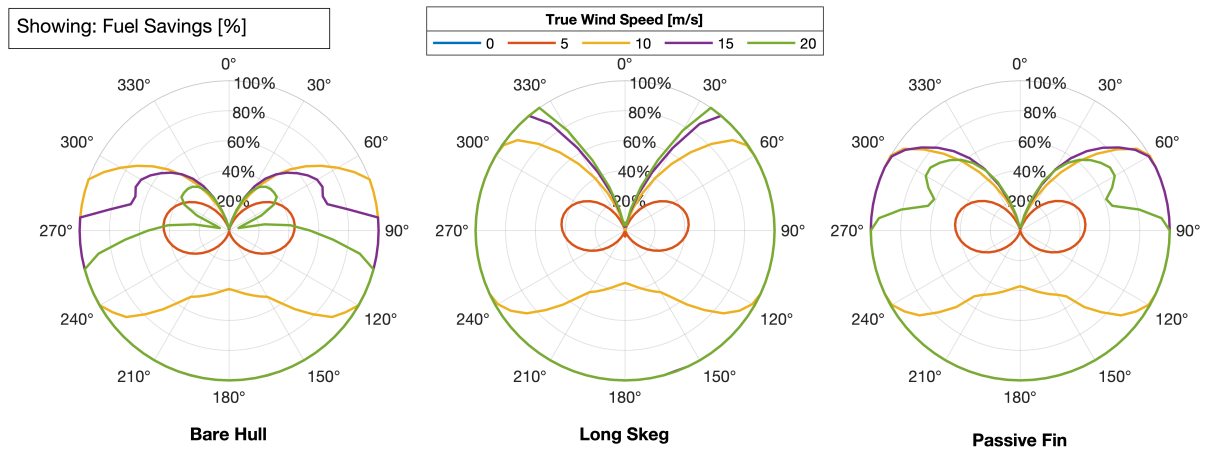
Figure 7.7: Polar plot of the fuel savings for various wind conditions and appendages.
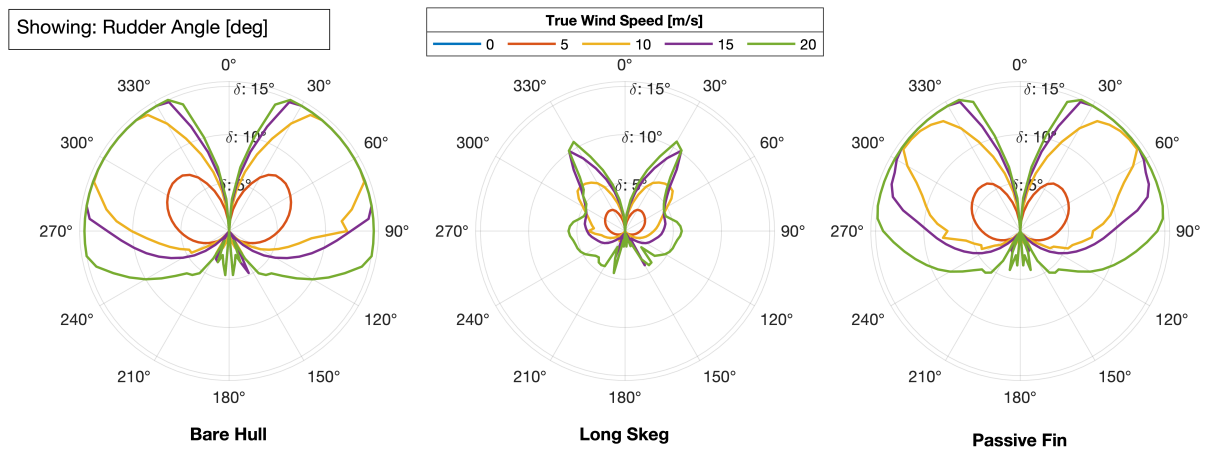
Figure 7.8: Polar plot of the rudder angle for various wind conditions and appendages.

7.3. Active Appendages

Adding control functionality to the fin is expected to improve its performance. Two aspects will be introduced. Making the fin retractable eliminates the resistance penalty in unfavorable conditions for sailing. Then, by allowing the fin to change its angle of attack, the effectiveness of the lift generation is improved since the fin can reach higher angles with respect to the flow. Figure 7.9 shows the emissions for the same set of fins configurations as before, but this time with different added control functionality.
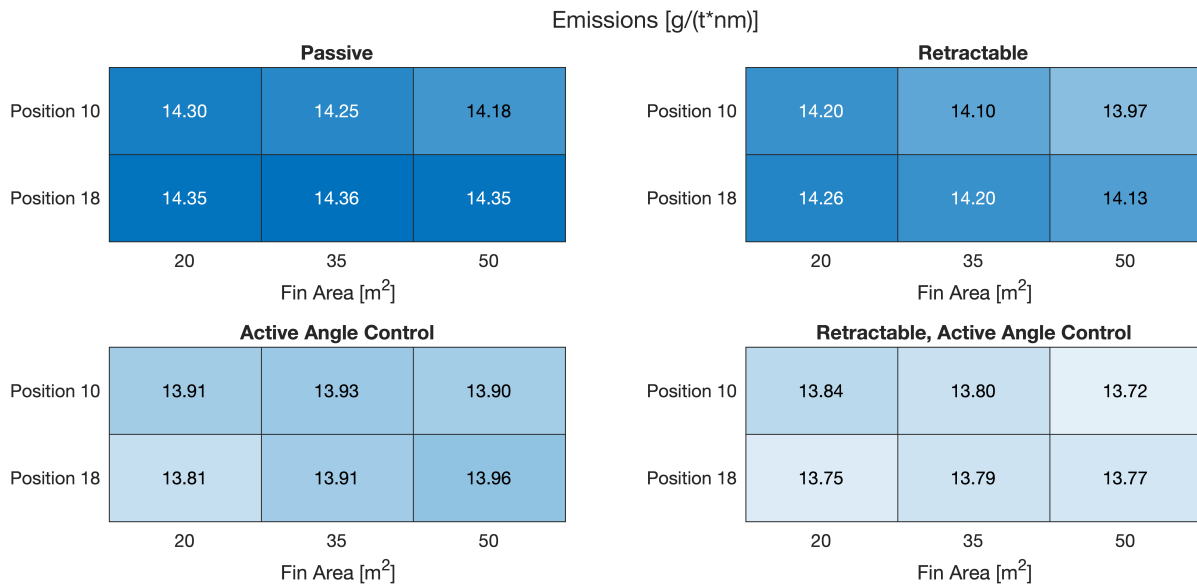
Figure 7.9: Comparison of emissions for wind-assisted ships with different anti-drift fin configurations and different levels of control

Compared to the passive fin, introducing retractability reduced emissions further by 1.5%. There is a constant reduction for all designs, but the largest fin positioned at midship remains the ideal option.

Introducing the active angle of attack has a larger effect, reducing emissions by 2.7% with respect to the passive fin. Again, all designs see an improvement, but this time, the smallest fins improve the most. The lift generation is much higher now, so even the small fins provide ample sideforce and moment reduction; the smallest fin, having the lowest resistance, is best.

The combined functionality leads to a combined positive effect, now reducing emissions by 3.4%. The largest fin is best again, as the resistance penalty in poor conditions is eliminated through retractability. Overall, the results here are very similar between designs, so the choice of including the appendage is much more important than the exact dimensions, as all fin variations lead to similar emissions reductions. Still, the largest fin positioned at midship, with retractability and active angle-of-attack, is selected for now as the ideal solution.

7.4. Overall Optimal Design

Based on the extensive analysis of hydrodynamic and operational aspects, the best design can be chosen out of the three computational batches. Table 7.2 lists the chosen optimal design parameters.

A B/T ratio of 2.8 was maintained from the reference case, as it was the best trade-off between stability and performance. A lower B/T ratio increases emissions due to large heeling angles, and a higher B/T ratio increases emissions due to increased resistance and decreased lift production. Introducing a deadrise was not found to notably improve the ship's hydrodynamic performance.

With active control, the fin is the most efficient appendage for increasing lift generation and providing yaw moment equilibrium. The $50m^2$ fin, at midship, performs best in both aspects.

Table 7.2: Set of optimal input design parameters for the wind-assisted cruise ship design.

Design Parameter	Value	Unit
B/T Ratio	2.8	[-]
Deadrise	0	[deg]
Appendage	Fin	[-]
Fin Area	50	[m^2]
Fin Position (Station)	10	[-]
Retractable Fin?	Yes	[-]
Active Angle Control?	Yes	[-]

Table 7.3: Sailfish performance indicators for the optimal design, compared to the unappended reference ship.

Property	Ref.		Opt.	Unit
Operational Speed	12	→	12	[kn]
Drift Angle (Average)	1.6	→	1.3	[deg]
Drift Angle (P95)	4.8	→	3.8	[deg]
Rudder Angle (Average)	4.8	→	2.5	[deg]
Rudder Angle (P95)	15	→	6.8	[deg]
Heel Angle (Average)	0.5	→	0.6	[deg]
Heel Angle (P95)	1.5	→	1.8	[deg]
Fraction Fin Deployed	-		43	[%]
Fraction Reefed	14.6	→	12.1	[%]
Fraction Fully Sailing	8.8	→	12.1	[%]
Relative Fuel Savings	-		2.8	[%]
Total Fuel Savings	34.5	→	**37.3**	[%]

Table 7.3 shows several performance indicators derived from the calculations in Sailfish. Looking at the constraints first, it can be seen that the optimal design reduces the drift angle of the ship. P95 denotes the 95th percentile, so the value that 95% of cases fall below of. In this case, the value refers to the drift angle that is not exceeded 95% of the time. This value was reduced by a full degree in the optimal design. While an indication of better hydrodynamic performance, sailing under less drift is also beneficial in secondary objectives such as seakeeping and overall maneuverability.

The rudder angle is considerably lower - on average, it is only half as large. This also improves safety considerations, as the ship retains better turning ability throughout the sailing conditions. The extreme cases are reduced especially, from the P95 reaching the rigid constraint of 15°, to only 6.8° in the optimal design. This also means that the earlier issues on the position of the fin being sub-optimal for moment generation is rectified now. This is because when active angle control was introduced, the forces that the fin generates increased, and therefore its impact on the CLR also increased.

The heel angle increases slightly because the optimized ship can sail in more critical conditions and support higher sail forces. Still, thanks to the choice of B/T ratio of 2.8, the ship can support these forces without heeling by more than 1.8° in the extreme, and 0.6° on average.

Figure 7.10 shows how the rudder never reaches the 15° limit, as well as the contribution of the fin angle. The fluctuations in the data are due to the cross-talk between fin and rudder angle in cases where multiple angle configurations lead to similar results. Since this only happens when the difference between the cases is slight either way, this does not really affect the emissions.

Compared to the reference ship, the optimized ship spends almost 40% more time entirely propelled by the sails. Also, 43% of the time, the fin is deployed, so a very even balance is struck for when the fin is beneficial and when it is not. The fin deployment is also shown in Figure 7.10. It shows that the fin is especially useful for upwind courses, where it becomes beneficial even at very low wind speeds. Because the moment on the ship is highest for these courses, the fin can considerably aid the ship's balance there.

The fraction of time in which the sails are reefed is equal to the time the ship is entirely wind-propelled. This means that reefing of the sails never occurs due to operational constraints, but only due to surplus power. This was not the case for the reference ship, where nearly 6% of time, the ship had to reef early because of limitations imposed on the rudder angle.

In total, adding the active fin results in additional fuel savings of 2.8%, leading to a total fuel saving of 37.3% when compared to a bare hull version without sails.
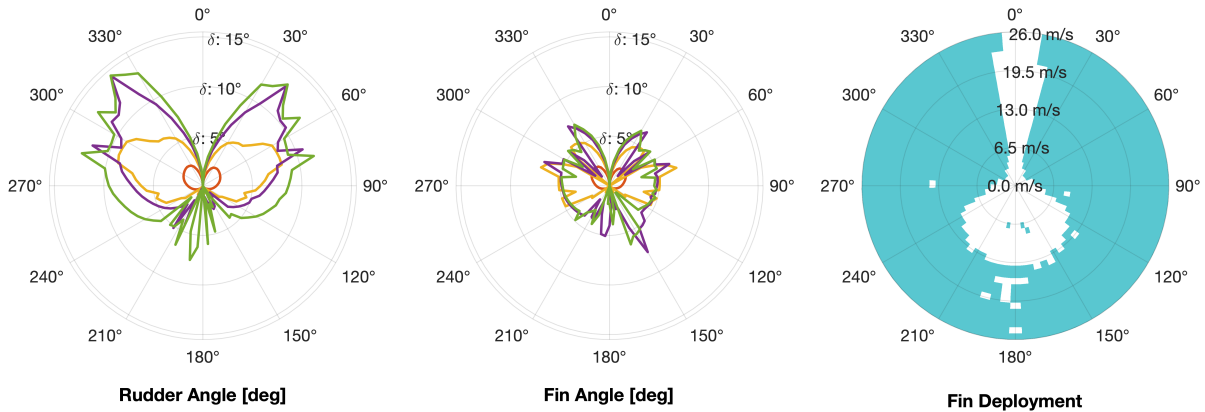
Figure 7.10: Polar plots of the rudder angle, anti-drift fin angle, and deployment for the optimal design configuration.
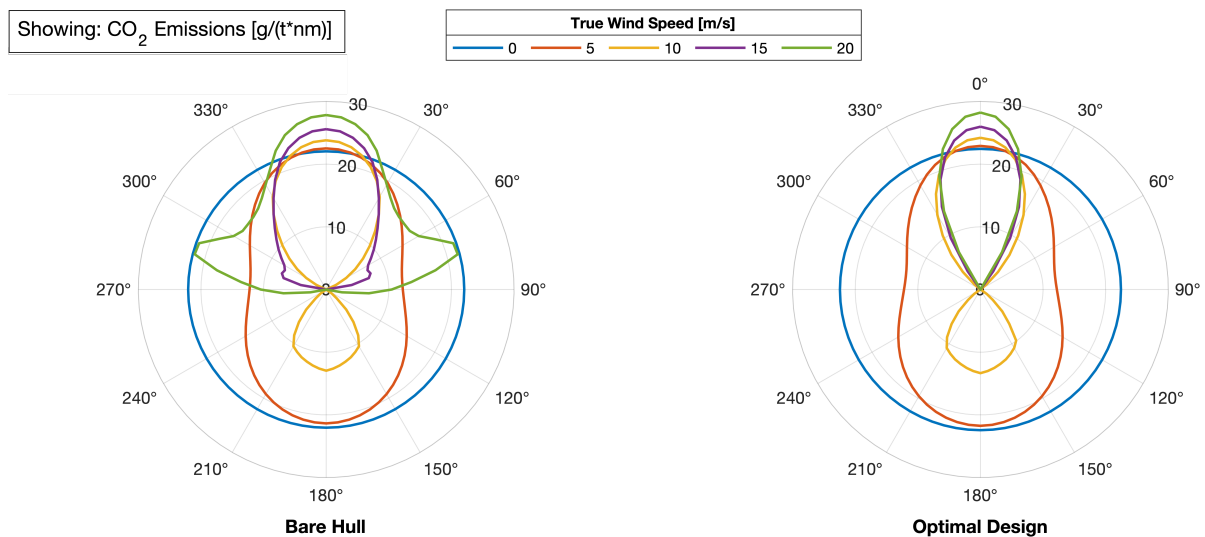
Figure 7.11: Polar plot of the ship emissions for the reference and optimal design.

Figures 7.11 and 7.12 show the emissions and fuel savings for the final design, compared to the un-appended reference case. The most significant reduction in emissions is in upwind courses. While the reference ship barely sees savings when sailing upwind, the optimized ship is fully sailing for a course up to 55° at 10m/s and up to 35° at 20m/s of wind speed. At these very high wind speeds, the reference ship can barely keep operating, actually needing just as much or even more engine power than it would at lower wind speeds. This is only the case for the optimized ship when sailing with a direct ±15° headwind.
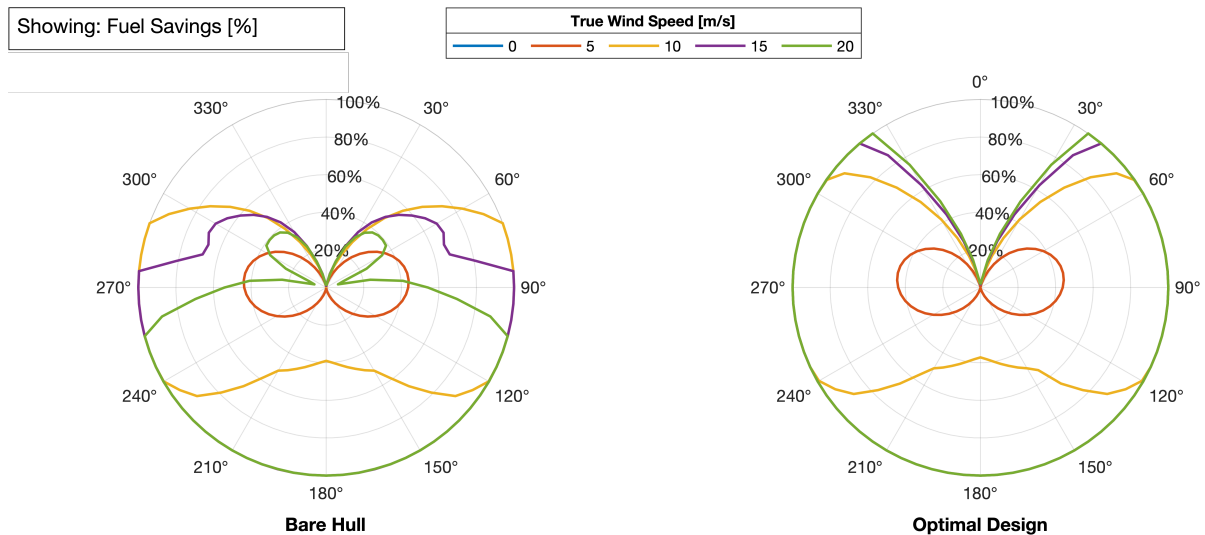
Figure 7.12: Polar plot of the fuel savings for the reference and optimal design.

7.5. Operational Variations and Sensitivity

The design of a wind-assisted ship is a complex, multidisciplinary problem involving many parameters and conditions. This is reflected in some steps of the methodology of this project. Only through the inclusion of aerodynamic data (see Section 3.7) and operational and supplementary data (see Section 3.8) it was possible to compute the PPP and come to conclusions on the expected emissions.

While this study is heavily focused on the hydrodynamic aspects, the large influence that some of the other parameters have on the final result should not be underestimated. To acknowledge this fact, this section focuses on the sensitivities and uncertainties of the overall power prediction for the wind-assisted ship.

7.5.1. Power Flow
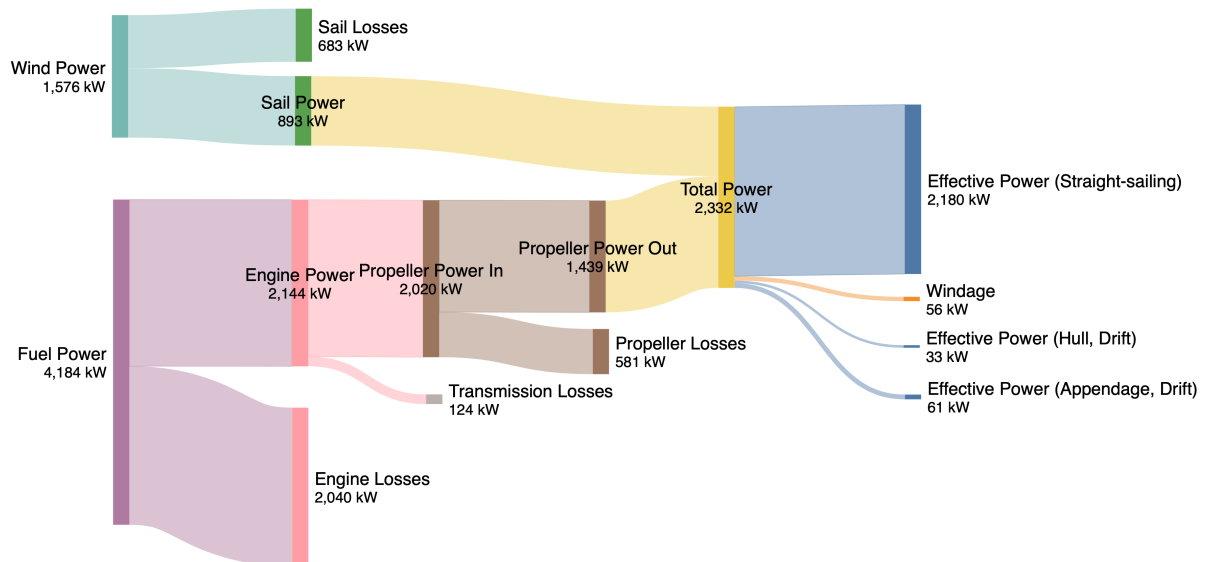
Figure 7.13: Power flow for the operation of a wind-assisted ship based on Sailfish computation.

Figure 7.13 shows the power flow for the optimal design, calculated based on the analysis in Sailfish. The power through each node was computed for each possible wind condition, and then the weighted average was calculated using the MEPC.1/Circ.896 wind statistics matrix.

This makes sure that non-linearities are respected.

The two power inputs are wind and fuel power. They are calculated according to:

$$P_{\text{wind}} = 0.5\rho A_{\text{sails}}TWS^3 \tag{7.1a}$$

$$P_{\text{fuel}} = \dot{m} \cdot LHV \tag{7.1b}$$

Neither power source can be turned into usable propulsion without experiencing some losses. For wind propulsion, the idealized sails have an overall efficiency of 57%. Including further losses, such as interaction effects between sails, will lower this fraction. Still, the efficiency is likely to stay higher than that of the conventional propulsion system, which falls around 34%. This is due to the losses in the diesel engine (49%), transmission losses (6%), and propeller losses (29%).

The effective power is split into the straight-sailing component, the windage, and the drift-induced components of hull and rudder (resulting from the drag forces introduced when sailing under drift). The drift-induced components would not be a factor for a non-wind-assisted ship. It can be seen that the overwhelming majority of power (93%) goes to overcoming the ship's straight-sailing resistance (at 12kn).

In this study, the goal is to reduce the total power by reducing the various resistance components. If the total power demand is lower, but the sail power is the same, less propeller power is needed, and therefore, less fuel is used. Thus, based on the available wind power and power demand, the conventional propulsion power train is calculated 'backward' to reach the fuel power necessary to achieve an equilibrium. The emissions are then directly based on the fuel mass flow rate, so also on the fuel power:

$$\dot{CO_2} = CF \cdot \dot{m} = CF \frac{P_{\text{fuel}}}{LHV} \tag{7.2}$$

The CO_2 performance, as a function of ship speed and capacity, is then calculated according EEDI standards:

$$CO_{2,\text{perf}} \left[g/(t \cdot nm) \right] = \frac{\dot{CO_2} \, [kg/s]}{DWT \, [t] \cdot v_s \, [kn, nm/h]} \tag{7.3}$$

The overview of the power flow through the systems already gives an initial idea of the possible sources of errors, as well as the sensitivity of some of the subsystems. If a component contributes a large amount of power, changes in its parameters can significantly affect the final output, i.e. have a large sensitivity with respect to the emission prediction.

7.5.2. Operational Variation

Until now, the analysis focused on the comparative emissions between design variations. This had the advantage that systems outside of the hydrodynamic scope did not impact the quality of the analysis since they are constant throughout the variations. However, these factors are essential to understand the overall expected fuel savings for the final wind-assisted design. To gain insight into the accuracy of the emissions estimation overall, some parameters were varied to see how sensitive the final result is to them.

The list is split into hydrodynamic and scenario parameters. The hydrodynamic parameters are more theoretical, and account for possible uncertainties in the calculations. The scenario parameters are linked to real operational factors.

Hydrodynamic parameters:
- Ship Resistance
- Ship C_L
- Ship C_N
- Rudder C_L
- Anti-drift Fin C_L

Scenario parameters:
- Ship Speed
- Sail Area
- Wind Conditions

Each parameter was varied by $\pm 20\%$. The only exception are the wind conditions. A fractional increase in sail power would lead to the same effect as increasing the sail area, so instead, the wind conditions are varied geographically, by describing the wind conditions for a less favorable and a more favorable

route with respect to the MEPC.1/Circ.896 statistics. These routes are described in Section 3.8.2 'Wind Statistics'.

The results are shown in Figure 7.14. Emissions and fuel savings are not interchangeable in this case, as some conditions (ship speed and resistance) also influence the emissions of the reference ships without wind-assisted propulsion.
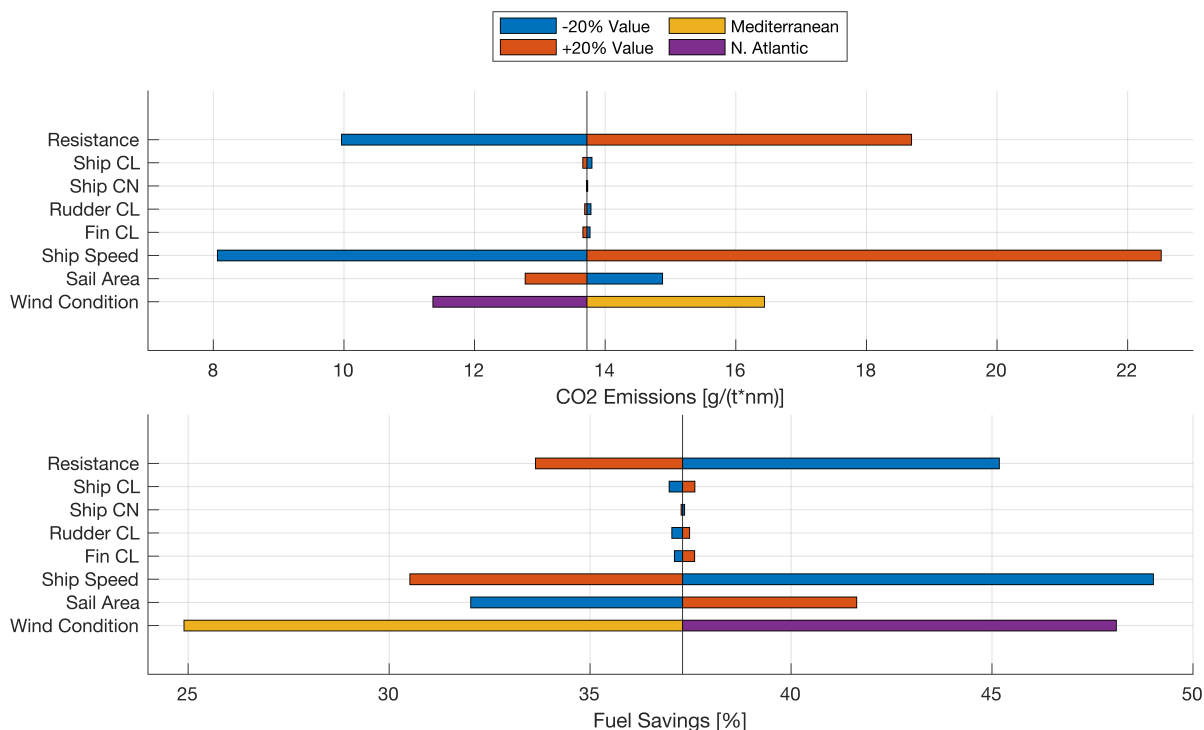
Figure 7.14: CO_2 Emissions (top) and relative fuel savings (bottom) estimation for variation of input parameters, for the optimal ship design.

Looking at the first five bars (the hydrodynamic parameters), the conclusions drawn from the power flow diagram can be confirmed. Resistance has an overwhelming influence on emissions. The effect is much more significant than changing the lift or moment coefficients. Increasing returns are visible for resistance, as decreasing resistance improves savings more than increasing resistance reduces savings. This is because at lower resistances, the much more probable, low wind speed conditions already become beneficial for sailing and generate considerable savings.

The influence of the hull lift is much smaller, only impacting the fuel savings by $\pm0.3\%$. A higher lift leads to more efficient sailing under less drift, in turn leading to lower drag. However, since the drift-induced hull drag is much smaller than the straight-sailing resistance, the sensitivity is also much lower. For the rudder and the fin, results are similar but smaller with variations of about $\pm0.2\%$. The moment coefficient has almost no impact, altering the fuel savings by only $\pm0.05\%$. This is because when moment balance can always be maintained without reaching any constraints on the rudder or fin angle (as is the case for the optimal design), the further impact of the moment coefficient is minimal.

The operational characteristics show a more considerable impact. Reducing the ship speed by 20% (to 9.6kn) increases fuel savings the most, to 49%, which is an increase of 32%. On the other hand, increasing ship speed to 14.4kn does not lead to as much of a penalty but still reduces savings to just more than 30%. The parameter behaves similarly to the resistance since they are closely correlated.

The sail area also has a significant impact, with changing the sail area by $\pm20\%$ leading to either a reduction in fuel savings to 32% or an increase to 42%. Here, some diminishing returns can be noted for larger sail areas, considering the larger sails are not beneficial for conditions in which the sails are already reefed.

Lastly, altering the wind conditions to different routes targets the same power source as changing the sail area. Table 7.4 shows how the wind power differs for each region.

Table 7.4: Available wind power for different routes.

Route	Wind Power	Rel. Difference
Mediterranean	836 kW	-47%
MEPC.1/Circ.896	1576 kW	0
North Atlantic	2643 kW	+68%

Out of the investigated parameters, the fuel savings of the ship are most dependent on the wind conditions. In the North Atlantic, the optimal ship design could achieve 48% of fuel savings through wind-assisted propulsion without any other modifications. The same ship sailing in the Mediterranean would only be able to reduce its fuel savings by 25%.

7.5.3. Variable Speed Operation
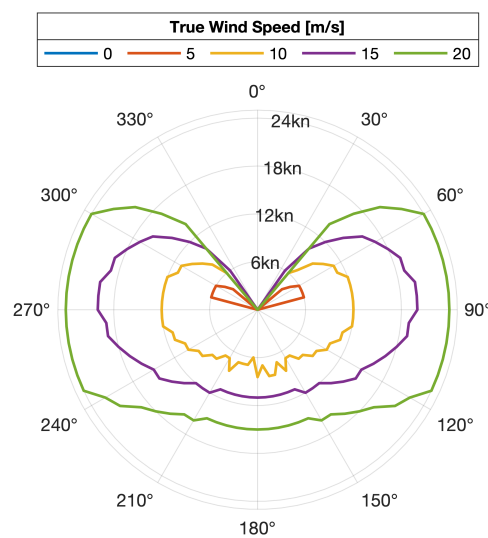
Figure 7.15: Velocity prediction program (VPP) for optimal ship design.

There are a range of conditions for which there is surplus wind power available that is not used, because the ship already reached its operational speed of 12kn. For the MEPC.1/Circ.896 conditions, this happens 12% of the time. For the North Atlantic conditions, it occurs 23% of the time. Harnessing this power surplus can happen in two ways - through the integration a regenerator mode for the propeller (see Section 2.3.5 'Regeneration') or by allowing an increased ship speed. The implementation of a regenerator is complex and results would either have very high uncertainty, or require more complex coupled ship-propeller simulations. The analysis of a variable speed operation is therefore more sensible to quantify potential additional savings in this study.

A VPP, shown in Figure 7.15 was constructed by running Sailfish for a range of operational speeds, and for each condition finding the lowest speed for which emissions are zero, i.e. the ship is sailing. For wind speeds above 10m/s, a wide range of courses allow a speed much higher than the operational speed of 12kn. At 20m/s, this is the case for all courses outside ±40°. The maximum speed is 24kn, as that is the highest operational speed that was computed in Sailfish.

To quantify the benefit of sailing faster, the ship speed in less favorable conditions was reduced slightly, to the point that the average ship speed is again equal to 12kn. Instead of having to optimize the ship speed for hundreds of conditions, i.e. hundreds of variables, the problem was simplified into reducing the ship speed to a certain 'slow' operational speed for all conditions under a certain wind power threshold. The optimization was set up as a two-variable, nonlinear constraint problem. The two variables are the reduced ship speed, and the threshold for the wind conditions in which the ship speed should be reduced. For conditions in which the ship can sail faster than 12kn, the ship speed is

taken from the VPP, but limited to a maximum 20kn to account for possible other operational concerns. The nonlinear constraint is an equality constraint that ensures the average ship speed remains 12kn. The problem was solved using `fmincon` in Matlab.

For the MEPC.1/Circ.896 conditions, savings increased from 37.3% to 40.2% after the optimization. This is achieved by slightly lowering the ship speed to 11.6kn in sub-optimal conditions. Over the range of conditions, the average speed remains 12kn.

For the North Atlantic conditions, savings increased from 48% to 56.7%. The optimal solution involved lowering the ship speed to 10.6kn in poor conditions. The increased sailing speed in better conditions makes up for this.

(a) MEPC.1/Circ.896 Conditions. **(b)** North Atlantic Conditions.
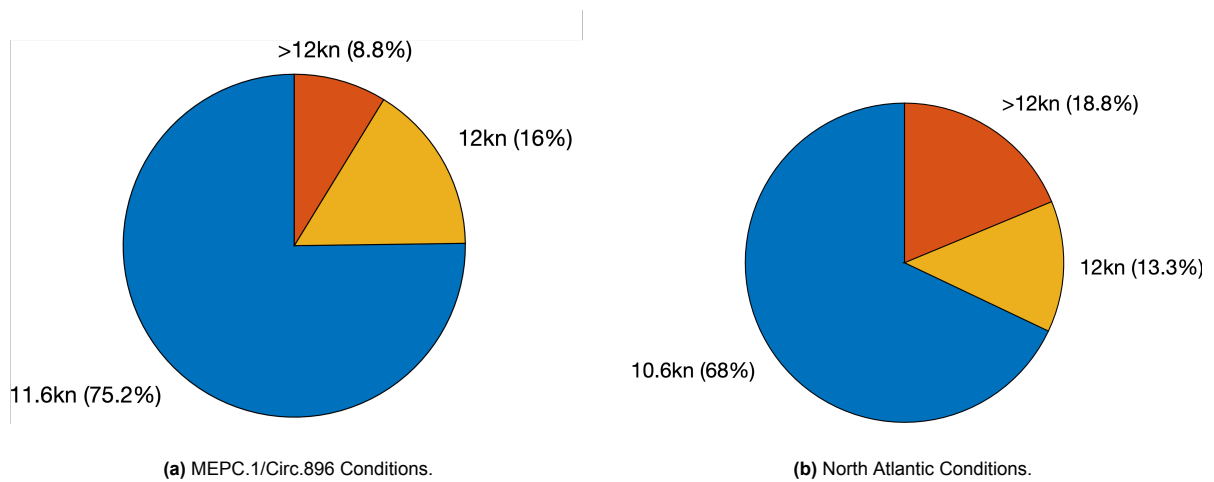
Figure 7.16: Variable speed operation in different conditions. Increased ship speed reaches 20kn, average speed is 12kn.

While complete flexibility in ship speed might not always be possible due to scheduling considerations, the fact that even a slight variation in ship speed depending on the wind conditions can have a significant impact on the fuel savings shows there can be a benefit to an adaptive ship speed strategy.

8
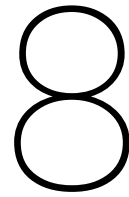
Conclusions

This research aimed to determine how the hydrodynamic design of a wind-assisted cruise ship aiming for 50% fuel savings can be optimized. Clear hydrodynamic findings gave insight into the optimal design and associated trade-offs. An expanded performance investigation revealed operational conditions that strongly impact the quantification of fuel savings in the context of wind-assisted propulsion.

8.1. Hydrodynamic Investigation

The hydrodynamic investigation focused on two aspects. The modification of the hull form, and the analysis of appendages.

For the hull form, the B/T ratio showed a clear trade-off between stability and performance. Slender hulls show improved lift-to-drag ratios. This is mainly due to a significant reduction in resistance at zero drift. For the MARIN Ferry, the vortex generation at the bow indicated the increased lift production of slender hulls. These effects are considerable, but due to their non-linear nature, they only scale in magnitude at higher drift angles, which well-trimmed, optimized designs generally do not reach. The heel limit on the ship sets a hard constraint on the slenderness of the hull. For the MARIN Ferry, this limit lies between B/T 2.0 and 2.8. Slender hulls also have a slight moment penalty. From a design perspective, this is less significant. The slightly worse moment balance can be restored, while an otherwise significantly increased resistance or a lack of stability cannot be recovered easily.

The deadrise angle showed no significant impact on the lift production of the hull. There is some improved performance through a reduction in drag. However, this purely stems from reduced transom resistance due to better pressure recovery at the aftship. These improvements are not expected to carry over into the real world, due to the added resistance through the increased dynamic trim and associated sinkage of the aft.

When using the lift-to-drag ratio as a performance indicator, the skeg performs significantly worse than a high-aspect-ratio fin. The resistance of the skeg is more than three times as large as the one of the fin, while the lift is comparable in magnitude. However, from a moment balance perspective, the skeg outperforms a fin positioned at midship, due to its lower yaw moment coefficient, and the associated reduction of the CLR. The skeg shifts the CLR from 8m ahead of the bow to almost midship.

The semi-empirical approach using the Holtrop&Mennen resistance estimation and SURSIM maneuvering models was not found suitable for the hydrodynamic evaluation of designs. The resistance estimation with H&M is accurate, matching the CFD results within a 2% margin. The drag coefficient estimation in SURSIM is acceptable, at least error margins are smaller than the differences between designs. However, the most critical parameter is the lift coefficient. Lift in SURSIM was found to be over-predicted by a factor of 2 with respect to the CFD results. Also, relative differences between designs and trends as a function of drift angle are not consistent with the CFD results. This is likely caused by the highly non-linear nature of the lift generation. SURSIM is designed for maneuvering

87

applications, which deal with a much broader (full) range of drift angles. This results in a mismatch, as for sailing, accuracy in the drift angles between 0° and 5° is most important.

Additional attention was given to the interactions of rudders/fins with the hull. It was essential to consider the rudder-hull interaction, accounting for up to one-third of the total rudder lift force. Hull-rudder (flow straightening) effects were found to be highly dependent on the distance between rudders, and the skeg design. The strongest straightening effects are found for slender ships with long skegs. Overall rudder performance differed by up to 40% between designs. The fin-hull interactions were found to be even more important to consider, with almost half of the force from the fin resulting from the induced pressure by the fin on the hull. Straightening effects on the fin are negligible.

8.2. Operational Performance Investigation

The operational analysis conducted in Sailfish allowed for the integrated evaluation, which was found to be crucial based on the literature review and reference designs. The benefit of more advanced design variations through actively controlled appendages can also only be quantified in an operational analysis.

The optimal bare hull design reaches savings of **34.5%**. No operational constraints due to heel are encountered; the heeling angle always stays below 2.5°, which is well below the set limit of 5°. The main drawbacks of the bare hull design are the operational constraints due to insufficient yaw balance severely limit sailing performance in upwind courses.

The optimal passively appended design reaches savings of **34.9%**, achieved with a fin positioned at midship. Yaw balance in all conditions is still not achieved with this configuration, so moving the fin back further would unlock some additional savings.

Introducing active retractability and angle-of-attack control strategies to the fin increases savings to **37.3%**. Retractability limits the resistance penalty in unfavorable conditions, and thanks to the higher angle of attack, full yaw balance is achieved now as well. The two control strategies are found to complement each other well.

Wind conditions have a large effect on the potential fuel savings. The results of the design optimizations are gauged based on the MEPC.1/Circ.896 guidelines. A comparison with typical cruising routes revealed a strong sensitivity with respect to fuel savings. The MEPC.1 guidelines are comparable to typical cruises in the Caribbean. A more favorable route is the Holland America Line North Atlantic itinerary. On this route, fuel savings would reach **48%**. On the contrary, the MSC Opera East Mediterranean itinerary would only result in 25% savings.

Fuel savings were also found to be limited through a lack of strategy in conditions with surplus wind power. Adapting the sailing strategy based on variable speed optimization (between 10.6 and 20kn) increased savings to **40.2%** (+2.9%) for the MEPC.1/Circ.896 conditions, and to **56.7%** (+8.7%) for N. Atlantic conditions.

The goal of a cruise ship going beyond 50% fuel savings through wind-assisted propulsion is feasible, but only through optimal appendage design, and the integration of operational considerations, which are highly dependent on wind conditions, ship speed, and possibly the recoupment of energy in favorable wind conditions.

9

Discussion and Recommendations

9.1. Discussion

The limitations of this study are related to the uncertainties associated with the results. The following simplifications are made in this study, sorted in ascending order of expected impact on the final results.

Additional interaction effects of the anti-drift fin

Flow straightening effects for the anti-drift fin have been assumed to be negligible. This is because the flow angle on the centerline and along the parallel midbody of the ship varies much less than at the aftship. Based on relative differences in flow angle, the straightening effect of the fins is expected to be less than one-third of that of the rudders.

Should cases be investigated in which the fin is positioned further aft (as would be optimal for a passive fin configuration), flow straightening and even fin-propeller/rudder interactions may become relevant.

Propeller interaction effects

The propeller was not included in the CFD computations, which neglects the effect of the drift angle on the propeller performance. Due to drift, the wake field in the propeller plane will change, and asymmetries between the two propulsors are introduced. Generally, the mean axial and pre-swirl wake fractions increase with drift angle, but vortices shed from the hull can significantly influence specific drift conditions. Based on calculations of a similar case of a twin-screw ship under drift, the impact on the propulsive efficiency is expected around 1-2% [104].

The rudder lift curve is also dependent on the propeller thrust, especially for higher rudder angles. Under drift, the interaction between the rudder and propeller is also considerable and might alter the wake fraction at the rudder. The same goes for the swirl of the rudder inflow. Effects of varying self-propulsion points in wind-assisted conditions add further complexity to the description of all these effects.

Wave-making and wave-added resistance

The ship resistance has a major impact on the emissions. In this study, wave-making resistance is neglected through the usage of double-body simulations. However, since the operational speed is relatively low ($Fr = 0.14$), these effects are expected to be minimal as viscous resistance components are dominant.

More important remains the wave-added resistance. When estimating the emissions by integrating operational conditions such as wind statistics on specific routes, other environmental factors like wave-response should also be considered. This becomes especially relevant considering the correlation between high wind speeds and wave height. Waves will increase overall fuel emissions through increased resistance, but may also reduce the relative fuel savings, as shown in the sensitivity study.

Sail force estimation and interaction effects

Accurate information on the lift generation of the Solid Sails used for Silenseas was not available for this research, so approximations had to be made. This limits the fidelity of the sail forces, therefore introducing uncertainty with respect to fuel savings. Most notably, interaction effects between sails are not considered, which are expected to lower their overall performance. Accurate modeling of sail interactions, especially between three sails, still relies on complex numerical models.

9.2. Recommendations

Specific to the investigated design case, some of the aforementioned limitations could be addressed in future studies to improve the prediction accuracy. This includes including the propeller in the CFD analysis, implementing a more accurate version of the sail forces, computing wave-added resistance components, and further optimizing the fin geometry, for example by improving the lift distribution on the fin to lower the induced drag.

Beyond the specifics of this case study, two main directions for future research are identified.

Expanding on the appendage design for wind-assisted ships

SURSIM does not have the precision to estimate the lift force at small drift angles accurately enough for a design optimization. While this may speak for an improved semi-empirical modeling approach for optimizing ship hulls under drift, the results from this study, in combination with the analyzed literature, favor a different approach.

Appendages, especially active appendages, have a considerable effect on the hydrodynamic performance of the hull. This includes the anti-drift fins, but also the rudders. From a broader design perspective, it appears that the more efficient the appendage design, the more the optimal ship hull approaches the ideal straight-sailing design again. It is therefore seen as a viable strategy to optimize the hull for minimal straight-sailing resistance, and the appendages for side force/moment balance under drift.

Wing theory provides the underlying reason for this; high aspect ratio lifting surfaces outperform lower aspect ratio surfaces. Also, hull optimization has the fundamental limitation of having to be optimal for the aggregate of all conditions. Active appendages can be optimized individually per condition.

A detailed optimization of appendages (rudders, fins) in terms of geometry, sizing, positioning, and control strategy is proposed. This can include interaction effects with the hull and propellers, as well as possible multi-fidelity approaches, as also suggested by Kramer and Steen [64], and Giovannetti [51].

Quantitative analysis of the recovery of surplus wind power

Operating the ship at a variable speed depending on wind conditions had a major impact on the total fuel savings. This is because a significant amount of wind power goes unused in favorable conditions. Making the ship speed a function of the wind conditions may not always be possible due to scheduling concerns of the cruise ship operator.

Regeneration is a competing solution. It recovers the same surplus energy as variable speed operation, also activating when the wind conditions are more favorable than sailing at the design speed requires.

It would be interesting to explore how the savings from the two methods compare. On system level, regeneration is limited by propeller efficiency, and possible additional mechanical and electrical losses. The savings in variable speed operation are limited by the increased resistance, scaling with the square of the ship speed.

Investigating the potential savings associated with a regenerator integrated into a wind-assisted cruise ship has the potential to reveal significant additional savings. Based on the results from the variable speed optimization, these additional savings are expected in the range of 2-8%.

References

[1] W. Laas, *Die grossen Segelschiffe: Ihre Entwickelung und Zukunft*, 1st ed. Berlin, Heidelberg: Springer Berlin, Heidelberg, 1908, pp. VIII, 127, Springer Book Archive.

[2] F. Thies and K. Fakiolas, "Wind propulsion," in *Sustainable Energy Systems on Ships*, Elsevier, 2022, pp. 353–402.

[3] J. Gerritsma, R. Onnink, and A. Versluis, "Geometry, Resistance and Stability of the Delft Systematic Yacht Hull Series," *International Shipbuilding Process*, vol. 28, no. 328, 1981.

[4] B. R. Clayton, "Wind-assisted ship propulsion," *Physics in Technology*, vol. 18, no. 53, 1987.

[5] G. J. Van Burgeler, "Fuel saving through wind energy. The Flettner rotor.," *Blauwe Wimpel*, vol. 41, 1986.

[6] G. W. Schaefer and K. Allsopp, "Kite-sails for wind-assisted ship propulsion.," 1981.

[7] W. M. S. Bradbury, "Large Sailing Ships - A Fluid Dynamic Investigation," Tech. Rep., 1983.

[8] J.-L. Armand and P. Marol, "Aerodynamics of Sail-Assisted Propulsion of Commercial Ships : A Preliminary Study," Tech. Rep.

[9] L. Bergeson and C. K. Greenwald, "Sail Assist Developments 1979-1985," *Journal of Wind Engineering and Industrial Aerodynamics*, vol. 19, pp. 45–114, 1985.

[10] E. Crowdy, "The Economics of Sail," in *Symposium on Wind Propulsion of Commercial Ships*, The Royal Institution of Naval Architects, RINA, 1980.

[11] Bain News Service, *Buckau*, 1970. [Online]. Available: `https://loc.gov/pictures/resource/ggbain.37764/`.

[12] Solar Studios, *Jamda shin aitoku maru rigid sails wind assisted tanker ship*. [Online]. Available: `http://www.change-climate.com/Transport_Land_Sea_Sustainable/Assisted_Ships_Sails_Solar_Projects_Marine_Pollution/JAMDA_Shin_Aitoku_Maru_Japan_Marine_Development_Association.htm`.

[13] P. Singer, "One Atmosphere," in S. Gardiner, Ed., Oxford University Press, 2010, ch. 10.

[14] S. Gardiner, "A Perfect Moral Storm Climate Change, Intergenerational Ethics, and the Problem of Corruption," in S. Gardiner, Ed., Oxford University Press, 2010, ch. 4.

[15] R. Heijliger, "ESG for Shipping - Anatomy of Ship Finance," *Cambridge Academy of Transport*, 2022.

[16] M. Mozuni and W. Jonas, "Rise of alternative business models in the era of expensive megaships," in 2016, pp. 55–70.

[17] International Maritime Organization, "Consideration of How To Progress the Matter of Reduction of GHG Emissions From Ships - Existing IMO activity related to reducing GHG emissions in the shipping sector," Tech. Rep., 2017.

[18] International Maritime Organization, *Rules on ship carbon intensity and rating system enter into force*, 2022. [Online]. Available: `https://www.imo.org/en/MediaCentre/PressBriefings/pages/CII-and-EEXI-entry-into-force.aspx`.

[19] F. Spinelli, S. Mancini, L. Vitiello, R. N. Bilandi, and M. De Carlini, "Shipping Decarbonization: An Overview of the Different Stern Hydrodynamic Energy Saving Devices," English, *Journal of Marine Science and Engineering*, vol. 10, no. 5, 2022.

[20] N. Gray, S. McDonagh, R. O'Shea, B. Smyth, and J. D. Murphy, "Decarbonising ships, planes and trucks: An analysis of suitable low-carbon fuels for the maritime, aviation and haulage sectors," English, *Advances in Applied Energy*, vol. 1, 2021.

[21] H. Wang, P. Zhou, and Z. Wang, "Reviews on current carbon emission reduction technologies and projects and their feasibilities on ships," English, *Journal of Marine Science and Application*, vol. 16, no. 2, pp. 129–136, 2017.

[22] "Orient Express Silenseas: The legendary train heads out to sea as the world's largest sailing ship is unveiled," *Accor*, 2023.

[23] A. Skogman, "The Practical Meaning of Lateral Balance for a Sail-Assisted Research Vessel," *Journal of Wind Engineering and Industrial Aerodynamics*, vol. 20, pp. 201–226, 1985.

[24] P. K. Kundu, I. M. Cohen, and D. R. Dowling, *Fluid mechanics.* 2016, vol. 6.

[25] *Atmospheric turbulences*. [Online]. Available: `https://www.ibc-aviation.com/en/the-mag/business-aviation/atmospheric-turbulences.html`.

[26] S. Hörner, *Fluid Dynamic Lift*. 1985, vol. 2.

[27] *Subsonic flow effects*. [Online]. Available: `https://history.nasa.gov/SP-367/chapt4.htm#f53`.

[28] W. B. Oswald, "General Formulas and Charts for the Calculation of Airplane Performance," U.S. Department of Commerce, Tech. Rep., 1932.

[29] G. Bordogna, "Aerodynamics of wind-assisted ships Interaction effects on the aerodynamic performance of multiple wind-propulsion systems," 2020.

[30] K. Roncin and J. M. Kobus, "Dynamic Simulation of Two Sailing Boats in Match Racing," *Sports Engineering*, vol. 7, pp. 139–152, 2004.

[31] L. Larsson, H. Raven, and J. Paulling, *Ship Resistance and Flow* (Principles of naval architecture). Society of Naval Architects and Marine Engineers, 2010.

[32] A. Papanikolaou, *Ship design: Methodologies of preliminary design*. Springer Netherlands, 2014, pp. 1–628.

[33] T. Fujiwara, G. E. Hearn, F. Kitamura, M. Ueno, and Y. Minami, "Steady sailing performance of a hybrid-sail assisted bulk carrier," *Journal of Marine Science and Technology*, vol. 10, no. 3, pp. 131–146, 2005.

[34] J. Gerritsma, J. A. Keuning, and A. Versluis, "Sailing Yacht Performance in Calm Water and in Waves," Delft University of Technology, Tech. Rep., 1993.

[35] S. Toxopeus and S. W. Lee, "Validation of slender-body method for prediction of linear manoeuvring co-efficients using experiments and viscous-flow calculations," MARIN, Delft University of Technology, Tech. Rep., 2006.

[36] J. P. Hooft, "The Cross-Flow Drag on a Maneuvering Ship," *Ocean Engineering*, vol. 21, no. 3, pp. 329–342, 1994.

[37] J. P. Hooft and F. H. H. A. Quadvlieg, "Non-linear hydrodynamic hull forces derived from segmented model tests," in *International Conference MARSIM*, A.A. Balkema, 1996, pp. 9–13.

[38] M. Drela, "XFOIL: An Analysis and Design System for Low Reynolds Number Airfoils," MIT Dept. of Aeronautics and Astronautics, Tech. Rep., 1989.

[39] J. Holtrop and G. G. J. Mennen, "An Approximate Power Prediction Method," *International Shipbuilding Progress*, vol. 29, no. 335, 1982.

[40] MARIN, *Qdesp*. [Online]. Available: `https://www.marin.nl/api/marin/downloads/get-download/5101/0/16917/block_files_7utkknkc7efz/F7G19XUswWZyJcOlxWUj_7iX5Lg=/QDESP.pdf`.

[41] S. Toxopeus, "Comparison of Manoeuvering Simulation Programs for SIMMAN Test Cases," MARIN, Tech. Rep., 2008.

[42] MARIN, *Refresco*. [Online]. Available: `https://www.marin.nl/en/facilities-and-tools/software/refresco`.

[43] J. H. Ferziger and M. Peric, *Computational Methods for Fluid Dynamics*, 3rd ed. Springer, 2002.

[44] SimScale, *What is y+ (yplus)?* 2023. [Online]. Available: `https://www.simscale.com/docs/simulation-setup/global-settings/k-omega-sst/`.

[45] J. Mourad, *What is y+ (yplus)?* 2018. [Online]. Available: `https://www.simscale.com/forum/t/what-is-y-yplus/82394`.

[46] Altair, *Near-wall modeling*, 2023. [Online]. Available: `https://help.altair.com/hwcfdsolvers/acusolve/topics/acusolve/training_manual/near_wall_modeling_r.htm`.

[47] G. D. Struijk, "Hydrodynamics of Wind-Assisted Ships A Numerical and Experimental Study on a Systematic Series of Bare Hull Models at Drift Angles," 2015.

[48] J. W. Settels, "Hydrodynamic Forces on Wind Assisted Ships using CFD," 2015.

[49] N. J. Van Der Kolk, J. A. Keuning, and R. H. Huijsmans, "Part 1: Experimental validation of a RANS-CFD methodology for the hydrodynamics of wind-assisted ships operating at leeway angles," *Ocean Engineering*, vol. 178, pp. 375–387, 2019.

[50] N. J. Van Der Kolk, I. Akkerman, J. A. Keuning, and R. H. Huijsmans, "Part 2: Simulation methodology and numerical uncertainty for RANS-CFD for the hydrodynamics of wind-assisted ships operating at leeway angles," *Ocean Engineering*, vol. 201, 2020.

[51] L. M. Giovannetti, K. Ljungqvist, and S. Werner, "Variation of Underwater Appendages and their Effects on Wind Powered Ships," in *7th High Performance Yacht Conference*, 2021.

[52] J. W. Settels, "Systematic Investigation of Hull Forces Under Influence of Wind Assisted Ship Propulsion (WASP)," MARIN, Tech. Rep., 2016.

[53] J. Schot, "ARD Flettner Driven Ship: Work Package 2 Effect of design variations on the hydrodynamic performance of a wind assisted bulk carrier Report No. 70100-2-RD," MARIN, Tech. Rep., 2022.

[54] V. Ferrari, T. Gornicz, A. Kisjes, and F. H. H. A. Quadvlieg, "Influence of Skeg on Ship Manoeuvrability at High and Low Speeds," MARIN, Tech. Rep.

[55] R. Eggers, "Design Variations for Wind Assisted Ships Report No. 70033-10-RD," MARIN, Tech. Rep., 2018.

[56] F. H. H. A. Quadvlieg, R. Tonelli, and A. Bedos, "Unified Damping Model," MARIN, Tech. Rep., 2021.

[57] T. Nikkels, "The Ecoliner Concept," in *2nd Natural Propulsion seminar*, Wageningen, 2013, pp. 1–22.

[58] A. F. Molland, *Marine Rudders and Control Surfaces*. 2007.

[59] J. Liu and R. Hekkenberg, "Sixty years of research on ship rudders: effects of design choices on rudder performance," *Ships and Offshore Structures*, vol. 12, no. 4, pp. 495–512, 2017.

[60] J. Schot, "Hydrodynamics of wind assisted vessels Effect of rudder design on the hydrodynamic losses Report No. 70100-4-RD," MARIN, Tech. Rep., 2022.

[61] Y. Minami, T. Nimura, T. Fujiwara, and M. Ueno, "Investigation into Underwater Fin Arrangement Effect on Steady Sailing Characteristics of a Sail Assisted Ship," *International Society of Offshore and Polar Engineers.*, 2003.

[62] N. J. Van Der Kolk, "Sailing Efficiency and Course Keeping Ability of Wind Assisted Ships," 2020.

[63] N. J. Van Der Kolk, I. Akkerman, J. A. Keuning, and R. H. Huijsmans, "Low-aspect ratio appendages for wind-assisted ships," *Journal of Marine Science and Technology (Japan)*, vol. 26, no. 4, pp. 1126–1143, 2021.

[64] J. V. Kramer and S. Steen, "Sail-induced resistance on a wind-powered cargo ship," *Ocean Engineering*, vol. 261, 2022.

[65] F. DeBord, "Relative Performance of Conventional Versus Movable-Ballast Racing Yachts," *The 17th Chesapeake Sailing Yacht Symposium*, 2005.

[66] *Watt and sea*. [Online]. Available: `https://www.wattandsea.com/en/`.

[67] *Swi-tec*. [Online]. Available: `https://swi-tec.com/product-category/energy/`.

[68] *Save marine*. [Online]. Available: `https://www.save-marine.com/en/home`.

[69] *Shipmotion*. [Online]. Available: `https://shipmotiongroup.com/sailyacht/controllable-pitch-propulsion/`.

[70] *Bruntons propellers*. [Online]. Available: `https://bruntonspropellers.com/cpp/`.

[71] S. Enge, E. Fjøsna, and A. Sigurbjarnarson, "Regenerative Hybrid-Electric Propulsion RENSEA, Phase 1," North Sailing, Bellona Foundation, Tech. Rep., 2013.

[72] G. Gunnarsson, J. Björn, S. Á. Sigurbjarnarson, and S. Enge, "Regenerative electric/hybrid drive train for ships RENSEA, Phase 2," North Sailing, Bellona Foundation, Tech. Rep., 2016.

[73] M. Leslie-Miller and B. Van Someren, "Foundation 0 - Hydro-generation, solar, electric and heat generation," in *27th International HISWA Symposium*, 2022.

[74] J. Huisman, "Propeller Design Review and Exploration Studies, Report No. 32992-1-POW," MARIN, Tech. Rep., 2023.

[75] J. Huisman, "Propeller Design Review, Second Design, Report No. 32992-2-POW," MARIN, Tech. Rep., 2023.

[76] M. van der Plas, "Hydro generation potential on board sailing super yachts - Dykstra Naval Architects," *TU Delft*, 2023.

[77] L. Van Heugten, "A surrogate-assisted propeller optimisation in propulsive and regenerative operations: A case study," *TU Delft*, 2023.

[78] A. Ajdin, *China rolls out its first vlcc with four rigid wing sails*, 2022. [Online]. Available: `https://splash247.com/china-rolls-out-its-first-vlcc-with-four-rigid-wing-sails/`.

[79] A. Schmidt and M. Vahs, "Entwicklung eines innovativen Schiffsantriebes gekennzeichnet durch den Einsatz von Magnus-Rotoren zur Windenergienutzung in Kombination mit einem hierauf abgestimmten Antriebspropeller," ENERCON, Tech. Rep., 2013.

[80] L. Khan, J. J. R. Macklin, C. D. Peck, O. Morton, and G. Souppez, "A review of wind-assisted ship propulsion for sustainable commercial shipping: latest developments and future stakes," in *Wind Propulsion Conference*, 2021.

[81] N. Rehmatulla, S. Parker, T. Smith, and V. Stulgis, "Wind technologies: Opportunities and barriers to a low carbon shipping industry," *Marine Policy*, vol. 75, pp. 217–226, 2017.

[82] B. Comer, C. Chen, D. Stolz, and D. Rutherford, "Rotors and bubbles: Route-based assessment of innovative technologies to reduce ship fuel consumption and emissions," ICCT, Tech. Rep., 2019.

[83] L. Blain, *Giant supertanker uses 9.8% less fuel thanks to 130-foot sails*, 2022. [Online]. Available: `https://newatlas.com/marine/new-aden-supertanker-sails/`.

[84] Econowind, *Key wind-assist propulsion installation starts north sea operations*, 2021. [Online]. Available: `https://www.econowind.nl/index.php/2020/03/02/key-wind-assist-propulsion-installation-starts-north-sea-operations/`.

[85] Ship Technology, *Norsepower fits first tiltable rotor sails on sc connector*, 2021. [Online]. Available: `https://www.ship-technology.com/news/norsepower-rotor-sails-sc-connector/#:~:text=Norsepower%5C%20noted%5C%20that%5C%20the%5C%20installation,service%5C%20speed%5C%20by%5C%20sail%5C%20alone.`.

[86] ENERCON, *Windblatt: Enercon magazine for wind energy, ausgabe 1*, 2013. [Online]. Available: `https://www.enercon.de/fileadmin/Redakteur/Medien-Portal/windblatt/pdf/en/WB_03-2013_en_web.pdf`.

[87] *Windcoop*. [Online]. Available: `https://www.wind.coop/`.

[88] *Neptune has started to build the first large sailing cargo vessel „the canopée"*, 2022. [Online]. Available: `https://www.neptunemarine.com/neptune-has-started-to-build-the-first-large-sailing-cargo-vessel-the-canopee-ever-made/`.

[89] *Neoliner 1360 - 136m ro-ro sailing cargo vessel*. [Online]. Available: `https://www.mauric.ecagroup.com/neoliner-1360`.

[90] Chantiers de l'Atlantique, *Silenseas*, 2021. [Online]. Available: `https://chantiers-atlantique.com/references/silenseas/`.

[91] *Oceanbird*, 2022. [Online]. Available: `https://www.theoceanbird.com/`.

[92] D. G. M. Watson, "Practical Ship Design," in *Ocean Engineering*, vol. 1, 1998.

[93] *Windcoop franchit un nouveau pas dans son projet de porte-conteneur*, 2022. [Online]. Available: `https://agence-api.ouest-france.fr/article/windcoop-franchit-un-nouveau-pas-dans-son-projet-de-porte-conteneur`.

[94] *Ariane group twitter*. [Online]. Available: `https://twitter.com/arianegroup/status/1532794269253115905`.

[95] R. Tonelli, "Rudder 2020 Model," MARIN, Tech. Rep., unreleased.

[96] AirfoilTools, *Airfoil tools naca0009*, 2024. [Online]. Available: `http://airfoiltools.com/airfoil/details?airfoil=n0009sm-il`.

[97] Gaspar, H. - NTNU, *Ship lab*. [Online]. Available: `http://www.shiplab.hials.org/`.

[98] SimScale, *Mesh quality*, 2022. [Online]. Available: `https://www.simscale.com/docs/simulation-setup/meshing/mesh-quality/`.

[99] Matlab, *Fmincon*, 2023. [Online]. Available: `https://nl.mathworks.com/help/optim/ug/fmincon.html`.

[100] B. Montgomerie, "Scientific report Methods for Root Effects, Tip Effects and Extending the Angle of Attack Range to ±180°, with Application to Aerodynamics for Blades on Wind Turbines and Propellers," 2004.

[101] International Maritime Organization, *Mepc.1-circ.896*. [Online]. Available: `https://wwwcdn.imo.org/localresources/en/OurWork/Environment/Documents/Air%5C%20pollution/MEPC.1-Circ.896.pdf`.

[102] MARIN, *Blue route*. [Online]. Available: `https://blueroute.application.marin.nl/`.

[103] T. Burton, N. Jenkins, D. Sharpe, and E. Bossanyi, *Wind Energy Handbook*, 2nd ed. John Wiley & Sons, 2011.

[104] J. J. A. Schot and R. Eggers, "The Effect Of Leeway Angle On The Propeller Performance," in *Wind Propulsion*, 2019.

Appendix A: Fit of MARIN Ferry Maneuvering Model

Origin of the fitted comparison maneuvering model for the MARIN Ferry used for the SURSIM validation in Section 2.2.3 'SURSIM'.
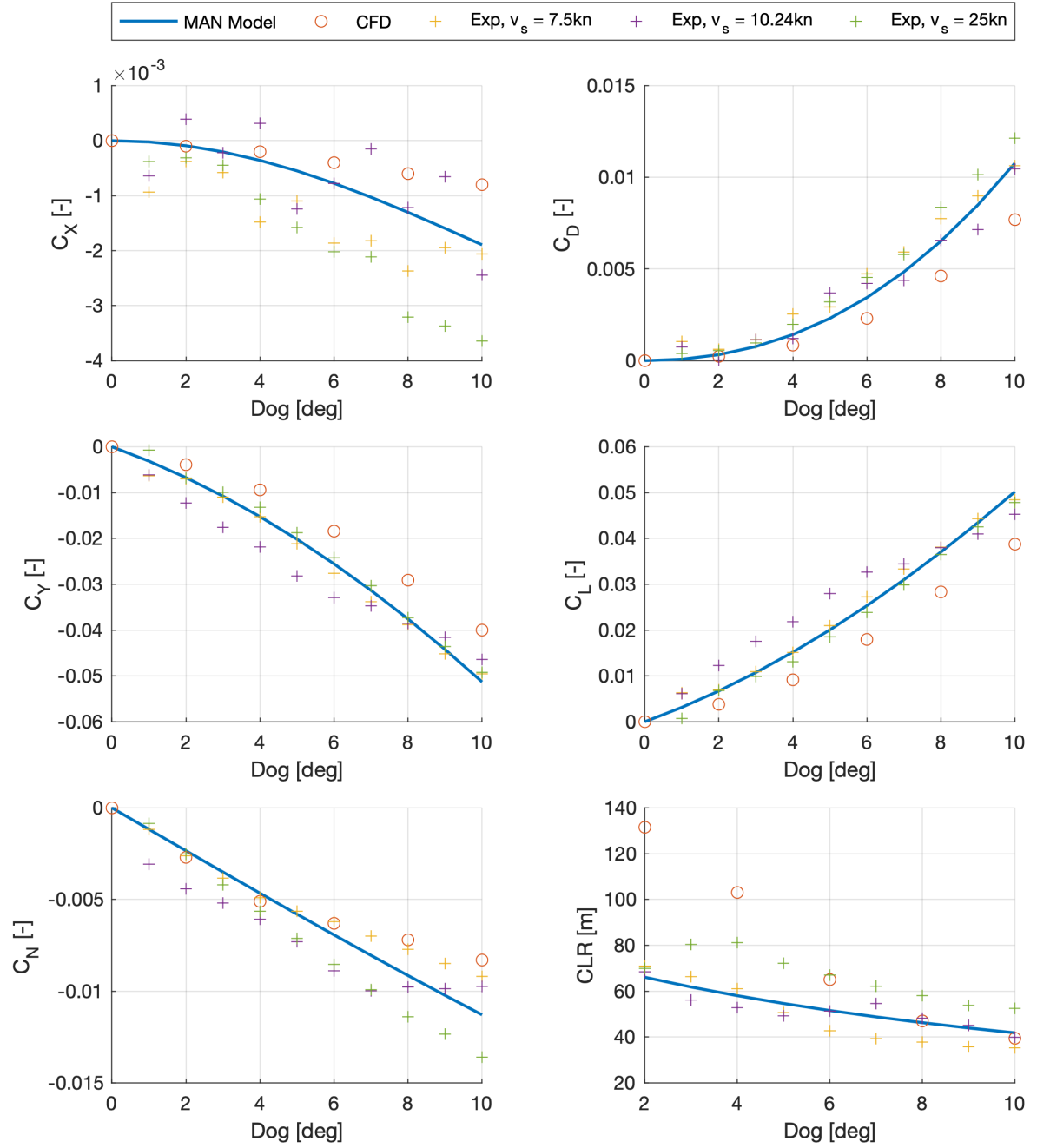
Appendix B: Comparison of Wind-Assisted and Conventional Ship Parameters

Dimensions of wind-assisted ships compared to around 900 commercial cruise and cargo ships. Reference data source: `cruisemapper.com` *and* `marinetraffic.com`
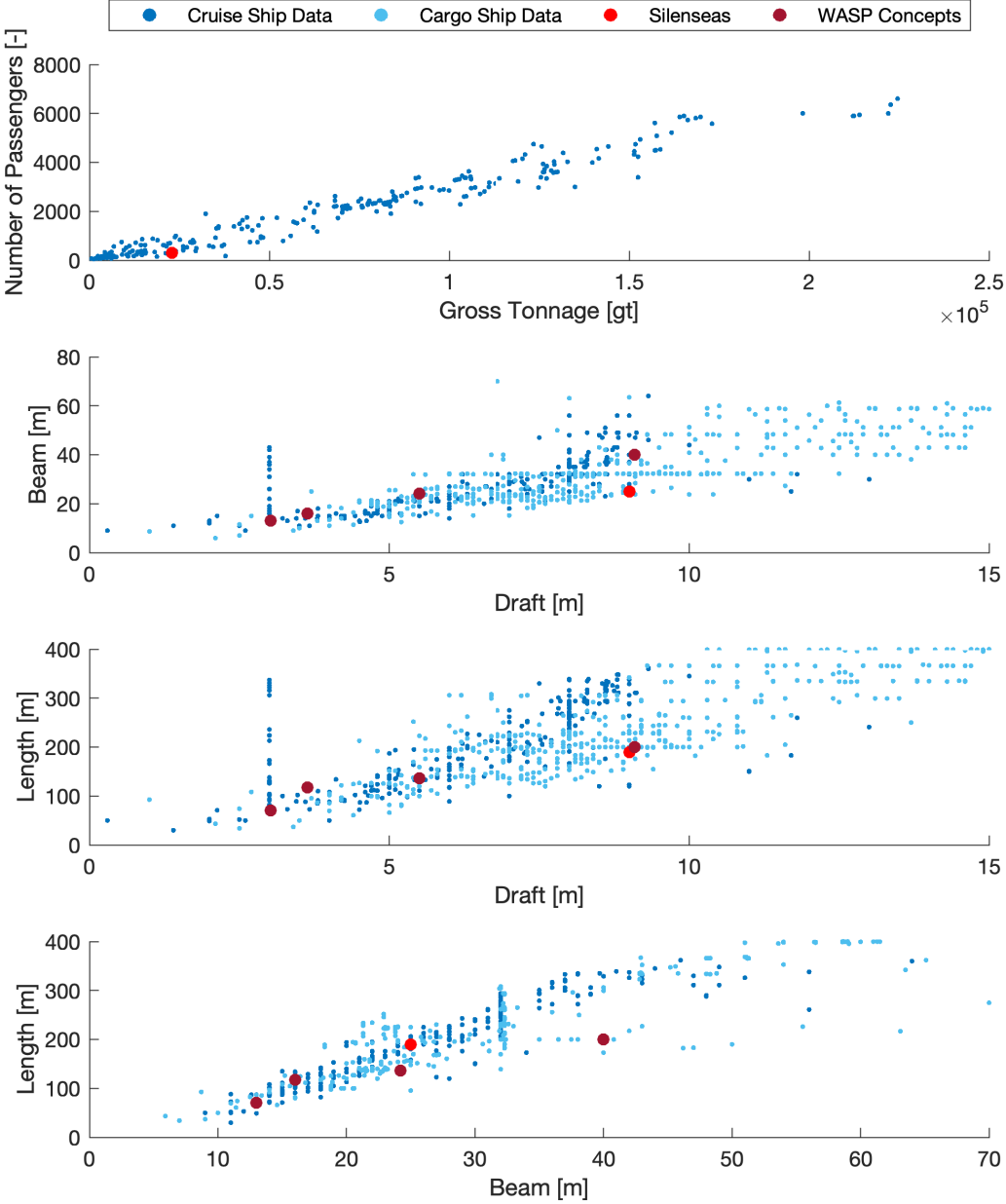
Appendix C: MARIN Ferry Design Data

Information on the reference ship geometry used as basis for the Silenseas ship design.

1.   MAIN PARTICULARS OF SHIP AND LOADING CONDITION

DESIGNATION	SYMBOL	MAGNITUDE	UNIT
Length between perpendiculars	L_{PP}	190.000	m
Length on waterline	L_{WL}	195.647	m
Length overall submerged	L_{OS}	201.656	m
Breadth moulded on WL	B	30.000	m
Depth	-	32.2	m
Average draught moulded	T_M	7.000	m
Draught moulded on F_{PP}	T_F	7.000	m
Draught moulded on A_{PP}	T_A	7.000	m
Displacement volume moulded	∇	24476	m³
Displacement mass in seawater	Δ_1	25112	t
Wetted surface area bare hull	S	6554.1	m²
LCB position aft of F_{PP}	FB	99.02	m
LCB position forward of midship	-	-2.117	% of L_{PP}
Transverse metacentric height	GMt	2.03	m
Vertical position centre of gravity	KG	14.66	m
Vertical position centre of buoyancy	KB	3.94	m
Transverse metacentre above base	KM	16.69	m
Natural period of roll	T_ϕ	17.9	s
Block coefficient	C_B	0.613	-
Midship section coefficient	C_M	0.979	-
Prismatic coefficient	C_P	0.627	-
Length-Breadth ratio	L_{PP}/B	6.333	-
Breadth-Draught ratio	B/T	4.286	-
Length-Draught ratio	L_{PP}/T	27.14	-
Frontal lateral wind area	A_F	428	m²
Transverse lateral wind area	A_L	4848	m²

2.   PARTICULARS OF PROPELLER AND RUDDER

DESIGNATION	SYMBOL	MAGNITUDE	UNIT
Number of propellers	-	2	-
Propeller type	-	FPP	-
Diameter	D	5400	mm
Pitch at 0.7R	$P_{0.7}$	4671	mm
Pitch ratio at 0.7R	$P_{0.7}/D$	0.865	-
Boss-diameter ratio	d/D	0.200	-
Expanded blade area ratio	A_E/A_0	0.599	-
Number of blades	Z	4	-
Direction of rotation	-	Inward over the top	-
Longitudinal position of propeller from A_{PP}	x_P	3.262	m
Offset of PS propeller from centreline	y_P	6.450	m
Offset of propeller from baseline	z_P	2.842	m
Available shaft power at 100%MCR	P_S	20.000 (2 x 10.000)	kW

DESIGNATION	SYMBOL	MAGNITUDE	UNIT
Number of rudders	-	2	-
Rudder type	-	Spade	-
Average height	b_R	5.600	m
Average chord	c_R	3.700	m
Geometric aspect ratio b_R/c_R	λ_R	1.51	-
Maximum rudder thickness	t	0.945	m
Thickness / chord t / c_R	-	25.5	%
Movable area	A_R	20.72	m^2
Movable rudder area ratio $A_R/(L_{PP}*T_M)$	-	1.56	%
Longitudinal position of rudder axis from A_{PP}	x_R	0.0	m
Offset of PS rudder axis from centreline	y_R	6.450	m
Clearance rudder tip with baseline	z_{tip}	0.107	m
Angle of the rudder axis with horizontal	β_R	90	deg

The ship's lateral area is calculated with a ship's draught of T_M = 7.00 m and a ship's length of L_{PP} = 190.0 m. Average height and chord of the rudders with head boxes are defined for only the movable part of the rudder.

3. BODY PLAN OF SHIP MODEL
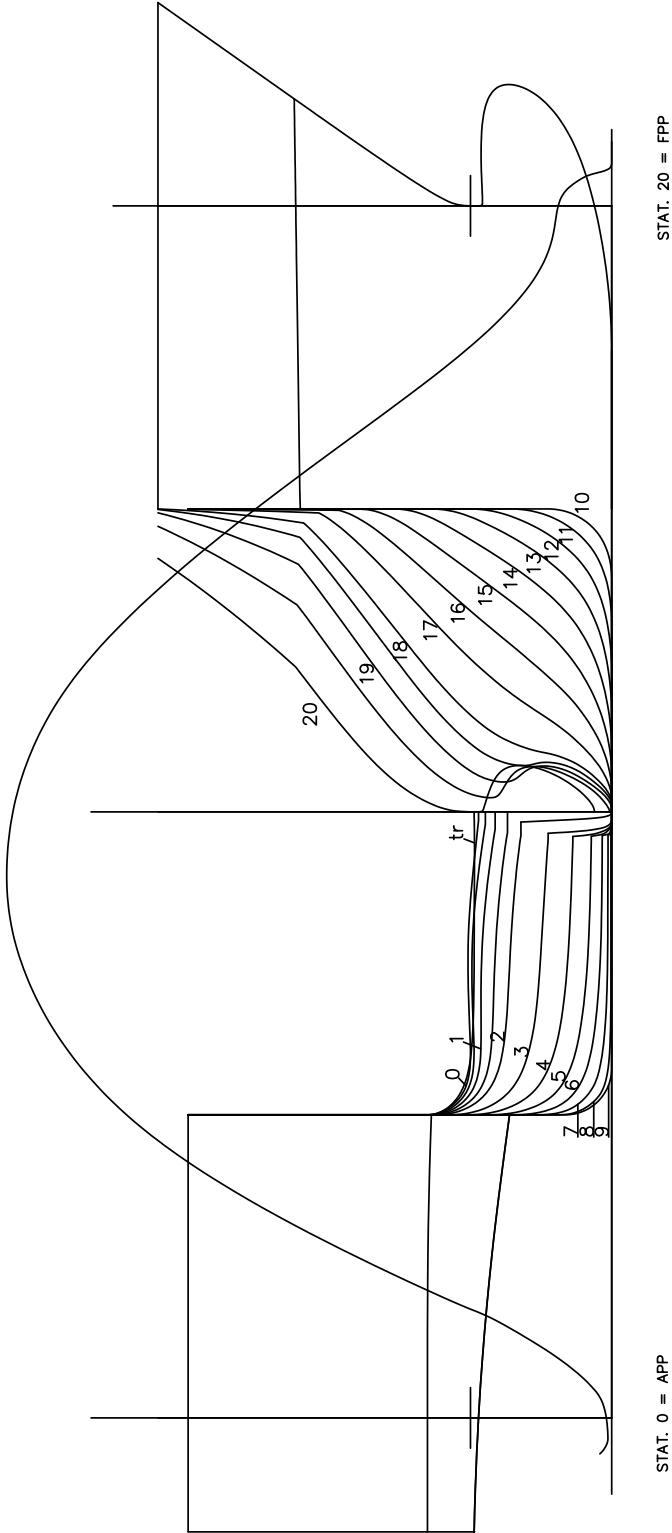
BODY PLAN, STEM AND STERN PROFILES AND SECTIONAL AREA CURVE OF
SHIP MODEL No. 9974 FOR A DRAUGHT OF 7.000 m FWD. AND 7.000 m AFT.

Appendix D: Summarized CFD Results

Results from the CFD study on ship designs under drift. Results are presented in the form of maneuvering model fit coefficients.

B/T	Deadrise	Skeg	AR	CD90	CD0	e	Te	Te/T
[-]	[deg]		[-]	[-]	[-]	[-]	[m]	[-]
2.0	0	0	0.016	1.105	0.008	0.322	4.11	0.36
2.0	5	0	0.024	0.981	0.006	0.344	5.24	0.44
2.0	10	0	0.023	1.126	0.006	0.501	6.24	0.51
2.0	15	0	0.004	1.681	0.005	0.887	3.51	0.28
2.0	0	Short	0.063	1.225	0.008	0.519	10.77	0.94
2.0	5	Short	0.077	1.121	0.007	0.472	11.29	0.95
2.0	10	Short	0.080	1.234	0.006	0.498	11.72	0.95
2.0	15	Short	0.068	1.595	0.006	0.598	11.88	0.93
2.0	0	Long	0.077	1.413	0.008	0.507	11.88	1.03
2.0	5	Long	0.100	1.185	0.007	0.467	12.94	1.09
2.0	10	Long	0.100	1.295	0.006	0.484	13.14	1.07
2.0	15	Long	0.086	1.644	0.006	0.565	13.19	1.04
2.8	0	0	0.032	0.555	0.009	0.393	6.60	0.68
2.8	5	0	0.037	0.487	0.008	0.443	7.50	0.74
2.8	10	0	0.025	0.656	0.007	0.532	6.75	0.65
2.8	15	0	0.023	0.807	0.007	0.875	8.32	0.77
2.8	0	Short	0.082	0.583	0.010	0.551	12.65	1.30
2.8	5	Short	0.083	0.592	0.008	0.551	12.70	1.26
2.8	10	Short	0.082	0.709	0.007	0.568	12.79	1.23
2.8	15	Short	0.089	0.721	0.007	0.632	14.03	1.30
2.8	0	Long	0.101	0.681	0.010	0.538	14.08	1.45
2.8	5	Long	0.103	0.700	0.008	0.535	14.13	1.41
2.8	10	Long	0.101	0.813	0.007	0.547	14.09	1.36
2.8	15	Long	0.108	0.797	0.007	0.597	15.25	1.42
3.6	0	0	0.043	0.393	0.011	0.398	7.78	0.90
3.6	5	0	0.044	0.306	0.009	0.426	8.13	0.91
3.6	10	0	0.042	0.282	0.008	0.515	8.72	0.95
3.6	15	0	0.041	0.298	0.008	0.637	9.64	1.01
3.6	0	Short	0.089	0.421	0.011	0.550	13.38	1.56
3.6	5	Short	0.089	0.388	0.010	0.560	13.49	1.52
3.6	10	Short	0.092	0.375	0.009	0.568	13.82	1.50
3.6	15	Short	0.091	0.421	0.008	0.597	14.06	1.48
3.6	0	Long	0.109	0.506	0.011	0.541	14.80	1.73
3.6	5	Long	0.111	0.474	0.010	0.538	14.90	1.68
3.6	10	Long	0.112	0.478	0.009	0.551	15.11	1.65
3.6	15	Long	0.110	0.523	0.008	0.571	15.27	1.61
4.4	0	0	0.051	0.306	0.013	0.375	8.46	1.09
4.4	5	0	0.049	0.242	0.011	0.399	8.50	1.05
4.4	10	0	0.046	0.207	0.010	0.443	8.65	1.04
4.4	15	0	0.047	0.154	0.009	0.513	9.45	1.10
4.4	0	Short	0.094	0.350	0.013	0.518	13.58	1.75
4.4	5	Short	0.095	0.302	0.011	0.530	13.84	1.72
4.4	10	Short	0.094	0.293	0.010	0.552	13.99	1.68
4.4	15	Short	0.095	0.288	0.010	0.556	14.15	1.65
4.4	0	Long	0.114	0.416	0.013	0.524	15.18	1.96
4.4	5	Long	0.113	0.406	0.011	0.531	15.27	1.90
4.4	10	Long	0.114	0.381	0.010	0.545	15.51	1.87
4.4	15	Long	0.115	0.368	0.010	0.539	15.46	1.80

Appendix E: Power Prediction Program Results

PPP Result of Optimal (Passive-appendage) Ship Design:
TWS in [m/s] and TWA in [deg]
Emissions in [g/(t*nm)]

TWA \ TWS	0.5	1.5	2.5	3.5	4.5	5.5	6.5	7.5	8.5	9.5	10.5	11.5	12.5	13.5	14.5	15.5	16.5	17.5	18.5	19.5	20.5	21.5	22.5	23.5	24.5	25.5
0	22.1	22.3	22.4	22.6	22.8	23.0	23.2	23.5	23.8	24.0	24.4	24.7	25.0	25.4	25.8	26.2	26.6	27.0	27.5	28.0	28.5	29.0	29.5	30.1	30.7	31.3
5	22.1	22.3	22.4	22.6	22.7	22.9	23.1	23.3	23.5	23.8	24.1	24.4	24.7	25.0	25.4	25.8	26.2	26.6	27.1	27.5	28.0	28.5	29.1	29.6	30.2	30.8
10	22.1	22.2	22.3	22.4	22.5	22.6	22.7	22.8	22.9	23.1	23.3	23.5	23.7	24.0	24.3	24.7	25.0	25.4	25.8	26.3	26.7	27.2	27.7	28.3	28.8	29.4
15	22.1	22.2	22.2	22.1	22.0	22.0	21.9	21.9	21.9	21.9	21.9	22.0	22.2	22.3	22.6	22.8	23.1	23.4	23.8	24.2	24.6	25.1	25.6	26.1	26.6	27.2
20	22.1	22.1	22.0	21.7	21.5	21.2	20.9	20.6	20.4	20.2	20.1	20.0	20.0	20.0	20.1	20.3	20.4	20.7	20.9	21.2	21.6	21.9	22.3	22.8	23.3	23.8
25	22.1	22.0	21.7	21.3	20.8	20.2	19.6	19.1	18.6	18.2	17.8	17.5	17.2	17.1	16.9	16.9	16.9	17.1	17.4	17.7	18.1	18.5	19.0	19.6	20.2	20.8
30	22.1	21.9	21.4	20.7	19.9	19.1	18.2	17.3	16.5	15.7	15.0	14.4	13.9	13.6	13.5	13.5	13.7	13.9	14.3	14.7	15.2	15.8	16.4	17.0	17.7	18.4
35	22.1	21.7	21.0	20.1	19.0	17.8	16.6	15.3	14.1	13.0	11.9	11.0	10.6	10.4	10.3	10.5	10.8	11.1	11.6	12.2	12.8	13.4	14.1	14.9	15.7	16.5
40	22.1	21.6	20.7	19.5	18.2	16.6	15.0	13.4	11.7	10.0	8.6	7.9	7.6	7.5	7.6	7.9	8.3	8.8	9.4	10.1	10.9	11.7	12.5	13.4	14.3	15.3
45	22.0	21.4	20.3	19.0	17.3	15.5	13.5	11.4	9.3	7.1	5.6	5.1	4.8	4.9	5.2	5.6	6.2	6.9	7.7	8.6	9.5	10.5	11.5	12.6	13.7	14.8
50	22.0	21.3	20.0	18.4	16.5	14.4	12.0	9.5	7.0	4.4	2.9	2.5	2.4	2.6	3.1	3.7	4.4	5.3	6.3	7.4	8.5	9.7	10.9	12.2	13.4	14.8
55	22.0	21.2	19.7	17.9	15.8	13.4	10.7	7.9	4.9	1.8	0.4	0.1	0.1	0.5	1.1	1.9	2.8	3.9	5.1	6.4	7.8	9.2	10.6	12.1	13.7	15.2
60	22.0	21.0	19.5	17.5	15.2	12.5	9.6	6.4	3.1	0.0	0.0	0.0	0.0	0.0	0.0	0.4	1.6	3.1	4.6	6.2	7.9	9.6	11.4	13.2	15.1	17.0
65	22.0	20.9	19.2	17.2	14.7	11.8	8.7	5.2	1.5	0.0	0.0	0.0	0.0	0.0	0.0	0.0	1.2	3.0	5.0	7.0	9.1	11.3	13.5	15.8	18.0	20.3
70	21.9	20.8	19.1	16.9	14.3	11.3	7.9	4.3	0.3	0.0	0.0	0.0	0.0	0.0	0.0	0.0	1.2	3.4	5.7	8.0	10.5	13.0	15.7	18.3	21.1	23.8
75	21.9	20.7	18.9	16.7	14.0	10.9	7.5	3.6	0.0	0.0	0.0	0.0	0.0	0.0	0.0	0.0	0.0	2.2	4.6	7.1	9.7	12.5	15.4	18.4	21.5	24.7
80	21.9	20.7	18.8	16.5	13.8	10.7	7.1	3.0	0.0	0.0	0.0	0.0	0.0	0.0	0.0	0.0	0.0	0.0	0.4	3.1	5.9	9.0	12.2	15.6	19.1	22.8
85	21.9	20.6	18.8	16.5	13.8	10.7	7.0	2.7	0.0	0.0	0.0	0.0	0.0	0.0	0.0	0.0	0.0	0.0	0.0	0.0	2.4	5.9	9.7	13.8	18.0	22.4
90	21.9	20.6	18.8	16.5	13.9	10.8	7.0	2.7	0.0	0.0	0.0	0.0	0.0	0.0	0.0	0.0	0.0	0.0	0.0	0.0	0.0	3.2	7.5	12.0	16.8	21.8
95	21.9	20.6	18.8	16.7	14.1	11.0	7.2	3.0	0.0	0.0	0.0	0.0	0.0	0.0	0.0	0.0	0.0	0.0	0.0	0.0	0.0	0.0	4.4	9.4	14.7	20.2
100	21.9	20.6	18.9	16.8	14.4	11.3	7.7	3.7	0.0	0.0	0.0	0.0	0.0	0.0	0.0	0.0	0.0	0.0	0.0	0.0	0.0	0.0	0.6	6.1	12.0	18.3
105	21.9	20.7	19.0	17.1	14.8	11.8	8.4	4.6	0.2	0.0	0.0	0.0	0.0	0.0	0.0	0.0	0.0	0.0	0.0	0.0	0.0	0.0	0.0	2.0	8.7	15.9
110	21.9	20.7	19.2	17.4	15.2	12.4	9.3	5.7	1.5	0.0	0.0	0.0	0.0	0.0	0.0	0.0	0.0	0.0	0.0	0.0	0.0	0.0	0.0	0.0	4.0	12.2
115	21.9	20.8	19.4	17.7	15.7	13.2	10.4	7.0	3.0	0.0	0.0	0.0	0.0	0.0	0.0	0.0	0.0	0.0	0.0	0.0	0.0	0.0	0.0	0.0	0.0	6.6
120	21.9	20.9	19.6	18.1	16.3	14.1	11.5	8.3	4.6	0.4	0.0	0.0	0.0	0.0	0.0	0.0	0.0	0.0	0.0	0.0	0.0	0.0	0.0	0.0	0.0	0.0
125	21.9	21.0	19.8	18.5	16.9	15.0	12.6	9.8	6.4	2.5	0.0	0.0	0.0	0.0	0.0	0.0	0.0	0.0	0.0	0.0	0.0	0.0	0.0	0.0	0.0	0.0
130	21.9	21.1	20.0	18.9	17.5	15.9	13.8	11.3	8.2	4.6	0.5	0.0	0.0	0.0	0.0	0.0	0.0	0.0	0.0	0.0	0.0	0.0	0.0	0.0	0.0	0.0
135	22.0	21.2	20.2	19.3	18.2	16.8	15.0	12.8	10.0	6.8	3.0	0.0	0.0	0.0	0.0	0.0	0.0	0.0	0.0	0.0	0.0	0.0	0.0	0.0	0.0	0.0
140	22.0	21.3	20.5	19.7	18.8	17.7	16.2	14.2	11.8	8.9	5.4	1.5	0.0	0.0	0.0	0.0	0.0	0.0	0.0	0.0	0.0	0.0	0.0	0.0	0.0	0.0
145	22.0	21.4	20.7	20.1	19.4	18.5	17.3	15.6	13.5	12.2	7.8	4.2	0.0	0.0	0.0	0.0	0.0	0.0	0.0	0.0	0.0	0.0	0.0	0.0	0.0	0.0
150	22.0	21.5	20.9	20.5	20.0	19.3	18.3	16.9	15.0	12.6	9.0	4.6	0.0	0.0	0.0	0.0	0.0	0.0	0.0	0.0	0.0	0.0	0.0	0.0	0.0	0.0
155	22.0	21.6	21.2	20.8	20.5	20.0	19.2	18.0	16.1	13.2	9.5	5.2	0.1	0.0	0.0	0.0	0.0	0.0	0.0	0.0	0.0	0.0	0.0	0.0	0.0	0.0
160	22.0	21.7	21.4	21.1	20.9	20.6	20.0	18.8	16.6	13.7	10.0	5.6	0.4	0.0	0.0	0.0	0.0	0.0	0.0	0.0	0.0	0.0	0.0	0.0	0.0	0.0
165	22.0	21.8	21.5	21.3	21.3	21.1	20.6	19.8	17.1	14.1	10.4	6.0	0.7	0.0	0.0	0.0	0.0	0.0	0.0	0.0	0.0	0.0	0.0	0.0	0.0	0.0
170	22.0	21.9	21.7	21.6	21.5	21.4	20.9	19.6	17.4	14.5	10.9	6.4	1.2	0.0	0.0	0.0	0.0	0.0	0.0	0.0	4.0	4.8	5.2	5.4	5.5	5.6
175	22.0	21.9	21.8	21.7	21.7	21.7	21.1	19.8	17.7	14.9	11.3	6.9	1.7	0.0	0.0	0.0	0.0	0.0	0.0	0.0	0.0	14.1	14.6	14.9	14.8	14.7
180	22.0	21.9	21.9	21.8	21.8	21.7	21.2	19.9	17.9	15.1	11.6	7.3	2.2	0.0	0.0	0.0	0.0	0.0	0.0	0.0	0.0	19.5	19.3	18.9	18.6	18.3
185	22.0	21.9	21.8	21.7	21.7	21.7	21.1	19.8	17.7	14.9	11.3	6.9	1.7	0.0	0.0	0.0	0.0	0.0	0.0	0.0	0.0	14.1	14.7	14.9	14.9	14.8
190	22.0	21.9	21.7	21.6	21.5	21.4	20.9	19.6	17.4	14.5	10.9	6.4	1.2	0.0	0.0	0.0	0.0	0.0	0.0	0.0	4.0	4.8	5.2	5.4	5.5	5.6
195	22.0	21.8	21.5	21.3	21.3	21.1	20.6	19.8	17.1	14.1	10.4	6.0	0.7	0.0	0.0	0.0	0.0	0.0	0.0	0.0	0.0	0.0	0.0	0.0	0.0	0.0
200	22.0	21.7	21.4	21.1	20.9	20.6	20.0	19.0	16.6	13.7	10.0	5.6	0.4	0.0	0.0	0.0	0.0	0.0	0.0	0.0	0.0	0.0	0.0	0.0	0.0	0.0
205	22.0	21.6	21.2	20.8	20.5	20.0	19.2	18.0	16.1	13.2	9.5	5.2	0.1	1.9	0.0	0.0	0.0	0.0	0.0	0.0	0.0	0.0	0.0	0.0	0.0	0.0
210	22.0	21.5	20.9	20.5	20.0	19.3	18.3	16.9	15.0	12.6	9.0	4.6	0.0	0.0	0.0	0.0	0.0	0.0	0.0	0.0	0.0	0.0	0.0	0.0	0.0	0.0
215	22.0	21.4	20.7	20.1	19.4	18.5	17.3	15.6	13.5	12.2	7.8	4.2	0.0	0.0	0.0	0.0	0.0	0.0	0.0	0.0	0.0	0.0	0.0	0.0	0.0	0.0
220	22.0	21.3	20.5	19.7	18.8	17.7	16.2	14.2	11.8	8.9	5.4	1.5	0.0	0.0	0.0	0.0	0.0	0.0	0.0	0.0	0.0	0.0	0.0	0.0	0.0	0.0
225	22.0	21.2	20.2	19.3	18.2	16.8	15.0	12.8	10.0	6.8	3.0	0.0	0.0	0.0	0.0	0.0	0.0	0.0	0.0	0.0	0.0	0.0	0.0	0.0	0.0	0.0
230	21.9	21.1	20.0	18.9	17.5	15.9	13.8	11.3	8.2	4.6	0.5	0.0	0.0	0.0	0.0	0.0	0.0	0.0	0.0	0.0	0.0	0.0	0.0	0.0	0.0	0.0
235	21.9	21.0	19.8	18.5	16.9	15.0	12.6	9.8	6.4	2.5	0.0	0.0	0.0	0.0	0.0	0.0	0.0	0.0	0.0	0.0	0.0	0.0	0.0	0.0	0.0	0.0
240	21.9	20.9	19.6	18.1	16.3	14.1	11.5	8.3	4.6	0.4	0.0	0.0	0.0	0.0	0.0	0.0	0.0	0.0	0.0	0.0	0.0	0.0	0.0	0.0	0.0	0.0
245	21.9	20.8	19.4	17.7	15.7	13.2	10.4	7.0	3.0	0.0	0.0	0.0	0.0	0.0	0.0	0.0	0.0	0.0	0.0	0.0	0.0	0.0	0.0	0.0	0.0	6.6
250	21.9	20.7	19.2	17.4	15.2	12.4	9.3	5.7	1.5	0.0	0.0	0.0	0.0	0.0	0.0	0.0	0.0	0.0	0.0	0.0	0.0	0.0	0.0	0.0	4.0	12.2
255	21.9	20.7	19.0	17.1	14.8	11.8	8.4	4.6	0.2	0.0	0.0	0.0	0.0	0.0	0.0	0.0	0.0	0.0	0.0	0.0	0.0	0.0	0.0	2.0	8.7	15.9
260	21.9	20.6	18.9	16.8	14.4	11.3	7.7	3.7	0.0	0.0	0.0	0.0	0.0	0.0	0.0	0.0	0.0	0.0	0.0	0.0	0.0	0.0	0.6	6.1	12.0	18.3
265	21.9	20.6	18.8	16.7	14.1	11.0	7.2	3.0	0.0	0.0	0.0	0.0	0.0	0.0	0.0	0.0	0.0	0.0	0.0	0.0	0.0	0.0	4.4	9.4	14.7	20.2
270	21.9	20.6	18.8	16.5	13.9	10.8	7.0	2.7	0.0	0.0	0.0	0.0	0.0	0.0	0.0	0.0	0.0	0.0	0.0	0.0	0.0	3.2	7.5	12.0	16.8	21.8
275	21.9	20.6	18.8	16.5	13.8	10.7	7.0	2.7	0.0	0.0	0.0	0.0	0.0	0.0	0.0	0.0	0.0	0.0	0.0	0.0	2.4	5.9	9.7	13.8	18.0	22.4
280	21.9	20.7	18.8	16.5	13.8	10.7	7.1	3.0	0.0	0.0	0.0	0.0	0.0	0.0	0.0	0.0	0.0	0.0	0.4	3.1	5.9	9.0	12.2	15.6	19.1	22.8
285	21.9	20.7	18.9	16.7	14.0	10.9	7.5	3.6	0.0	0.0	0.0	0.0	0.0	0.0	0.0	0.0	0.0	2.2	4.6	7.1	9.7	12.5	15.4	18.4	21.5	24.7
290	21.9	20.8	19.1	16.9	14.3	11.3	7.9	4.3	0.3	0.0	0.0	0.0	0.0	0.0	0.0	0.0	1.2	3.4	5.7	8.0	10.5	13.0	15.7	18.3	21.1	23.8
295	22.0	20.9	19.2	17.2	14.7	11.8	8.7	5.2	1.5	0.0	0.0	0.0	0.0	0.0	0.0	0.0	1.2	3.0	5.0	7.0	9.1	11.3	13.5	15.8	18.0	20.3
300	22.0	21.0	19.5	17.5	15.2	12.5	9.6	6.4	3.1	0.0	0.0	0.0	0.0	0.0	0.0	0.4	1.6	3.1	4.6	6.2	7.9	9.6	11.4	13.2	15.1	17.0
305	22.0	21.1	19.7	17.9	15.8	13.4	10.7	7.9	4.9	1.8	0.4	0.1	0.1	0.5	1.1	1.9	2.8	3.9	5.1	6.4	7.8	9.2	10.6	12.1	13.7	15.2

PPP Result of Optimal (Passive-appendage) Ship Design:
TWS in [m/s] and TWA in [deg]
Emissions in [g/(t*nm)]

TWA \ TWS	0.5	1.5	2.5	3.5	4.5	5.5	6.5	7.5	8.5	9.5	10.5	11.5	12.5	13.5	14.5	15.5	16.5	17.5	18.5	19.5	20.5	21.5	22.5	23.5	24.5	25.5
310	22.0	21.3	20.0	18.4	16.5	14.4	12.0	9.5	7.0	4.4	2.9	2.5	2.4	2.6	3.1	3.7	4.4	5.3	6.3	7.4	8.5	9.7	10.9	12.2	13.4	14.8
315	22.0	21.4	20.3	19.0	17.3	15.5	13.5	11.4	9.3	7.1	5.6	5.1	4.8	4.9	5.2	5.6	6.2	6.9	7.7	8.6	9.5	10.5	11.5	12.6	13.7	14.8
320	22.1	21.6	20.7	19.5	18.2	16.6	15.0	13.4	11.7	10.0	8.6	7.9	7.6	7.5	7.6	7.9	8.3	8.8	9.4	10.1	10.9	11.7	12.5	13.4	14.3	15.3
325	22.1	21.7	21.0	20.1	19.0	17.8	16.6	15.3	14.1	13.0	11.9	11.0	10.6	10.4	10.3	10.5	10.8	11.1	11.6	12.2	12.8	13.4	14.1	14.9	15.7	16.5
330	22.1	21.9	21.4	20.7	19.9	19.1	18.2	17.3	16.5	15.7	15.0	14.4	13.9	13.6	13.5	13.5	13.7	13.9	14.3	14.7	15.2	15.8	16.4	17.0	17.7	18.4
335	22.1	22.0	21.7	21.3	20.8	20.2	19.6	19.1	18.6	18.2	17.8	17.5	17.2	17.1	16.9	16.9	16.9	17.1	17.4	17.7	18.1	18.5	19.0	19.6	20.2	20.8
340	22.1	22.1	22.0	21.7	21.5	21.2	20.9	20.6	20.4	20.2	20.1	20.0	20.0	20.0	20.1	20.3	20.4	20.7	20.9	21.2	21.6	21.9	22.3	22.8	23.3	23.8
345	22.1	22.2	22.2	22.1	22.0	22.0	21.9	21.9	21.9	21.9	21.9	22.0	22.2	22.3	22.6	22.8	23.1	23.4	23.8	24.2	24.6	25.1	25.6	26.1	26.6	27.2
350	22.1	22.2	22.3	22.4	22.5	22.6	22.7	22.8	22.9	23.1	23.3	23.5	23.7	24.0	24.3	24.7	25.0	25.4	25.8	26.3	26.7	27.2	27.7	28.3	28.8	29.4
355	22.1	22.3	22.4	22.6	22.7	22.9	23.1	23.3	23.5	23.8	24.1	24.4	24.7	25.0	25.4	25.8	26.2	26.6	27.1	27.5	28.0	28.5	29.1	29.6	30.2	30.8

PPP Result of Optimal (Active-appendage) Ship Design:
TWS in [m/s] and TWA in [deg]
Emissions in [g/(t*nm)]

TWA \ TWS	0.5	1.5	2.5	3.5	4.5	5.5	6.5	7.5	8.5	9.5	10.5	11.5	12.5	13.5	14.5	15.5	16.5	17.5	18.5	19.5	20.5	21.5	22.5	23.5	24.5	25.5
0	22.1	22.3	22.4	22.6	22.8	23.0	23.2	23.5	23.8	24.1	24.4	24.7	25.0	25.4	25.8	26.2	26.6	27.0	27.5	28.0	28.5	29.0	29.5	30.1	30.7	31.3
5	22.1	22.3	22.4	22.5	22.7	22.9	23.1	23.3	23.5	23.8	24.0	24.3	24.6	25.0	25.3	25.7	26.1	26.5	27.0	27.4	27.9	28.4	28.9	29.5	30.1	30.6
10	22.1	22.2	22.3	22.4	22.4	22.5	22.6	22.7	22.8	22.9	23.1	23.3	23.5	23.7	24.0	24.3	24.6	25.0	25.4	25.8	26.2	26.7	27.2	27.7	28.2	28.8
15	22.1	22.2	22.1	22.1	22.0	21.9	21.7	21.6	21.6	21.5	21.5	21.5	21.5	21.6	21.8	21.9	22.1	22.4	22.7	23.0	23.4	23.8	24.2	24.7	25.2	25.7
20	22.1	22.1	21.9	21.7	21.3	21.0	20.6	20.2	19.9	19.6	19.3	19.0	18.9	18.7	18.7	18.7	18.7	18.8	18.9	19.1	19.3	19.6	19.8	20.2	20.5	20.9
25	22.1	22.0	21.6	21.2	20.6	19.9	19.2	18.5	17.8	17.1	16.5	15.9	15.5	15.1	14.7	14.4	14.2	14.0	13.9	13.8	13.8	13.8	13.9	14.1	14.2	
30	22.1	21.8	21.3	20.6	19.7	18.7	17.6	16.5	15.4	14.3	13.3	12.3	11.4	10.6	9.8	9.1	8.5	8.0	7.5	7.1	6.7	6.4	6.2	6.0	5.9	6.0
35	22.1	21.7	21.0	20.0	18.8	17.4	16.0	14.4	12.9	11.3	9.7	8.3	6.8	5.5	4.2	3.0	1.9	0.8	0.0	0.0	0.0	0.0	0.0	0.0	0.0	0.0
40	22.1	21.6	20.6	19.4	17.9	16.2	14.4	12.4	10.3	8.2	6.2	4.1	2.1	0.1	0.0	0.0	0.0	0.0	0.0	0.0	0.0	0.0	0.0	0.0	0.0	0.0
45	22.0	21.4	20.2	18.8	17.0	15.0	12.8	10.4	7.9	5.3	2.7	0.0	0.0	0.0	0.0	0.0	0.0	0.0	0.0	0.0	0.0	0.0	0.0	0.0	0.0	0.0
50	22.0	21.3	19.9	18.2	16.3	14.0	11.4	8.6	5.6	2.5	0.0	0.0	0.0	0.0	0.0	0.0	0.0	0.0	0.0	0.0	0.0	0.0	0.0	0.0	0.0	0.0
55	22.0	21.1	19.6	17.8	15.6	13.0	10.1	7.0	3.6	0.1	0.0	0.0	0.0	0.0	0.0	0.0	0.0	0.0	0.0	0.0	0.0	0.0	0.0	0.0	0.0	0.0
60	22.0	21.0	19.4	17.4	14.9	12.2	9.0	5.6	1.9	0.0	0.0	0.0	0.0	0.0	0.0	0.0	0.0	0.0	0.0	0.0	0.0	0.0	0.0	0.0	0.0	0.0
65	22.0	20.9	19.1	17.0	14.4	11.5	8.2	4.5	0.5	0.0	0.0	0.0	0.0	0.0	0.0	0.0	0.0	0.0	0.0	0.0	0.0	0.0	0.0	0.0	0.0	0.0
70	21.9	20.8	19.0	16.7	14.1	11.0	7.5	3.6	0.0	0.0	0.0	0.0	0.0	0.0	0.0	0.0	0.0	0.0	0.0	0.0	0.0	0.0	0.0	0.0	0.0	0.0
75	21.9	20.7	18.8	16.6	13.8	10.7	7.1	3.0	0.0	0.0	0.0	0.0	0.0	0.0	0.0	0.0	0.0	0.0	0.0	0.0	0.0	0.0	0.0	0.0	0.0	0.0
80	21.9	20.6	18.8	16.4	13.7	10.5	6.8	2.5	0.0	0.0	0.0	0.0	0.0	0.0	0.0	0.0	0.0	0.0	0.0	0.0	0.0	0.0	0.0	0.0	0.0	0.0
85	21.9	20.6	18.7	16.4	13.7	10.5	6.7	2.3	0.0	0.0	0.0	0.0	0.0	0.0	0.0	0.0	0.0	0.0	0.0	0.0	0.0	0.0	0.0	0.0	0.0	0.0
90	21.9	20.6	18.7	16.5	13.8	10.6	6.7	2.3	0.0	0.0	0.0	0.0	0.0	0.0	0.0	0.0	0.0	0.0	0.0	0.0	0.0	0.0	0.0	0.0	0.0	0.0
95	21.9	20.6	18.8	16.6	14.0	10.8	7.0	2.8	0.0	0.0	0.0	0.0	0.0	0.0	0.0	0.0	0.0	0.0	0.0	0.0	0.0	0.0	0.0	0.0	0.0	0.0
100	21.9	20.6	18.9	16.8	14.3	11.2	7.6	3.5	0.0	0.0	0.0	0.0	0.0	0.0	0.0	0.0	0.0	0.0	0.0	0.0	0.0	0.0	0.0	0.0	0.0	0.0
105	21.9	20.6	19.0	17.0	14.7	11.7	8.3	4.5	0.1	0.0	0.0	0.0	0.0	0.0	0.0	0.0	0.0	0.0	0.0	0.0	0.0	0.0	0.0	0.0	0.0	0.0
110	21.9	20.7	19.1	17.3	15.2	12.4	9.3	5.6	1.4	0.0	0.0	0.0	0.0	0.0	0.0	0.0	0.0	0.0	0.0	0.0	0.0	0.0	0.0	0.0	0.0	0.0
115	21.9	20.8	19.3	17.7	15.7	13.2	10.3	6.9	2.9	0.0	0.0	0.0	0.0	0.0	0.0	0.0	0.0	0.0	0.0	0.0	0.0	0.0	0.0	0.0	0.0	0.0
120	21.9	20.8	19.5	18.1	16.3	14.0	11.5	8.3	4.6	0.3	0.0	0.0	0.0	0.0	0.0	0.0	0.0	0.0	0.0	0.0	0.0	0.0	0.0	0.0	0.0	0.0
125	21.9	20.9	19.8	18.5	16.9	14.9	12.6	9.7	6.4	2.4	0.0	0.0	0.0	0.0	0.0	0.0	0.0	0.0	0.0	0.0	0.0	0.0	0.0	0.0	0.0	0.0
130	21.9	21.0	20.0	18.9	17.5	15.9	13.8	11.3	8.2	4.6	0.5	0.0	0.0	0.0	0.0	0.0	0.0	0.0	0.0	0.0	0.0	0.0	0.0	0.0	0.0	0.0
135	22.0	21.2	20.2	19.3	18.2	16.8	15.0	12.8	10.0	6.8	3.0	0.0	0.0	0.0	0.0	0.0	0.0	0.0	0.0	0.0	0.0	0.0	0.0	0.0	0.0	0.0
140	22.0	21.3	20.5	19.7	18.8	17.7	16.2	14.2	11.8	8.9	5.4	1.5	0.0	0.0	0.0	0.0	0.0	0.0	0.0	0.0	0.0	0.0	0.0	0.0	0.0	0.0
145	22.0	21.4	20.7	20.1	19.4	18.5	17.3	15.6	13.5	12.1	7.7	4.1	0.0	0.0	0.0	0.0	0.0	0.0	0.0	0.0	0.0	0.0	0.0	0.0	0.0	0.0
150	22.0	21.5	20.9	20.5	20.0	19.3	18.3	16.9	15.0	12.6	8.9	4.6	0.0	0.0	0.0	0.0	0.0	0.0	0.0	0.0	0.0	0.0	0.0	0.0	0.0	0.0
155	22.0	21.6	21.2	20.8	20.5	20.0	19.2	18.0	16.1	13.2	9.5	5.1	0.0	0.0	0.0	0.0	0.0	0.0	0.0	0.0	0.0	0.0	0.0	0.0	0.0	0.0
160	22.0	21.7	21.3	21.1	20.9	20.6	20.0	18.8	16.6	13.7	10.0	5.5	0.3	0.0	0.0	0.0	0.0	0.0	0.0	0.0	0.0	0.0	0.0	0.0	0.0	0.0
165	22.0	21.8	21.5	21.3	21.3	21.1	20.6	19.2	17.1	14.1	10.4	6.0	0.7	0.0	0.0	0.0	0.0	0.0	0.0	0.0	0.0	0.0	0.0	0.0	0.0	0.0
170	22.0	21.9	21.7	21.6	21.5	21.4	20.9	19.6	17.4	14.5	10.9	6.4	1.2	0.0	0.0	0.0	0.0	0.0	0.0	0.0	0.0	0.0	0.0	0.0	0.0	0.0
175	22.0	21.9	21.8	21.7	21.7	21.7	21.1	19.8	17.7	14.9	11.3	6.9	1.7	0.0	0.0	0.0	0.0	0.0	0.0	0.0	0.0	0.0	0.0	0.0	0.0	0.0
180	22.0	21.9	21.9	21.8	21.8	21.7	21.2	19.9	17.9	15.1	11.6	7.3	2.2	0.0	0.0	0.0	0.0	0.0	0.0	0.0	0.0	0.0	0.0	0.0	0.0	0.0
185	22.0	21.9	21.8	21.7	21.7	21.1	19.6	17.4	14.9	11.3	6.9	1.7	0.0	0.0	0.0	0.0	0.0	0.0	0.0	0.0	0.0	0.0	0.0	0.0	0.0	0.0
190	22.0	21.9	21.7	21.6	21.5	21.4	20.9	19.6	17.4	14.5	10.9	6.4	1.2	0.0	0.0	0.0	0.0	0.0	0.0	0.0	0.0	0.0	0.0	0.0	0.0	0.0
195	22.0	21.8	21.5	21.3	21.3	21.1	20.6	19.2	17.1	14.1	10.4	6.0	0.7	0.0	0.0	0.0	0.0	0.0	0.0	0.0	0.0	0.0	0.0	0.0	0.0	0.0
200	22.0	21.7	21.3	21.1	20.9	20.6	20.0	18.8	16.6	13.7	10.0	5.5	0.3	0.0	0.0	0.0	0.0	0.0	0.0	0.0	0.0	0.0	0.0	0.0	0.0	0.0
205	22.0	21.6	21.2	20.8	20.5	20.0	19.2	18.0	16.1	13.2	9.5	5.1	0.0	0.0	0.0	0.0	0.0	0.0	0.0	0.0	0.0	0.0	0.0	0.0	0.0	0.0
210	22.0	21.5	20.9	20.5	20.0	19.3	18.3	16.9	15.0	12.6	8.9	4.6	0.0	0.0	0.0	0.0	0.0	0.0	0.0	0.0	0.0	0.0	0.0	0.0	0.0	0.0
215	22.0	21.4	20.7	20.1	19.4	18.5	17.3	15.6	13.5	10.9	7.7	4.1	0.0	0.0	0.0	0.0	0.0	0.0	0.0	0.0	0.0	0.0	0.0	0.0	0.0	0.0
220	22.0	21.3	20.5	19.7	18.8	17.7	16.2	14.2	11.8	8.9	5.4	1.5	0.0	0.0	0.0	0.0	0.0	0.0	0.0	0.0	0.0	0.0	0.0	0.0	0.0	0.0

PPP Result of Optimal (Active-appendage) Ship Design:
TWS in [m/s] and TWA in [deg]
Emissions in [g/(t*nm)]

TWS TWA	0.5	1.5	2.5	3.5	4.5	5.5	6.5	7.5	8.5	9.5	10.5	11.5	12.5	13.5	14.5	15.5	16.5	17.5	18.5	19.5	20.5	21.5	22.5	23.5	24.5	25.5
225	22.0	21.2	20.2	19.3	18.2	16.8	15.0	12.8	10.0	6.8	3.0	0.0	0.0	0.0	0.0	0.0	0.0	0.0	0.0	0.0	0.0	0.0	0.0	0.0	0.0	0.0
230	21.9	21.0	20.0	18.9	17.5	15.9	13.8	11.3	8.2	4.6	0.5	0.0	0.0	0.0	0.0	0.0	0.0	0.0	0.0	0.0	0.0	0.0	0.0	0.0	0.0	0.0
235	21.9	20.9	19.8	18.5	16.9	14.9	12.6	9.7	6.4	2.4	0.0	0.0	0.0	0.0	0.0	0.0	0.0	0.0	0.0	0.0	0.0	0.0	0.0	0.0	0.0	0.0
240	21.9	20.8	19.5	18.1	16.3	14.0	11.5	8.3	4.6	0.3	0.0	0.0	0.0	0.0	0.0	0.0	0.0	0.0	0.0	0.0	0.0	0.0	0.0	0.0	0.0	0.0
245	21.9	20.8	19.3	17.7	15.7	13.2	10.3	6.9	2.9	0.0	0.0	0.0	0.0	0.0	0.0	0.0	0.0	0.0	0.0	0.0	0.0	0.0	0.0	0.0	0.0	0.0
250	21.9	20.7	19.1	17.3	15.2	12.4	9.3	5.6	1.4	0.0	0.0	0.0	0.0	0.0	0.0	0.0	0.0	0.0	0.0	0.0	0.0	0.0	0.0	0.0	0.0	0.0
255	21.9	20.6	19.0	17.0	14.7	11.7	8.3	4.5	0.1	0.0	0.0	0.0	0.0	0.0	0.0	0.0	0.0	0.0	0.0	0.0	0.0	0.0	0.0	0.0	0.0	0.0
260	21.9	20.6	18.9	16.8	14.3	11.2	7.6	3.5	0.0	0.0	0.0	0.0	0.0	0.0	0.0	0.0	0.0	0.0	0.0	0.0	0.0	0.0	0.0	0.0	0.0	0.0
265	21.9	20.6	18.8	16.6	14.0	10.8	7.0	2.8	0.0	0.0	0.0	0.0	0.0	0.0	0.0	0.0	0.0	0.0	0.0	0.0	0.0	0.0	0.0	0.0	0.0	0.0
270	21.9	20.6	18.7	16.5	13.8	10.6	6.7	2.3	0.0	0.0	0.0	0.0	0.0	0.0	0.0	0.0	0.0	0.0	0.0	0.0	0.0	0.0	0.0	0.0	0.0	0.0
275	21.9	20.6	18.7	16.4	13.7	10.5	6.7	2.3	0.0	0.0	0.0	0.0	0.0	0.0	0.0	0.0	0.0	0.0	0.0	0.0	0.0	0.0	0.0	0.0	0.0	0.0
280	21.9	20.6	18.8	16.4	13.7	10.5	6.8	2.5	0.0	0.0	0.0	0.0	0.0	0.0	0.0	0.0	0.0	0.0	0.0	0.0	0.0	0.0	0.0	0.0	0.0	0.0
285	21.9	20.7	18.8	16.6	13.8	10.7	7.1	3.0	0.0	0.0	0.0	0.0	0.0	0.0	0.0	0.0	0.0	0.0	0.0	0.0	0.0	0.0	0.0	0.0	0.0	0.0
290	21.9	20.7	19.0	16.7	14.1	11.0	7.5	3.6	0.0	0.0	0.0	0.0	0.0	0.0	0.0	0.0	0.0	0.0	0.0	0.0	0.0	0.0	0.0	0.0	0.0	0.0
295	22.0	20.9	19.1	17.0	14.4	11.5	8.2	4.5	0.5	0.0	0.0	0.0	0.0	0.0	0.0	0.0	0.0	0.0	0.0	0.0	0.0	0.0	0.0	0.0	0.0	0.0
300	22.0	21.0	19.4	17.4	14.9	12.2	9.0	5.6	1.9	0.0	0.0	0.0	0.0	0.0	0.0	0.0	0.0	0.0	0.0	0.0	0.0	0.0	0.0	0.0	0.0	0.0
305	22.0	21.1	19.6	17.8	15.6	13.0	10.1	7.0	3.6	0.1	0.0	0.0	0.0	0.0	0.0	0.0	0.0	0.0	0.0	0.0	0.0	0.0	0.0	0.0	0.0	0.0
310	22.0	21.3	19.9	18.2	16.3	14.0	11.4	8.6	5.6	2.5	0.0	0.0	0.0	0.0	0.0	0.0	0.0	0.0	0.0	0.0	0.0	0.0	0.0	0.0	0.0	0.0
315	22.0	21.4	20.2	18.8	17.0	15.0	12.8	10.4	7.9	5.3	2.7	0.0	0.0	0.0	0.0	0.0	0.0	0.0	0.0	0.0	0.0	0.0	0.0	0.0	0.0	0.0
320	22.1	21.6	20.6	19.4	17.9	16.2	14.4	12.4	10.3	8.2	6.2	4.1	2.1	0.1	0.0	0.0	0.0	0.0	0.0	0.0	0.0	0.0	0.0	0.0	0.0	0.0
325	22.1	21.7	21.0	20.0	18.8	17.4	16.0	14.4	12.9	11.3	9.7	8.3	6.8	5.5	4.2	3.0	1.9	0.8	0.0	0.0	0.0	0.0	0.0	0.0	0.0	0.0
330	22.1	21.8	21.3	20.6	19.7	18.7	17.6	16.5	15.4	14.3	13.3	12.3	11.4	10.6	9.8	9.1	8.5	8.0	7.5	7.1	6.7	6.4	6.2	6.0	5.9	6.0
335	22.1	22.0	21.6	21.2	20.6	19.9	19.2	18.5	17.8	17.1	16.5	15.9	15.5	15.1	14.7	14.4	14.2	14.0	13.9	13.8	13.8	13.8	13.9	14.1	14.2	
340	22.1	22.1	21.9	21.7	21.3	21.0	20.6	20.2	19.9	19.6	19.3	19.0	18.9	18.7	18.7	18.7	18.8	18.9	19.1	19.3	19.6	19.8	20.2	20.5	20.9	
345	22.1	22.2	22.1	22.1	22.0	21.9	21.7	21.6	21.6	21.5	21.5	21.5	21.5	21.6	21.8	21.9	22.1	22.4	22.7	23.0	23.4	23.8	24.2	24.7	25.2	25.7
350	22.1	22.2	22.3	22.4	22.4	22.5	22.6	22.7	22.8	22.9	23.1	23.3	23.5	23.7	24.0	24.3	24.6	25.0	25.4	25.8	26.2	26.7	27.2	27.7	28.2	28.8
355	22.1	22.3	22.4	22.5	22.7	22.9	23.1	23.3	23.5	23.8	24.0	24.3	24.6	25.0	25.3	25.7	26.1	26.5	27.0	27.4	27.9	28.4	28.9	29.5	30.1	30.6